

Collisionless Ion Collection by a Sphere in a Weakly Magnetized Plasma

by

Leonardo Patacchini

Ingénieur diplômé de l'Ecole Polytechnique (X2002)

Submitted to the Department of Nuclear Science and Engineering
in partial fulfillment of the requirements for the degree of

Master of Science in Nuclear Science and Engineering


at the


MASSACHUSETTS INSTITUTE OF TECHNOLOGY


May 2007


[June 2007]

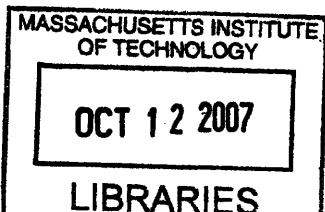
© Massachusetts Institute of Technology 2007. All rights reserved.

Author 
Department of Nuclear Science and Engineering
May 17, 2007

Certified by 
Ian H. Hutchinson
Professor
Thesis Supervisor

Certified by 
Brian Labombard
Principal Research Scientist
Thesis Reader

Accepted by 
Jeffrey A. Coderre
Chairman, Graduate Committee



ARCHIVES

Collisionless Ion Collection by a Sphere in a Weakly Magnetized Plasma

by

Leonardo Patacchini

Submitted to the Department of Nuclear Science and Engineering
on May 17, 2007, in partial fulfillment of the
requirements for the degree of
Master of Science in Nuclear Science and Engineering

Abstract

The interaction between a probe and a plasma has been studied since the 1920s and the pioneering work of Mott-Smith and Langmuir [1], and is still today an active topic of experimental and theoretical research. Indeed an understanding of the current collection process by an electrode is relevant to diverse matters such as Langmuir and Mach-probes calibrations, dusty plasma physics, or spacecraft charging.

Recent simulations relying on the *ad hoc* designed code SCEPTIC have fully addressed the collisionless and unmagnetized problem for a drifting collector idealized as a sphere. SCEPTIC is a 2d/3v hybrid Particle In Cell (PIC) code, in which the ion motion is fully resolved, while the electrons are treated as a Boltzmann distributed fluid [2, 3]. In the present work we tackle the transition between the unmagnetized and the weakly magnetized regime of ion collection by a spherical probe (The mean ion Larmor radius $r_L \geq r_p$) in a collisionless plasma (The ion mean free path $\lambda_{mfp} \gg r_p$).

When the sphere is at space potential, we demonstrate that the ion current dependence on the background magnetic field \mathbf{B} is linear for low \mathbf{B} , and provide analytical expressions for this dependence.

When the probe potential can not be neglected, the problem shows two distinct scale lengths: A collisionless layer of a few r_p close to the probe, followed by a collisional presheath of a few λ_{mfp} . The chosen approach is to resolve the collisionless scale-length with SCEPTIC, while using appropriate outer boundary conditions on the potential and ion distribution function to connect with the unresolved collisional presheath. We present results of our numerical simulations for a wide range of plasma parameters of direct relevance to Langmuir and Mach-probes.

Thesis Supervisor: Ian H. Hutchinson
Title: Professor

Thesis Reader: Brian Labombard
Title: Principal Research Scientist

Acknowledgments

The first lines of this thesis should be words of gratitude to those who contributed to this work.

First of all I would like to thank my advisor Pr. Hutchinson. In addition to his physical insight and contagious interest for Mach-probes, I shall not forget his uninterrupted support and time-commitment. I acknowledge that his tens of papers and thesis drafts proofreadings could have been fatal to many English Professors.

I express my sincere gratitude to the MIT Nuclear Science and Engineering Department as well as to the US Department of Energy, whose funding made this thesis possible.

I would also like to thank Pr. Giovanni Lapenta, who hosted me in his research group at Los Alamos National Laboratory during the summer 2006. This period resulted in a fruitful collaboration, and helped me mature my knowledge on topics of direct relevance to this thesis.

I am deeply indebted to my parents for their love and support throughout my entire life, and for their encouragement to undertake my Doctoral research in the United States.

I dedicate this thesis to Jean Marie Bénad. His devotion to the teaching of physics despite the misfortunes of life have always aroused the deepest respect and admiration in me. Où que vous soyez, j'espère que vous conscientisez tout ce que vous avez apporté à vos élèves.

Contents

I	Analytical basis	19
I.1	Position of the problem	19
I.2	Basic plasma properties	21
I.2.1	Infinite uniform plasmas	21
I.2.2	Analytical current calculations	23
I.3	Free flight ion current to a spherical probe	25
I.3.1	Unmagnetized plasma	25
I.3.2	Magnetized plasma with $\mathbf{v}_d \parallel \mathbf{B}$	26
I.4	Basic charging mechanisms with non negligible electric fields	31
I.4.1	Electron density	31
I.4.2	Orbital Motion Limited ion current in an unmagnetized plasma	32
I.4.3	Canonical upper-bound in a stationary, magnetized plasma . .	33
I.5	Coupling of Vlasov and Poisson equation	35
I.5.1	Debye shielding in a spherical well	35
I.5.2	Anti-shielding in a one-dimensional well	37
I.5.3	The Bohm Criterion	40
I.5.4	Helical upper bound and adiabatic limit currents	42
I.5.5	Quasicollisionless collection in a strongly magnetized plasma .	45
II	Solving the problem with the PIC code SCEPTIC	49
II.1	SCEPTIC Overview	49
II.1.1	The unit system	49
II.1.2	The equations	50

II.1.3	The Geometry	51
II.2	Development of a parallelized Poisson solver	52
II.2.1	Successive Over Relaxation	52
II.2.2	Parallel code structure	53
II.2.3	Performance expectation	53
II.2.4	Optimization	55
II.2.5	Test	55
II.3	Development of a symplectic magnetized particle mover	57
II.3.1	Motivation	57
II.3.2	Single particle Hamiltonian	58
II.3.3	Practical implementation	59
II.3.4	Benchmarking against direct orbit integration	61
II.4	The boundary conditions	62
II.4.1	Conditions on the potential	62
II.4.2	Particle reinjection	64
III	Solutions for a stationary plasma	67
III.1	Weakly-focusing and Strongly-focusing regimes	67
III.2	Space-charge distribution	68
III.2.1	Quasineutral plasma	68
III.2.2	Plasma with finite shielding	70
III.3	Total ion current to the probe	76
III.3.1	Dependence on β	76
III.3.2	Dependence on λ_{De}	77
III.3.3	Dependence on χ_p	79
III.4	Angular distribution of the ion current	82
III.4.1	Quasineutral regime	82
III.4.2	Plasma with finite shielding	83
IV	Solutions for a flowing plasma	85
IV.1	Cold ion orbits in a flowing plasma	85

IV.2	Space-charge distribution	91
IV.2.1	Quasineutral regime	91
IV.2.2	Plasma with finite shielding	94
IV.3	Total collected current	97
IV.4	Angular distribution of the ion current for weakly focusing probes . .	98
IV.4.1	Quasineutral regime	98
IV.4.2	Plasma with finite shielding and equithermal ions and electrons	102
IV.5	Flux asymmetry reversal suppression for strongly focusing probes . .	106
V	Conclusions	111
V.1	Review of our computation hypothesis	111
V.2	Implications of our results	112
V.3	Suggestions for future work	113
A	Low β expansion of Whipple-like integrals	115
A.1	Sphere at space potential in a drifting plasma	115
A.1.1	Current drawn from orbits in the magnetic shadow: ι^{in}	116
A.1.2	Current drawn from the other orbits: ι^{out}	116
A.1.3	Analysis of $t^*(s, t, u)$	117
A.1.4	Analysis of ι_L^{out}	119
A.1.5	Analysis of ι_C^{out}	120
A.1.6	Conclusion	121
A.2	Charged sphere in a stationary plasma: Upper bound	122
A.2.1	Current drawn from the orbits in the magnetic shadow: ι^{in} . .	123
A.2.2	Current drawn from the other orbits: ι^{out}	123
A.2.3	Analysis of ι_L^{Up}	123
A.2.4	Analysis of ι_C^{Up}	124
A.2.5	Conclusion	125
A.3	Charged sphere in a stationary plasma: Lower bound	125
A.3.1	Current drawn from the orbits in the magnetic shadow: ι_{in}^{Low} .	125
A.3.2	Analysis of ι_L^{Low}	126

A.3.3	Analysis of t_C^{Low}	126
A.3.4	Conclusion	126
B	Derivation of the OML currents to a sphere and infinite cylinder	127
B.1	Sphere	127
B.2	Infinite cylinder	129
B.3	Comparison of the OML current for the sphere and the cylinder . . .	131

List of Figures

I-1	Spherical and cylindrical coordinates of the problem	20
I-2	Collection orbits in the presence of a background magnetic field . .	26
I-3	Magnetized orbits parameterization	27
I-4	Ion current to a stationary spherical probe at space potential	29
I-5	Ion current to a drifting spherical probe at space potential	30
I-6	Ion and electron densities in a one-dimensional well	39
I-7	Bohm criterion in a half one-dimensional well	43
I-8	Helical upper bound as a function of β	45
I-9	Models of ion distribution function in a one-dimensional presheath .	47
II-1	Spherical mesh used in SCEPTIC	51
II-2	Principle of a SOR block-solver	54
II-3	Block-solver performance test	56
II-4	Schematic of the subcycling algorithm	60
II-5	Cyclotronic integrator benchmark	61
II-6	SCEPTIC physical domain	63
II-7	Models of differential fluxes for ion reinjection	65
III-1	Orbit interpretation of the probe focusing properties	68
III-2	Charge-density profiles dependence on β for $\bar{\lambda}_{De} = 0$	69
III-3	Charge-density contour plot evolution with β for $\bar{\lambda}_{De} = 0$	71
III-4	Charge-density contour plot evolution with \bar{T}_i for $\bar{\lambda}_{De} = 0$	72
III-5	Charge-density profiles dependence on β for $\bar{\lambda}_{De} \neq 0$	73
III-6	Charge-density contour plot evolution with $\bar{\lambda}_{De}$ for $\beta = 1$ and $\bar{T}_i = 0.1$	74

III-7	Potential contour plot evolution with $\bar{\lambda}_{De}$ for $\beta = 1$ and $\bar{T}_i = 0.1$. . .	75
III-8	Ion current as a function of β for $\bar{\lambda}_{De} = 0$	76
III-9	Ion current as a function of β for $\bar{\lambda}_{De} \neq 0$ and $\bar{T}_i = 1.0$	77
III-10	Ion current as a function of β for $\bar{\lambda}_{De} \neq 0$ and $\bar{T}_i = 0.3$	78
III-11	Ion current as a function of β for $\bar{\lambda}_{De} \neq 0$ and $\bar{T}_i = 0.1$	78
III-12	Variation of the slope factor C_β with $\bar{\lambda}_{De}$	79
III-13	Ion current dependence on $\bar{\lambda}_{De}$	80
III-14	Ion current dependence on χ_p	81
III-15	Angular dependence of the ion current for $\bar{\lambda}_{De} = 0$	82
III-16	Magnetic field induced asymmetry for $\bar{\lambda}_{De} = 0$	83
III-17	Angular dependence of the ion current for $\bar{\lambda}_{De} \neq 0$	84
IV-1	Orbit interpretation of the flux asymmetry reversal	86
IV-2	Evolution of the depletion cone with β	87
IV-3	Evolution of the depletion cone with $\bar{\lambda}_{De}$	88
IV-4	Charge-density profiles on axis for $\bar{\lambda}_{De} = 0$	91
IV-5	Magnetic field effect on Mach-cone shaped rarefactions	93
IV-6	Evolution of the ion density distribution with β for $\bar{\lambda}_{De} \neq 0$	95
IV-7	Evolution of the potential distribution with β for $\bar{\lambda}_{De} \neq 0$	96
IV-8	Wake in the supersonic, magnetized regime	97
IV-9	Ion current dependence on β for $\bar{\lambda}_{De} = 1$ and $\bar{T}_i = 1$	98
IV-10	Ion current dependence on β for $\bar{\lambda}_{De} = 1$ and $\bar{T}_i = 0.1$	99
IV-11	Angular dependence of the ion current for $\bar{\lambda}_{De} = 0$	100
IV-12	Mach-probe calibration factor for $\bar{\lambda}_{De} = 0$ and $\bar{T}_i = 1$	102
IV-13	Angular distribution of the ion current for $\bar{T}_i = 1.0$ and $\bar{\lambda}_{De} = 1.0$	103
IV-14	Angular distribution of the ion current for $\bar{T}_i = 1.0$ and $\bar{\lambda}_{De} = 0.1$	104
IV-15	Mach-probe calibration factor contour lines for $\bar{\lambda}_{De} \neq 0$ and $\bar{T}_i = 1$	105
IV-16	Mach-probe calibration factor for $\bar{\lambda}_{De} \neq 0$ and $\bar{T}_i = 1$	106
IV-17	Flux asymmetry reversal suppression by \mathbf{B} at $\bar{T}_i = 0.1$	107
IV-18	Mach-probe calibration factor for $\bar{\lambda}_{De} = 1.0$ and $\bar{T}_i = 0.1$	108

IV-19	Flux asymmetry reversal suppression by \mathbf{B} at $\bar{T}_i = 0.01$	109
B-1	OML current calculation: Sphere	128
B-2	OML current calculation: Infinite cylinder	130
B-3	Comparison of the spherical and cylindrical probes OML current . .	132

List of Tables

II.1	Fundamental units used with SCEPTIC	49
II.2	Dependent units in SCEPTIC.	50

Nomenclature

r_p	Probe radius
$T_{i,e}$	Ion (Electron) temperature
$v_{ti,e}$	Ion (Electron) thermal speed
Z	Ion charge
c_s	Sound speed (Ion acoustic waves)
γ	Ratio of specific heats for the ion species
n_∞	Electron density at infinity
Γ_i^0	Ion thermal charge flux density
I_i^0	Ion thermal current to the probe
$\lambda_{Di,e}$	Ion (Electron) Debye length
λ_s	Plasma shielding length
\mathbf{B}	Magnetic field
Ω	Larmor angular frequency
r_L	Ion mean Larmor radius
β	Probe radius over the Ion mean Larmor radius
$f_{i,e}^\infty$	Ion (Electron) distribution function at infinity
\mathbf{v}_d	Ion drift velocity
V	Electrostatic potential
ϕ	Electrostatic potential normalized to $\frac{T_e}{e}$
χ	Electrostatic potential normalized to $-\frac{T_i}{Ze}$
V_p	Probe potential

Chapter I

Analytical basis

I.1 Position of the problem

Since the early days of laboratory plasmas scientists have been interested in studying the behavior of bodies inserted in gas discharges. The pioneering work of Mott-Smith and Langmuir on the matter [1] was mainly motivated by the prospect of diagnosing the ions and electrons distribution functions in a plasma by measuring their current to a conducting wire, or *Langmuir* probe. Because we have today a good understanding of particle-flux sensing devices in several regimes of operation, such probes are still widely used in modern plasma diagnostics [4].

The theory of current collection in a plasma would not have aroused much interest outside the community of experimentalists if its applications were limited to diagnostic purposes. Fortunately dust particles in natural or artificial plasmas, as well as man-made satellites, obey the same physics of *Langmuir* probes. Unless otherwise indicated, the term “probe” will be used regardless of the physical nature of the collector.

An ideal probe absorbs every ion and electron striking it. In steady state, it will release neutral atoms and/or molecules at a rate that balances the incoming flux of ions, which has been neutralized by the incoming electrons or the electrons supplied by an external bias circuit. The deviations from ideality come from different *Solid state* physics reactions resulting in electron emission at the surface, whose relative

importance depends upon the experimental conditions. Usually the most relevant effects are Photoemission, Secondary emission, and Thermionic emission. A quantitative treatment showing how those phenomena can strongly influence the charging of dust particles has been performed by Delzanno and Bruno [5]. In some cases ion-induced secondary emission is present as well. Although the conditions for a probe to behave as ideal are rarely met in practice, we will work under the assumption that those conditions are fulfilled, and hence shall only be concerned by the current drawn from the bulk plasma. We also assume that the charge-exchange mean-free-path is much longer than the probe size, in order to neglect the interaction between the neutrals released by the probe and the incoming ions.

The electrostatic potential of Langmuir probes is artificially biased with respect to the surrounding plasma, usually negatively. Ideal floating probes (i.e. non connected to an external circuit) tend to charge negatively as well due to the high electron mobility [4]. In either case, relating the current to the plasma properties requires an understanding of how the probe potential locally perturbs the plasma, and hence the particle distributions. This interaction between the plasma and the collector is governed by basic *Plasma* physics, that we will study under the assumption that the probe can be idealized as a sphere. The geometry under consideration is illustrated in Fig. (I-1).

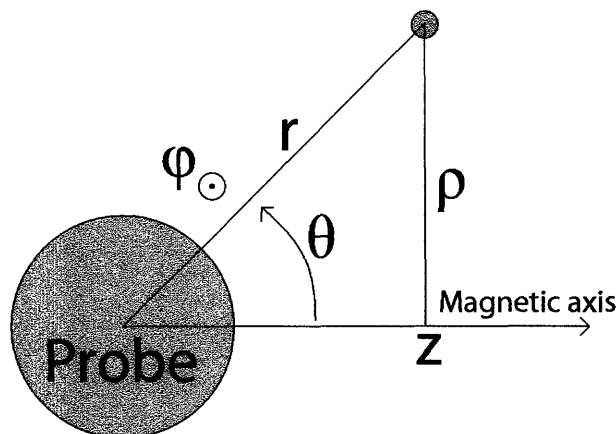


Figure I-1: Spherical and cylindrical coordinates of the problem. The magnetic axis (External \mathbf{B} -field) defines the \mathbf{z} -direction.

The unmagnetized problem (that is to say without background magnetic field) has been solved by Hutchinson [2, 3] in the limit of zero collisionality by means of the Particle in Cell (PIC) code SCEPTIC. The opposite limit of a strongly magnetized plasma ($\beta \gg 1$, where β is the probe radius divided by the mean ion Larmor radius) has been treated by Chung and Hutchinson [6, 7] through one-dimensional fluid and kinetic calculations in a “quasi-collisionless” plasma. In each case the angular distribution of ion current has been computed for a wide range of drift velocities and ion to electron temperature ratios.

The intermediate magnetic field regime ($\beta \sim 1$) has received non negligible attention, be it from an experimental [8] or an analytical [9, 10, 11, 12] point of view. Three dimensional PIC simulations of electron collection by a spherical satellite in a magnetoplasma flowing perpendicular to the magnetic field have been performed as well [14], however the results are rather crude and qualitative.

The main goal of the present thesis is to perform a comprehensive and quantitative study of ion collection by a negatively charged spherical probe using the code SCEPTIC under the condition of negligible collisionality, and in the presence of a weak magnetic field parallel to the drift velocity. The present Chapter summarizes existing theories necessary to an understanding of SCEPTIC operation and results, and develops new analytical expansions at low β to the current collected by a sphere at space potential. Chapter II gives an overview of the code operation, and of recent modifications necessary to implement the magnetic field. Chapter III presents the numerical results in the flow-free regime, while Chapter IV treats the drifting case.

I.2 Basic plasma properties

I.2.1 Infinite uniform plasmas

The simplest classical plasma is a uniform, infinite, isotropic, fully ionized neutral gas consisting of a single species of ions with mass m_i , charge Z and uniform density $n_i = n_\infty/Z$, and electrons with mass m_e and uniform density $n_e = n_\infty$. Because the

proton-to-electron mass ratio is extremely large ($\frac{m_H}{m_e} = 1836$) and thermalization is driven by Coulomb collisions, it is often the case that ions and electrons equilibrate among themselves much faster than with each other. Therefore the two species can be described by Maxwellian distributions with different temperatures $T_{i,e}$ and drift velocities $\mathbf{v}_{\mathbf{d},i,e}$.

If we define the thermal speed of a species by:

$$v_t = \sqrt{\frac{2T}{m}} \quad (\text{I.1})$$

the shifted Maxwellian distribution function $f^\infty(\mathbf{v})$, where $f^\infty(\mathbf{v})d^3\mathbf{v}$ is the number of particles in the velocity range $d^3\mathbf{v}$, is given by:

$$f^\infty(\mathbf{v}) = \frac{n}{(v_t\sqrt{\pi})^3} \exp\left(-\frac{(\mathbf{v} - \mathbf{v}_d)^2}{v_t^2}\right) \quad (\text{I.2})$$

By construction we have:

$$n = \int f^\infty(\mathbf{v})d^3\mathbf{v} \quad (\text{I.3})$$

$$\mathbf{v}_d = \int \mathbf{v}f^\infty(\mathbf{v})d^3\mathbf{v} \quad (\text{I.4})$$

$$T = \frac{1}{n} \int (\mathbf{v} - \mathbf{v}_d)^2 f^\infty(\mathbf{v})d^3\mathbf{v} \quad (\text{I.5})$$

$$(\text{I.6})$$

v_t appears as a measure of the random velocity of the particles, and is related to their mean kinetic energy by $\langle E_c \rangle = \frac{3}{4}mv_t^2$. The random flux-density is defined as the one-directional charge flux-density in a frame moving with velocity \mathbf{v}_d , where the plasma is therefore at rest:

$$\Gamma^0 = Z \int_{v_x \geq 0} f_{\mathbf{v}_d=0}^\infty(\mathbf{v})v_x d^3\mathbf{v} = Zn \frac{v_t}{2\sqrt{\pi}} \quad (\text{I.7})$$

If p_x is the diagonal value of the ion pressure tensor in the \mathbf{e}_x direction, the ratio

of specific heats along this direction, γ_x , is given by:

$$\gamma_x = \frac{1}{T} \frac{dp}{dn} \Big|_{dy=dz=0} \quad (\text{I.8})$$

We can now define the sound speed c_s in the \mathbf{e}_x direction as the speed of ion acoustic waves in the ion reference frame:

$$c_s = \frac{ZT_e + \gamma_x T_i}{m_i} \gtrsim v_{ti} \quad (\text{I.9})$$

In most plasma experiments the electron drift velocity is much smaller than the electron thermal speed ($|\mathbf{v}_{de}| \ll v_{te}$), it is therefore appropriate to consider the electrons as stationary. This thesis is based on this assumption, and from now on the term “drift velocity” refers to the ion species. The relevant values for the drift velocity range from zero to a few sound speeds.

I.2.2 Analytical current calculations

The theories and computations developed in this thesis, intended to calculate the ion current to a spherical probe, assume the ions and electrons far from the collector, or “at infinity”, to be described by the preceding model. Because the probe induces a local perturbation on the electrostatic fields and particle distribution functions, the ion flux density to the probe surface is not simply given by Eq. (I.7) with $n = n_\infty/Z$. Two main approaches can be followed when searching for analytic expressions for the steady-state current effectively collected by the probe, when collisions can be neglected.

Approach 1

The first approach is to use Vlasov’s equation, governing the temporal and spatial evolution of the distribution function:

$$\frac{df}{dt} \Big|_{\text{orbit}} = \frac{\partial f}{\partial t} + \mathbf{v} \cdot \nabla_x f + \frac{Ze}{m} (\mathbf{E} + \mathbf{v} \wedge \mathbf{B}) \cdot \nabla_v f = 0 \quad (\text{I.10})$$

Along an orbit, because phase-space density is conserved, $\frac{df}{dt} = 0$. If each orbit striking the probe can be traced back to infinity, the distribution function at the probe surface is straightforwardly given by:

$$f^{\text{probe}}(\mathbf{v}, \mathbf{x}) = f^\infty(\mathbf{v}_\infty) \quad (\text{I.11})$$

where \mathbf{v}_∞ is the velocity that a particle striking the probe with position (\mathbf{v}, \mathbf{x}) had at infinity. If v_n is the component of the velocity normal to the probe surface and directed inwards, the total current collected is:

$$I = Z \int_{\text{probe}} \int v_n f^{\text{probe}}(\mathbf{v}, \mathbf{x}) d^3\mathbf{v} d^3\mathbf{x} \quad (\text{I.12})$$

Unfortunately there are two situations where this approach can not be followed: When some orbits intersect the probe more than once, and when it is not possible to find an analytic relationship between (\mathbf{v}, \mathbf{x}) and \mathbf{v}_∞ .

Approach 2

When the preceding path fails, one can consider a control volume Ω containing the probe, but whose surface is at an arbitrary location where the distribution function is known, such as infinity. The collected current is:

$$I = Z \int_{\partial\Omega} \int_{v_n \geq 0} v_n f^\infty(\mathbf{v}) H(\mathbf{v}, \mathbf{x}) d^3\mathbf{v} d^3\mathbf{x} \quad (\text{I.13})$$

where $\partial\Omega$ is the surface of the control volume over which the integration is performed, v_n the velocity component normal to the control surface and directed inwards, and $H(\mathbf{v}, \mathbf{x})$ an impact parameter equal to 1 if a particle whose initial position in phase-space is (\mathbf{v}, \mathbf{x}) is collected, and 0 otherwise.

I.3 Free flight ion current to a spherical probe

I.3.1 Unmagnetized plasma

The *free flight* model of current collection is a collisionless model where any electric field is neglected. Therefore although we immediately specialize to the ions, this model can equivalently be applied to the electrons. Unmagnetized orbits emerging from a convex probe are therefore straight lines and connect to infinity, hence we can use the first approach described in Section I.2.2:

$$\Gamma_i^{ff} = Z \int_{v_n \geq 0} f_i^\infty(\mathbf{v}) v_n d^3\mathbf{v} \quad (\text{I.14})$$

The integration has been performed analytically in Ref. [2] in the case of a spherical probe with f_i^∞ given by Eq. (I.2) (See Fig. (I-1) for a description of the coordinate system).

$$\Gamma_i^{ff}(v_d, \cos \theta) = \Gamma_i^0 \left[\exp\left(-\left(\frac{v_d}{v_{ti}}\right)^2 \cos^2 \theta\right) - \sqrt{\pi} \operatorname{erfc}\left(\frac{v_d}{v_{ti}} \cos \theta\right) \frac{v_d}{v_{ti}} \cos \theta \right] \quad (\text{I.15})$$

By integrating Eq. (I.15) over the sphere we find the total current:

$$I_i^{ff} = I_i^0 \left[\frac{1}{2} \exp\left(-\frac{v_d^2}{v_{ti}^2}\right) + \frac{\sqrt{\pi}}{2} \left(\frac{v_d}{v_{ti}} + \frac{v_{ti}}{2v_d}\right) \operatorname{erf}\left(\frac{v_d}{v_{ti}}\right) \right] \quad (\text{I.16})$$

Here and in the rest of the Thesis, $\Gamma_i^0 = n_\infty \frac{v_{ti}}{2\sqrt{\pi}}$ is the ion random charge flux density (we recall that the ion density at infinity is n_∞/Z), and $I_i^0 = 4\pi r_p^2 \Gamma_i^0$ is the ion random thermal current collected by the sphere. Similar calculations for an infinite planar probe perpendicular to the plasma drift and collecting particles from both sides (total area of the two faces: A) yield:

$$I_i^{ff} = \Gamma_i^0 A \left[\exp\left(-\frac{v_d^2}{v_{ti}^2}\right) + \sqrt{\pi} \frac{v_d}{v_{ti}} \operatorname{erf}\left(\frac{v_d}{v_{ti}}\right) \right] \quad (\text{I.17})$$

I.3.2 Magnetized plasma with $v_d \parallel B$

The picture is more complicated in the presence of a background magnetic field, because as shown in Fig. (I-2) not all the orbits originating from the probe, be it convex, connect to infinity. We must therefore resort to the second approach described in Section I.2.2.

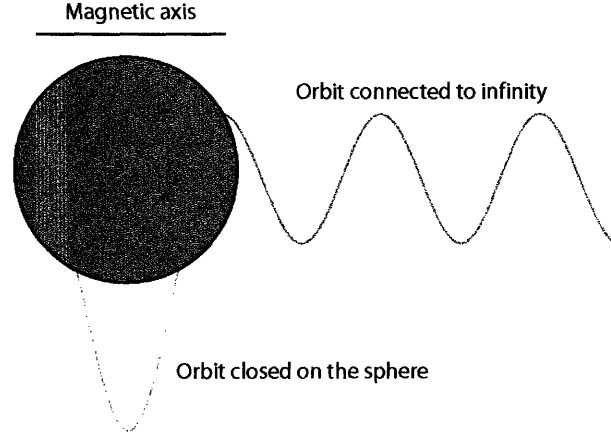


Figure I-2: Schematic representation of the two kind of orbits intersecting the probe. In a collisionless plasma, orbits that close on the sphere are empty.

The current to the probe depends on v_{ti} , v_d , and on the non-dimensional factor $\beta = r_p/r_L$, which is a measure of the magnetic field defined as the ratio of the probe radius over a mean ion gyroradius.

$$\beta = \frac{r_p}{\sqrt{\frac{\pi T_i m_i}{2Z^2 e^2 B^2}}} \quad (\text{I.18})$$

At $\beta = 0$, the current is given by Eq. (I.16):

$$I_i^{\beta=0} = I_i^0 \left[\frac{1}{2} \exp\left(-\frac{v_d^2}{v_{ti}^2}\right) + \frac{\sqrt{\pi}}{2} \left(\frac{v_d}{v_{ti}} + \frac{v_{ti}}{2v_d} \right) \text{erf}\left(\frac{v_d}{v_{ti}}\right) \right] \quad (\text{I.19})$$

In the limit $\beta \gg 1$, the particles are tight to the magnetic field lines and the total current is therefore given by Eq. (I.17) with $A = 2\pi r_p^2$ (double of the probe cross-section):

$$I_i^{\beta=\infty} = I_i^0 \frac{1}{2} \left[\exp\left(-\frac{v_d^2}{v_{ti}^2}\right) + \sqrt{\pi} \frac{v_d}{v_{ti}} \operatorname{erf}\left(\frac{v_d}{v_{ti}}\right) \right] \quad (\text{I.20})$$

In the intermediate magnetic field regime ($0 < \beta < \infty$), the current to a spherical electrode of radius unity at space potential can be evaluated by summing the contribution of helices of radius s , wave length $2\pi t$, guiding center distance to the magnetic axis of the probe u , and phase $\psi \in [0 : 2\pi]$ distributed according to a drifting Maxwellian (Only four variables are necessary to describe the helices because we have poloidal symmetry about the magnetic axis). Fig. (I-3) is a schematic of the problem:

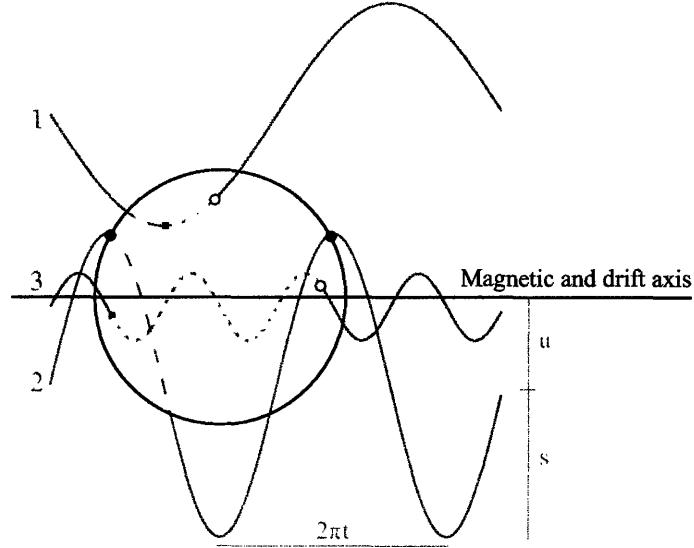


Figure I-3: Schematic of three different kind of orbits. Solid portions of orbits are visible, dashed portions are behind the sphere, and dotted portions are inside the probe. Orbit $n^{\circ}1$ has $s_1 + u_1 > 1$ and $|s_1 - u_1| < 1$. The phase ψ_1 is such that the orbit crosses the sphere, but because the wavelength is “long” ($t_1 > t_1^*(s_1, t_1, u_1)$, see Appendix A), there are phases $\tilde{\psi}$ such that $H(u_1, s_1, t_1, \tilde{\psi}) = 0$. Orbit $n^{\circ}2$, for which the geometrical meaning of s , t and u is shown, has $s_2 + u_1 > 1$ and $|s_2 - u_2| < 1$. It is a critical orbit because $H(u_2, s_2, t_2, \psi_2) = 1$ regardless of ψ_2 ($t_2 = t_2^*(s_2, t_2, u_2)$). Orbit $n^{\circ}3$ has $u_3 + s_3 < 1$, hence $H(u_3, s_3, t_3, \psi_3) = 1$ regardless of ψ_3 .

Stationary plasma

The calculation was first done in the stationary case ($v_d = 0$) by Whipple [9], whose expression can be recovered by setting $D = 0$ in Eq. (9) from Ref. [11].

$$\frac{I_i}{I_i^0} = \frac{1}{4}\pi^2\beta^4 \int_{s=0}^{\infty} \int_{t=0}^{\infty} \tilde{f}(\beta, s, t) \left[\frac{1}{2}\theta(1-s)(1-s)^2 + \int_{u=|s-1|}^{s+1} \frac{1}{2\pi} \int_{\psi=0}^{2\pi} H(u, s, t, \psi) u du \right] st ds dt \quad (\text{I.21})$$

with:

$$\tilde{f}(\beta, s, t) = \exp\left(-\frac{\pi}{4}\beta^2(s^2 + t^2)\right) \quad (\text{I.22})$$

I_i/I_i^0 (Eqs. (I.21,I.22)) can be seen as the current reduction factor from the value in an unmagnetized plasma. \tilde{f} is a form of the Boltzmann exponential appearing in the Maxwellian distribution function. The term $\frac{1}{2}\theta(1-s)(1-s)^2$ counts the orbits with $s+u < 1$, that we know for sure are collection orbits (θ is the Heaviside step function). The term $\int_{u=|s-1|}^{s+1} \frac{1}{2\pi} \int_{\psi=0}^{2\pi} H(u, s, t, \psi) u du$ counts the current collected from the orbits with $s+u \geq 1$ and $|u-s| \leq 1$. That is to say helices part in the magnetic shadow and part outside. The impact factor $H(u, s, t, \psi)$ (equal to 1 if the orbit characterized by (u, s, t, ψ) intersects the sphere at least once and 0 otherwise) has been calculated by Rubinstein and Laframboise in Ref. [11]. Orbits characterized by $u > s+1$ do not intersect the sphere.

This integral is expensive to evaluate as $\beta \rightarrow 0$ and was performed using a second order trapezoidal rule with adaptative step-size down to $\beta = 0.002$. The result is shown in Fig. (I-4).

I_i/I_i^0 can be approximated to within 0.3% by:

$$\frac{I_i}{I_i^0} = 1.000 - 0.0946z - 0.305z^2 + 0.950z^3 - 2.200z^4 + 1.150z^5 \quad \text{with} \quad z = \frac{\beta}{1+\beta}. \quad (\text{I.23})$$

We have shown (See Appendix A) by expansion starting from the integral expression of Eq. (I.21) that the slope of the current reduction at $\beta = 0$ is $C = 1/3\pi$, in agreement with our numerical integration. The linear term in Eq. (I.23) is slightly different from $-1/3\pi$ because this equation is not a Taylor expansion at $z = 0$ but a polynomial fitting over the range $z \in [0 : 1]$:

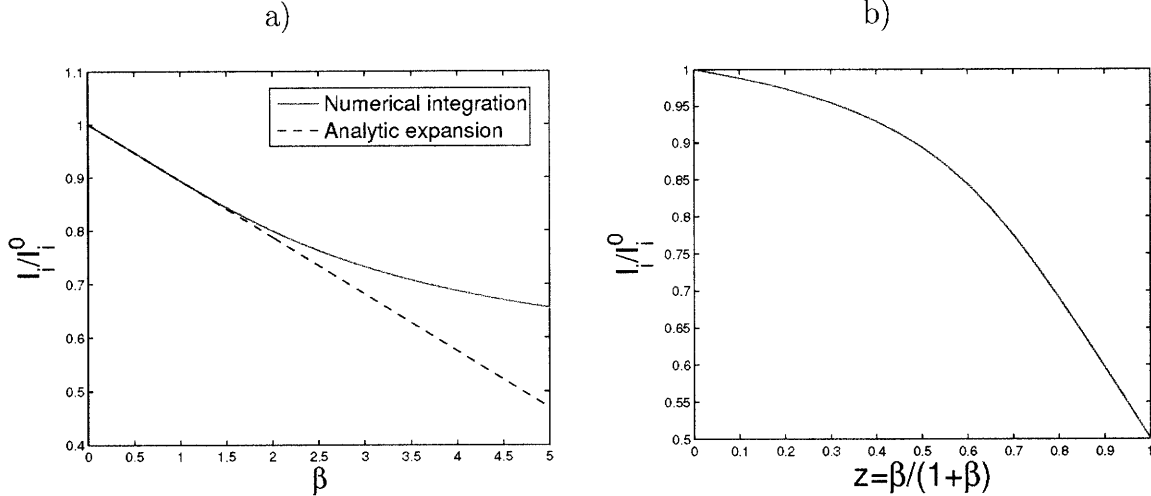


Figure I-4: Ion current collected by a stationary spherical probe at space potential (normalized to $I_i^0 = 4\pi r_p^2 n_\infty \frac{v_{ti}}{2\sqrt{\pi}}$) as a function of the magnetic field. Fig. a shows that the dependence at small β is given by Eq. (I.24). Fig. b shows the same function for the range $\beta \in [0 : \infty]$. If $\beta = 0$, the particle current is simply the sphere area times the random current: $I_i/I_i^0 = 1$. If $\beta = \infty$, the particle current is reduced by a factor of 2: $I_i/I_i^0 = 1/2$.

$$\frac{I_i(\beta)}{I_i^0} = 1 - \frac{1}{3\pi}\beta + O(\beta^2) \quad (\text{I.24})$$

Eq. (I.24) is in contradiction to the statement of Rubinstein and Laframboise (“Results and discussions” [11]) that the dependence on β is quadratic (i.e. $\iota(\beta) \sim 1 - C\beta^2$). The physical origin of this linear dependence can be understood as follows. We can choose a given point on the sphere surface, and consider the orbits there. Under the hypothesis of small β , the majority of those orbits can be traced back to infinity, while a small fraction re-intersect the probe at least once. Orbits that reintersect the sphere are unpopulated. It is this effect that entirely accounts for flux reduction. In order of magnitude, the reintersecting orbits require $|v_z| \lesssim r_p \Omega / \pi$, which delimits a solid angle proportional to $|v_z|$ (not v_z^2 as erroneously argued by Rubinstein and Laframboise). Since at small velocity the Maxwellian distribution is independent of \mathbf{v} , doubling β will simply double the fraction of such orbits, therefore doubling the depletion due to the magnetic field.

Drifting plasma

By setting:

$$\tilde{f}(\beta, s, t, \frac{v_d}{v_{ti}}) = \frac{1}{2} \left[\exp(-\frac{\pi}{4}\beta^2(s^2 + (t - \frac{v_d}{v_{ti}}\frac{2}{\beta\sqrt{\pi}})^2)) + \exp(-\frac{\pi}{4}\beta^2(s^2 + (t + \frac{v_d}{v_{ti}}\frac{2}{\beta\sqrt{\pi}})^2)) \right] \quad (\text{I.25})$$

in Eq. (I.21) we extended the previous theory to a plasma drifting parallel to the magnetic field.

The results of our numerical integration are shown in Fig. (I-5).

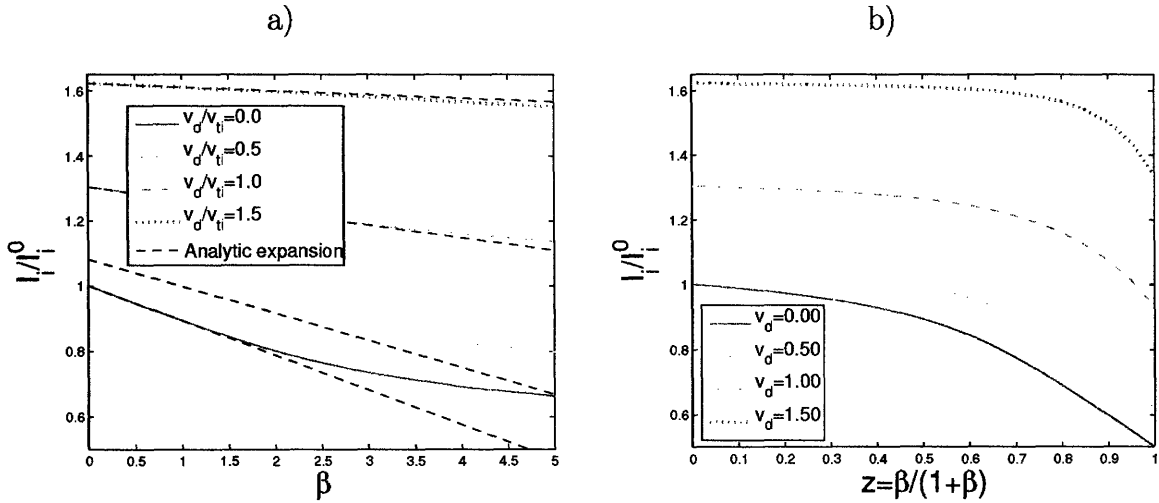


Figure I-5: Ion current collection by a spherical probe at space potential from a plasma drifting parallel to the magnetic field (normalized to $I_i^0 = 4\pi r_p^2 n_\infty \frac{v_{ti}}{2\sqrt{\pi}}$) as a function of the magnetic field β . Fig. a shows that the dependence at small β is given by Eq. (I.26). Fig. b shows the same functions for the range $\beta \in [0 : \infty]$. If $\beta = 0$, the particle current is given by Eq. (I.16). If $\beta = \infty$, the particle current is given by Eq. (I.17).

We show in Appendix A that the current dependence on β at small β is still linear, and given by:

$$\frac{I_i(\beta)}{I_i^0} = \left[\frac{1}{2} \exp(-\frac{v_d^2}{v_{ti}^2}) + \frac{\sqrt{\pi}}{2} (\frac{v_d}{v_{ti}} + \frac{v_{ti}}{2v_d}) \text{erf}(\frac{v_d}{v_{ti}}) \right] - \exp(-\frac{v_d^2}{v_{ti}^2}) \frac{\beta}{3\pi} + O(\beta^2) \quad (\text{I.26})$$

As can be seen in Eq. (I.26), the current slope at $\beta = 0$ is proportional to $\exp(-\frac{v_d^2}{v_{ti}^2})$ and therefore quickly decreases to zero as the drift rises. This is an intuitive result since for high drift velocities thermal motion perpendicular to the magnetic field can

be neglected, and the particles move along the field lines regardless of the magnitude of \mathbf{B} .

I.4 Basic charging mechanisms with non negligible electric fields

I.4.1 Electron density

In most situations where the electric fields can not be neglected, the ion current to the probe departs from the value given by Eqs (I.21,I.25). Because in this thesis we only consider negatively charged probes, we refer to the electrons as the “repelled species” and to the ions as the “attracted species”.

If nowhere in the plasma surrounding the probe the electrostatic potential is lower than the probe potential V_p , and if we can neglect the electron density depletion due to their collection, each point in the electron phase-space is connected to infinity. Those two conditions are always satisfied provided the probe potential is negative enough, typically $\phi_p \lesssim -1$ where we define the dimensionless potential as $\phi = \frac{eV}{T_e}$; and we are a fraction of r_p away from the probe surface. Recalling that the electron distribution is stationary and isotropic at infinity we have :

$$f_e(\mathbf{x}, \mathbf{v}) = f_e^\infty(\mathbf{v}^2 - v_{te}^2 \phi) \quad (\text{I.27})$$

, hence

$$n_e = n_\infty \exp(\phi) \quad (\text{I.28})$$

Obviously at the probe edge the density is lower than the value given by Eq. (I.28) since the orbits whose velocity is directed outwards are not populated.

I.4.2 Orbital Motion Limited ion current in an unmagnetized plasma

Bernstein and Rabinowitz [15] have shown that for the attracted species, each phase-space point with positive energy and velocity directed inwards at the surface of a spherical probe surrounded by a spherically symmetric potential distribution is populated only if the following inequality is satisfied:

$$\forall r, \frac{d}{dr} \left[r^3 \frac{d\phi}{dr} \right] \geq 0 \quad (\text{I.29})$$

That is to say the potential must decrease everywhere slower than $1/r^2$. This condition is satisfied in the limit $\lambda_s \gg r_p$, where $\lambda_s \propto 1/\sqrt{n_\infty}$ is the plasma shielding length (See Section I.5.1). Indeed in the limit $\lambda_s \rightarrow \infty$ the density of the plasma at infinity goes to zero and the potential distribution approaches a Coulomb form ($\phi \propto 1/r$). The current drawn by the probe in the limit of zero shielding is usually called ‘‘Orbital Motion Limited’’ (OML) current.

Conservation of energy (E_0) and angular momentum (J_0) for a given ion reads, provided the potential distribution is spherically symmetric:

$$E_0 = \frac{1}{2} m \dot{r}^2 + E_{eff}(r) \quad (\text{I.30})$$

where:

$$E_{eff}(r) = \frac{1}{2} \frac{J_0^2}{m r^2} + ZeV(r) \quad (\text{I.31})$$

is the effective potential of the radial motion. If the OML conditions are satisfied (i.e. the shielding is negligible), the potential distribution is indeed spherically symmetric, and Eqs (I.29,I.31) show that there is no intermediate barrier in the effective potential, hence Bernstein and Rabinowitz result holds.

Unfortunately we can not follow the first approach from Section I.2.2 to calculate the ion current to the probe because when the drift velocity is non zero, it does not appear possible to find an analytical relationship between (\mathbf{x}, \mathbf{v}) at the probe edge and \mathbf{v}_∞ , the corresponding velocity at infinity. We must therefore resort to the second

approach. Energy and angular momentum conservation imply that each particle with impact parameter p and energy E_0 such as:

$$p \leq r_p \sqrt{1 - \frac{ZeV_p}{E_0}} \quad (\text{I.32})$$

is collected.

For a drifting maxwellian distribution at infinity, the total current to the probe can be written as (See Appendix B):

$$I_i = \frac{n_\infty}{(v_{ti}\sqrt{\pi})^3} \int_{\theta=0}^{2\pi} \int_{v_z=-\infty}^{\infty} \int_{v_\rho=0}^{\infty} \exp\left(-\frac{(\mathbf{v} - \mathbf{v}_d)^2}{v_{ti}^2}\right) |\mathbf{v}| \pi r_p^2 \left(1 - \frac{ZeV_p}{E_0}\right) dv_z v_\rho dv_\rho d\theta \quad (\text{I.33})$$

Integration of Eq. (I.33) for $ZeV_p < 0$ gives:

$$\frac{I_i}{I_i^0} = \frac{1}{2} \exp\left(-\frac{v_d^2}{v_{ti}^2}\right) + \frac{\sqrt{\pi}}{2} \left[\frac{v_d}{v_{ti}} + \frac{v_{ti}}{2v_d} + \chi_p \frac{v_{ti}}{v_d} \right] \text{erf}\left(\frac{v_d}{v_{ti}}\right) \quad (\text{I.34})$$

Where χ is the ion-energy normalized potential ($\chi = -\frac{ZeV}{T_i}$), and χ_p the probe potential. Eq. (I.34) has first been derived by Whipple [13], and independently by Hutchinson [3].

By setting $v_d = 0$ we recover the formula first derived by Langmuir [1]:

$$I_i = I_i^0 (1 + \chi_p) \quad (\text{I.35})$$

Similar calculations, to the author's knowledge never published for a drifting plasma, can be performed for an infinite cylindrical probe, and are presented in Appendix B.

I.4.3 Canonical upper-bound in a stationary, magnetized plasma

When the OML conditions are satisfied, the total energy and the three components of the angular momentum about the probe center are conserved, that is to say four quantities. When the plasma is magnetized, we are left with only 2 conserved quantities.

In cylindrical coordinates (See Fig. I-1) those are the Energy

$$E_0 = \frac{m_i}{2}(v_\rho^2 + v_z^2 + v_\varphi^2) + ZeV \quad (\text{I.36})$$

and the canonical angular momentum about the magnetic axis

$$J_\varphi = m_i \rho^2 \frac{d\varphi}{dt} + \frac{1}{2} ZeB \rho^2 \quad (\text{I.37})$$

Combination of Eq. (I.36) and Eq. (I.37) gives:

$$E_0 = \frac{m_i}{2}(\dot{\rho}^2 + \dot{z}^2) + ZeV + \frac{m_i}{2} \rho^2 \left[\frac{J_\varphi}{m_i \rho^2} - \frac{ZeB}{2m_i} \right]^2 \quad (\text{I.38})$$

Because $\dot{\rho}^2 + \dot{z}^2 \geq 0$, a particle is confined in a “magnetic bottle”, defined by the following implicit equation:

$$E_0 - ZeV(z, \rho) - \frac{m_i}{2} \rho^2 \left[\frac{J_\varphi}{m_i \rho^2} - \frac{ZeB}{2m_i} \right]^2 \leq 0 \quad (\text{I.39})$$

One can easily solve Eq. (I.39) for ρ_∞ in the case of a cold plasma with drift velocity $\mathbf{v}_d \parallel \mathbf{B}$. The conserved quantities are $E_0 = \frac{m_i}{2} v_d^2$ and $J_\varphi = \frac{m_i}{2} ZeB \rho_\infty^2$, therefore:

$$\rho_\infty \leq \rho \sqrt{1 + \frac{2m_i}{ZeB} \sqrt{\frac{2}{m_i \rho^2} \left(\frac{1}{2} m_i v_d^2 - ZeV(\rho, z) \right)}} \quad (\text{I.40})$$

The maximum impact parameter for a particle to be collected is hence given by Eq. (I.41) by setting $V = V_p$ and $\rho = r_p$. This has first been done by Parker and Murphy [10] for a cold stationary plasma:

$$\rho_{PM} = r_p \sqrt{1 + \frac{2m_i}{ZeB} \sqrt{\frac{-2ZeV_p}{m_i r_p^2}}} \quad (\text{I.41})$$

They then calculated an upper bound to the collected current (Usually called canonical current) by assuming that at infinity the plasma still has a small thermal motion, thus obtaining:

$$I_i \leq I_i^{PM} = 2 \left[\frac{v_t}{2\sqrt{\pi}} (\pi \rho_{PM}^2) \right] = I_i^0 \left[\frac{1}{2} + \frac{2}{\sqrt{\pi}} \frac{\sqrt{\chi_p}}{\beta} \right] \quad (\text{I.42})$$

Later, Rubinstein and Laframboise [11] extended Parker's result to a stationary Maxwellian plasma with arbitrary temperature. Their expression, given in Eqs (30,33,35) from the previous reference, has a simple asymptotic form when $\chi_p = -\frac{ZeV_p}{T_i} \gg 1$:

$$\lim_{\chi_p \gg 1} I_i^{\text{Canonical}} = I_i^0 \left[\frac{1}{2} + \frac{2}{\sqrt{\pi}} \frac{\sqrt{\chi_p}}{\beta} + \frac{2}{\pi\beta^2} \right] \quad (\text{I.43})$$

$I_i^{\text{Canonical}}$ goes to I_i^{PM} when $\beta \rightarrow \infty$ as expected. No further investigation in the flowing case has been performed because as can be seen in Eq. (I.41), the maximum impact parameter grows with v_d , while in the limit of large v_d the particles only see the cross section of the probe perpendicular to the drift (and magnetic) axis. Therefore the optimal usefulness of this theory is at $v_d = 0$.

I.5 Coupling of Vlasov and Poisson equation

I.5.1 Debye shielding in a spherical well

Because we are in this thesis only concerned about the system “plasma+probe” in steady state (i.e. we shall not consider plasma waves), the electromagnetic fields are governed by Gauss and Ampere laws:

$$\begin{aligned} \nabla \cdot \mathbf{E} &= e \frac{Zn_i - n_e}{\epsilon_0} \\ \nabla \wedge \mathbf{B} &= e\mu_0(\Gamma_i - \Gamma_e) \end{aligned} \quad (\text{I.44})$$

where $\Gamma_{i,e}$ are the ion and electron charge-flux densities. This set of equations gives $E/B \sim c^2/v_{te}$ ($c^2\epsilon_0\mu_0 = 1$). Because typical thermal velocities are much smaller than c , it is usually possible to ignore the magnetic field generated by the local currents.

Therefore modifying Eq. (I.7) in order to account for the electric field generated by the probe itself (but not for any eventual background fields) requires the self-

consistent solution of Eq. (I.10) and Gauss equation that we rewrite under the form of Poisson's equation:

$$\nabla^2 \phi = \frac{1}{\lambda_{De}^2} (Zn_i - n_e) / n_\infty \quad (\text{I.45})$$

where $\lambda_{De} = \sqrt{\frac{T_e \epsilon_0}{e^2 n_\infty}}$ is the electron Debye length.

For a spherical probe in a stationary plasma, a perturbative analysis of the coupled Vlasov-Poisson equation can be performed in a region far from the probe where $V = V^1 \ll T_e/e$ ($-\nabla V^1 = \mathbf{E}^1$) by assuming the ion distribution function to be the unperturbed Maxwellian f_i^0 given by Eq. (I.2) plus a perturbation f_i^1 . Because the problem is spherically symmetric, Eq. (I.10) for the ions becomes, to first order:

$$v_r \frac{\partial f_i^1}{\partial r} + \frac{Ze}{m_i} E_r^1 \frac{\partial f_i^0}{\partial v_r} = 0 \quad (\text{I.46})$$

$$f_i^1 = - \int_{\tilde{r}=\infty}^r \frac{Ze E_r^1}{m_i v_r} \frac{\partial f_i^0}{\partial v_r} d\tilde{r} \quad (\text{I.47})$$

$$= \int_{\tilde{v}=0}^{V^1} \frac{Ze}{m_i v_r} \frac{\partial f_i^0}{\partial v_r} d\tilde{V} \quad (\text{I.48})$$

The integrand is readily evaluated from Eq. (I.2):

$$\frac{1}{v_r} \frac{\partial f_i^0}{\partial v_r} = - \frac{2f_i^0}{v_{ti}^2} \quad (\text{I.49})$$

Because $\int f_i^0(\mathbf{v}) d^3\mathbf{v} = n_\infty/Z$, the ion density perturbation $n_i^1 = \int f_i^1(\mathbf{v}) d^3\mathbf{v}$ is simply:

$$n_i^1 = -n_\infty \frac{2e}{m_i v_{ti}^2} V^1 = -n_\infty \frac{e}{T_i} V^1 \quad (\text{I.50})$$

By analogy $n_e^1 = n_\infty \frac{e}{T_e} V^1$, which is the first order expansion of the exact electron density given by Eq. (I.28).

Therefore Poisson's equation becomes:

$$\nabla^2\phi = \frac{1}{\lambda_{De}^2} \left[\left(1 - \frac{ZeV}{T_i}\right) - \left(1 + \frac{eV}{T_e}\right) \right] \quad (\text{I.51})$$

which can be rewritten as:

$$\nabla^2\phi = \frac{\phi}{\lambda_{De}^2} (1 + ZT_e/T_i) \quad (\text{I.52})$$

The solution of Eq. (I.52) is the well known Debye-Hückel potential:

$$\phi(r) = \phi_p \exp\left(-\frac{r - r_p}{\lambda_s}\right) \quad (\text{I.53})$$

where ϕ_p is the probe potential and λ_s is the linearized shielding length:

$$\lambda_s = \frac{\lambda_{De}}{\sqrt{1 + ZT_e/T_i}} \quad (\text{I.54})$$

Because the Debye-Hückel potential (Eq. (I.53)) has been calculated by assuming $\phi = \phi^1 \ll 1$ and by neglecting ion collection, it only gives an indication of the characteristic scale length over which the potential decays: λ_s .

I.5.2 Anti-shielding in a one-dimensional well

In the preceding section we derived a first order correction to the stationary Maxwellian distribution of ions to account for the presence of a small electrostatic potential χ^1 : $f_i(\mathbf{v}, \chi(\mathbf{x})) = f_i^0(\mathbf{v}) + f_i^1(\mathbf{v}, \chi(\mathbf{x}))$. In order to do so we assumed that $\forall \mathbf{v}, f_i^1(\mathbf{v}, \chi(\mathbf{x})) \ll f_i^0(\mathbf{v})$, which is incorrect for some \mathbf{v} . For convenience we work in this section with the ion-energy normalized potential χ

In the absence of background magnetic field and far from any boundary, if the ions are accelerated in a spherical potential well, conservation of energy along the orbits implies that

$$\forall \mathbf{v} \mid v^2 < v_{ti}^2 \chi \quad : \quad f_i(\mathbf{v}) = 0 \quad (\text{I.55})$$

Therefore for a small potential perturbation χ^1 :

$$f_i^{3D}(\mathbf{v}) = \begin{cases} f^0(\mathbf{v}) + f^1(\mathbf{v}, \chi(\mathbf{x})) & \text{If } v^2/v_{ti}^2 - \chi \geq 0 \\ 0 & \text{If } v^2/v_{ti}^2 - \chi < 0 \end{cases} \quad (\text{I.56})$$

The volume in velocity space where $f_i^{3D} = 0$ is proportional to $(\chi^1)^{3/2}$, and to first order in χ^1 the ion density is still given by $n_i = (n_\infty/Z)(1 + \chi^1)$ (Eq. (I.50)).

However if the ions are accelerated in a one-dimensional well (such as an infinite planar transparent grid placed at $z=0$) energy conservation reads:

$$\forall \mathbf{v} \mid v_z^2 < v_{ti}^2 \chi \quad : \quad f(\mathbf{v}) = 0 \quad (\text{I.57})$$

Therefore for a small potential perturbation χ^1 :

$$f_i^{1D}(\mathbf{v}) = \begin{cases} f_i^0(\mathbf{v}) + f_i^1(\mathbf{v}, \phi(\mathbf{x})) & \text{If } v_z^2/v_{ti}^2 - \chi \geq 0 \\ 0 & \text{If } v_z^2/v_{ti}^2 - \chi < 0 \end{cases} \quad (\text{I.58})$$

The volume in velocity space where $f_i^{1D} = 0$ is proportional to $(\phi^1)^{1/2}$, therefore the ion density is not given by Eq. (I.50) but goes as $n_i \propto (1 - C\sqrt{\chi^1})$. This expression is problematic when inserted in Poisson's equation. Indeed Eq. (I.52) becomes:

$$\nabla^2 \phi \propto -\sqrt{\phi} \quad (\text{I.59})$$

There is no solution to Eq. (I.59) with value at $z = 0$ of χ_p and limit at infinity of 0, while physically those are the limits the potential must have: For a one-dimensional problem, our collisionless model is inconsistent.

In a stationary plasma, it is actually possible to derive the distribution functions f_i^{1D} and f_i^{3D} without assuming $|\phi| \leq 1$ by taking advantage of phase-space density and energy conservation along an orbit:

$$f_i^{3D}(\mathbf{v}) = \begin{cases} \frac{n_\infty/Z}{(v_{ti}\sqrt{\pi})^3} e^{-v^2/v_{ti}^2 + \chi} & \text{If } v^2/v_{ti}^2 - \chi \geq 0 \\ 0 & \text{If } v^2/v_{ti}^2 - \chi < 0 \end{cases} \quad (\text{I.60})$$

and

$$f_i^{1D}(\mathbf{v}) = \begin{cases} \frac{n_\infty/Z}{(v_{ti}\sqrt{\pi})^3} e^{-v^2/v_{ti}^2 + \chi} & \text{If } v_z^2/v_{ti}^2 - \chi \geq 0 \\ 0 & \text{If } v_z^2/v_{ti}^2 - \chi < 0 \end{cases} \quad (\text{I.61})$$

Integration over the entire velocity space gives:

$$Zn_i^{3D}/n_\infty = \frac{2}{\sqrt{\pi}}\sqrt{\chi} + \exp(\chi)\text{erfc}(\sqrt{\chi}) \geq 1 \quad (\text{I.62})$$

$$Zn_i^{1D}/n_\infty = \exp(\chi)\text{erfc}(\sqrt{\chi}) \leq 1 \quad (\text{I.63})$$

Fig. (I-6) shows the densities as a function of χ in the one-dimensional case, when $Z = 1$ and $T_i = ZT_e$ (i.e. $\chi = -\phi$). The potential is assumed to decay monotonically from the probe to infinity, in order for a one-to-one relationship between z and χ to exist.

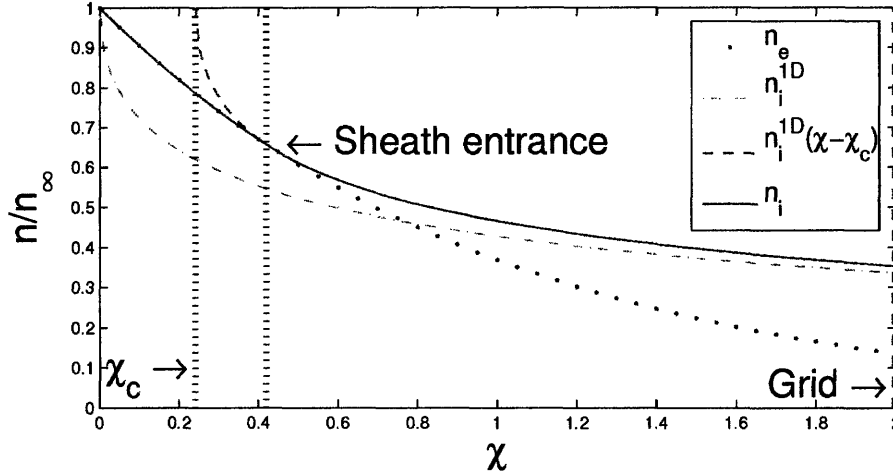


Figure I-6: Ion and electron charge densities as a function of the ion-energy normalized potential χ in the sheath and presheath of an infinite planar transparent grid.

In Fig. (I-6), the black dotted line is the electron density, given by $n_e = n_\infty \exp(\phi)$, upon which nothing can be done. The red dash-dotted line is the ion density given by Eq. (I.63). We see that for $\chi \leq 0.77$, n_i^{1D} is smaller than n_e , therefore the shielding is negative and the potential can not go from $\chi = 0.77$ to $\chi = 0$. If however the presheath is collisional or turbulent, energy conservation can be relaxed and the ion

density is not given by Eq. (I.63) anymore. Qualitatively, momentum loss in the presheath implies that at a point of potential χ , the ion distribution has only been accelerated by an amount $\tilde{\chi} \leq \chi$. The ion density curve in the collisionless sheath is then n_i^{1D} shifted by the amount χ_c necessary for this curve and the electron density curve to be tangent (Blue dashed curve). The point of tangency, situated at χ_s , is the sheath entrance. For $\chi > \chi_s$ we have $n_i > n_e$, while for $\chi < \chi_s$: $n_i \sim n_e$ (Collisional Presheath). The full blue curve is therefore a schematic curve of the “real” ion density. Obviously the quantitative value of n_i depends on the collisional processes.

I.5.3 The Bohm Criterion

A noticeable property of the sheath entrance (In a one-dimensional well) is that at this point, the ion average velocity equals the sound speed. While this can easily be shown for negligible ion temperature [4], the demonstration in the general case is more involved [16]. We here content ourselves to verify the property on a particular case.

We consider a spherical probe immersed in a strong magnetic field in order for the ions to be tight to the field lines. Because the probe is not transparent, the ion distribution function in the magnetic shadow at a point of potential χ is given by one half of $f_i^{1D}(\tilde{\chi})$, where $\tilde{\chi} = \chi - \chi_c$.

$$f_i(\chi, v_z) = \begin{cases} \frac{n_\infty/Z}{(v_{ti}\sqrt{\pi})^3} \cdot e^{-v^2/v_{ti}^2 + \tilde{\chi}} & \text{If } v_z/v_{ti} - \sqrt{\tilde{\chi}} \geq 0 \\ 0 & \text{If } v_z/v_{ti} - \sqrt{\tilde{\chi}} < 0 \end{cases} \quad (\text{I.64})$$

One can take the first moments of this distribution function as follows:

$$n_i(\chi) = \frac{n_\infty/Z}{v_{ti}\sqrt{\pi}} \int_{v_{ti}\sqrt{\tilde{\chi}}}^{\infty} \exp\left(-\frac{v_z^2 - v_{ti}^2\tilde{\chi}}{v_{ti}^2}\right) dv_z = \frac{n_\infty}{2Z} \exp(\tilde{\chi}) \operatorname{erfc}(\sqrt{\tilde{\chi}}) \quad (\text{I.65})$$

$$\langle v_z \rangle(\chi) = \frac{n_\infty/Z}{n_i(\tilde{\chi})} \frac{1}{v_{ti}\sqrt{\pi}} \int_{v_{ti}\sqrt{\tilde{\chi}}}^{\infty} v_z \exp\left(-\frac{v_z^2 - v_{ti}^2\tilde{\chi}}{v_{ti}^2}\right) dv_z = \frac{v_{ti}}{2\sqrt{\pi}} \frac{n_\infty/Z}{n_i(\chi)} \quad (\text{I.66})$$

$$\begin{aligned} T_i^{eff}(\chi) &= \frac{n_\infty/Z}{n_i(\tilde{\chi})} \frac{1}{v_{ti}\sqrt{\pi}} \int_{v_{ti}\sqrt{\tilde{\chi}}}^{\infty} [v_z - \langle v_z \rangle(\tilde{\chi})]^2 \exp\left(-\frac{v_z^2 - v_{ti}^2\tilde{\chi}}{v_{ti}^2}\right) dv_z \\ &= \frac{n_\infty v_{ti}^2/Z}{2\pi \operatorname{erfc}(\sqrt{\tilde{\chi}})^2} \left\{ 2\sqrt{\tilde{\chi}}\sqrt{\pi} \exp(-\tilde{\chi}) \operatorname{erfc}(\sqrt{\tilde{\chi}}) \right. \\ &\quad \left. + \pi \left[1 + \operatorname{erf}(\sqrt{\tilde{\chi}})^2 - 2\operatorname{erf}(\sqrt{\tilde{\chi}}) \right] - 2 \exp(-2\tilde{\chi}) \right\} \quad (\text{I.67}) \end{aligned}$$

where n_i is the ion density, $\langle v_z \rangle$ the average velocity, and T_i^{eff} the effective temperature. T_i^{eff} is different from T_i because the distribution function evolves with the potential and starts from a truncated Maxwellian. In order to calculate the sound speed, we need the ratio of specific heats in the \mathbf{z} -direction as defined in Eq. (I.8):

$$c_s(\chi) = \sqrt{T_i^{eff}(\chi)\gamma(\chi) + ZT_e} \quad \text{with} \quad \gamma(\chi) = \frac{1}{T_i^{eff}(\chi)} \frac{dP_i}{d\chi} / \frac{dn_i}{d\chi} \quad (\text{I.68})$$

where the pressure P_i is simply:

$$P_i(\chi) = n_i(\chi)T_i^{eff}(\chi) \quad (\text{I.69})$$

Derivation of the moments with respect to χ (or $\tilde{\chi}$) yields:

$$\frac{dn_i}{d\chi} = \frac{n_\infty/Z}{2} \exp(\tilde{\chi}) \operatorname{erfc}(\sqrt{\tilde{\chi}}) - \frac{n_\infty/Z}{2\sqrt{\pi}\sqrt{\tilde{\chi}}} \quad (\text{I.70})$$

$$\begin{aligned} \frac{dP}{d\chi} &= \frac{n_\infty v_{ti}^2/Z}{4\pi^2 \operatorname{erfc}(\sqrt{\tilde{\chi}})^2} \left\{ -2\sqrt{\frac{\pi}{\tilde{\chi}}} \exp(-2\tilde{\chi}) + \pi^2 \exp(\tilde{\chi}) \right. \\ &\quad \left. \left[1 + 3\operatorname{erf}(\sqrt{\tilde{\chi}})^2 - 3\operatorname{erf}(\sqrt{\tilde{\chi}}) - \operatorname{erf}(\sqrt{\tilde{\chi}})^3 \right] \right. \\ &\quad \left. + 2\pi \operatorname{erfc}(\sqrt{\tilde{\chi}}) \exp(-\tilde{\chi}) \right\} \quad (\text{I.71}) \end{aligned}$$

The sheath entrance is the point where the electron and ion charge-density curves are tangent, that is to say:

$$\begin{cases} Z \frac{dn_i}{d\chi} = \frac{dn_e}{d\chi} \\ Zn_i = n_e \end{cases} \quad (\text{I.72})$$

Because $n_e = n_\infty \exp(\phi) = n_\infty \exp(-\chi T_i / Z T_e)$, the sheath entrance potential χ_s is such that:

$$\frac{dn_i}{d\chi}(\chi_s) + \frac{T_i}{Z T_e} n_i(\chi_s) = 0 \quad (\text{I.73})$$

At $\chi = \chi_s$ one can then explicitly verify that $\langle v_z \rangle(\chi) = c_s(\chi)$. Fig. (I-7) is a graphical illustration of this property for the special case $T_i = Z T_e$.

The quasineutrality break-down in a one-dimensional potential well at the point where $\langle v_i \rangle = c_s$ is called Bohm criterion. We will take advantage of it in Chapter III, when the regime $\lambda_{De} \ll r_p$ will be studied in more detail.

I.5.4 Helical upper bound and adiabatic limit currents

The ion current to a stationary spherical probe in a collisionless magnetoplasma when the magnetic field is finite is framed by its value at $\beta = 0$ and its value at $\beta = \infty$. The first bound is simply Eq. (I.35), while the second is independent of the probe potential by virtue of flux conservation, and is given by Eq. (I.20) after setting $v_d = 0$.

$$I_i^{\beta=\infty} = \frac{1}{2} I_i^0 \quad (\text{I.74})$$

In order to improve this framing, the idea developed by Rubinstein and Laframboise [11] is to assume that the effects of orbit depletion due to multiple intersections with the probe occur in a neighborhood of the probe where the ions have already been accelerated by χ_p .

A lower bound is obtained by assuming that the portion of the ion distribution function whose velocity is directed towards the probe at the entrance of the neighborhood is given by f_i^{1D} (Eq. (I.61)). An upper bound, called ‘‘Helical’’ in order to

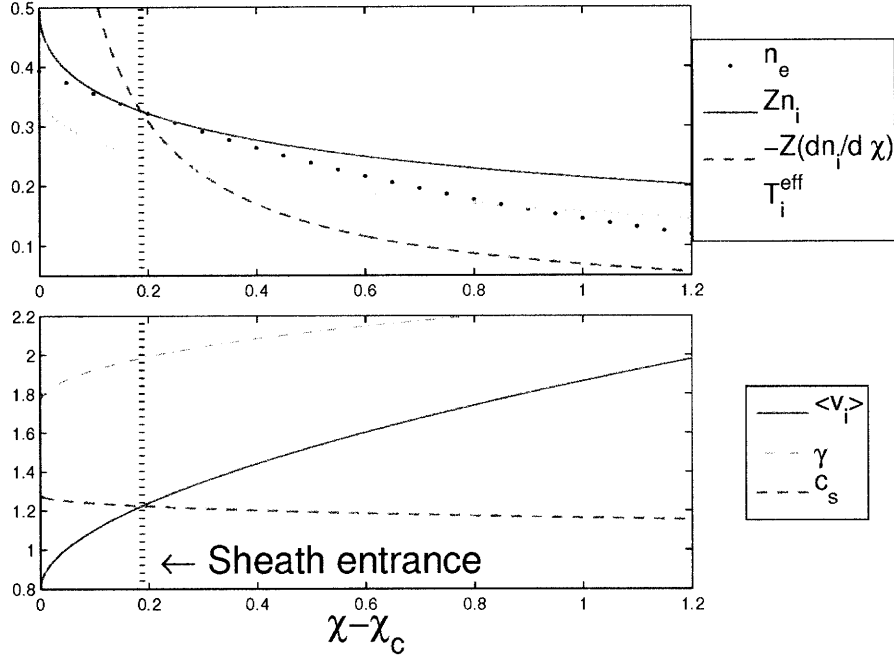


Figure I-7: Evolution of different physical quantities with $\tilde{\chi} = \chi - \chi_c$ for the ion distribution function given in Eq. (I.64), traced using the analytical formulas derived in this section. For this example we take $T_i = ZT_e$. n_e and Zn_i are in units of n_∞ , T_i^{eff} in units of ZT_e , $\langle v_i \rangle$ and c_s in units of $\sqrt{ZT_e/m_i}$. One sees that the point where $c_s = \langle v_i \rangle$ coincides with the point where $\frac{dn_i}{d\chi} = -T(\chi)n_i(\chi)$. At this point the ion and electron charge-density curves are tangent: this is the Bohm criterion.

avoid a confusion with the ‘‘Canonical’’ bound (Eq. (I.43)), is obtained taking this portion of distribution function to be given by f_i^{3D} .

The normalized current can therefore be written as:

$$\frac{I_i}{I_i^0} = \frac{\exp(\chi_p)}{4} \pi^2 \beta^4 \int_{s=0}^{\infty} \int_{t=0}^{\infty} \tilde{\theta}(\beta, \chi, s, t) \tilde{f}(\beta, s, t) \left[\frac{1}{2} \theta(1-s)(1-s)^2 + \int_{u=|s-1|}^{s+1} \frac{1}{2\pi} \int_{\psi=0}^{2\pi} \text{H}(u, s, t, \psi) u du \right] st ds dt \quad (\text{I.75})$$

with \tilde{f} given by Eq. (I.22), $\tilde{\theta}$ given by

$$\tilde{\theta}(\beta, \chi, s, t) = \begin{cases} \theta(t-D) & \text{For the lower bound} \\ \theta(s^2 + t^2 - D^2) & \text{For the upper bound} \end{cases} \quad (\text{I.76})$$

and D defined by :

$$D = \frac{2}{\beta} \sqrt{\frac{\chi_p}{\pi}} \quad (\text{I.77})$$

We demonstrate in Appendix A that:

$$\frac{I_i^{Up}}{I_i^0} = (1 + \chi) - \left[\frac{1}{3\pi} \text{erfc}(\sqrt{\chi_p}) \exp(\chi_p) + \frac{2}{3} \frac{\sqrt{\chi_p}}{\pi^{3/2}} \right] \beta + O(\beta^2) \quad (\text{I.78})$$

$$\frac{I_i^{Low}}{I_i^0} = 1 - \frac{\sqrt{\pi}}{2} \sqrt{\chi_p} \text{erfc}(\sqrt{\chi_p}) \exp(\chi_p) + O(\beta^2) \quad (\text{I.79})$$

The Lower bound is approached in the limit $r_L \ll L_\phi$, where L_ϕ is the characteristic length scale of the potential variation. That is to say when β and λ_{De}/r_p are large. The Helical upper bound is approached in the opposite limit, when β and λ_{De}/r_p are small.

For high enough potentials, I_i^{Up} is higher than $I_i^{\text{Canonical}}$ (Section I.4.3). The optimum upper bound is therefore $\min(I_i^{Up}, I_i^{\text{Canonical}})$. For all practical purposes, we can use the respective expansions given by Eqs (I.43, I.78).

Extending this theory to flowing plasmas does not appear feasible, because it is not possible to find an analytic expression for f_i^{3D} in this case.

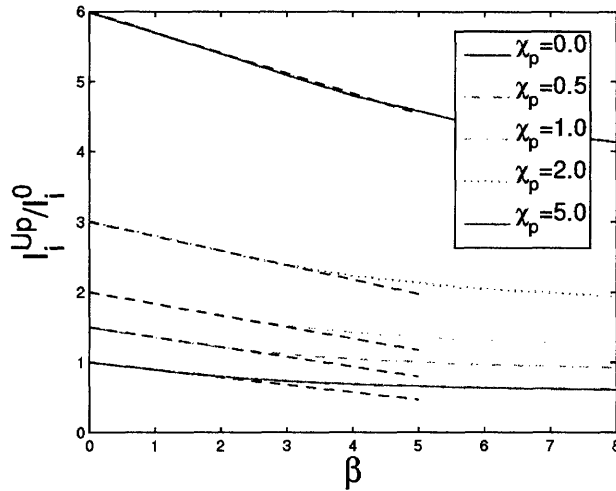


Figure I-8: Upper bound ion current collected by a stationary spherical probe (normalized to $I_i^0 = 4\pi r_p^2 n_\infty \frac{v_{ti}}{2\sqrt{\pi}}$) as a function of the magnetic field for different ion-energy normalized probe potentials. We verify that the current at $\beta \ll 1$ follows the analytical expression given by Eq. (I.78).

I.5.5 Quasicollisionless collection in a strongly magnetized plasma

The model distribution function that we used to verify the Bohm criterion is only qualitatively reasonable in the collisionless presheath. Indeed it assumes that the ions only have a velocity directed towards the probe, while their distribution should tend to a full Maxwellian at infinity. What is more the presheath has been assumed to be one-dimensional, which is usually not the case.

In the presence of a strong magnetic field however, the presheath will indeed be one-dimensional, and it is then possible to find the ion distribution function within it more accurately. A model derived by Chung and Hutchinson [7] assumes that the non conservation of ion momentum in the “quasi-collisionless” presheath is due to cross field transport of ions between the magnetic shadow of the probe and the external plasma. If we define by l the ion mean free path along the field lines and L the length of the magnetic presheath, this model assumes $l \gg L$ (which is the meaning of “quasi-collisionless” [4]), valid when anomalous transport dominates.

In steady state, the one-dimensional Vlasov equation in the presheath can then

be written:

$$v_z \frac{\partial f_i}{\partial z} - \frac{Ze \partial V}{m_i} \frac{\partial f_i}{\partial z \partial v_z} = W [f_i^\infty(v_z) - f_i(z, v_z)] \quad (\text{I.80})$$

where $W \sim D_\perp/r_p^2$, D_\perp being the anomalous cross-field diffusion coefficient.

This equation can be solved numerically along with Poisson's equation with a very small Debye length or directly by assuming quasineutrality. In both cases the boundary conditions are $f_i(z = \infty) = f_i^\infty$ and $f_i(z = 0, v_z > 0) = 0$. The length of the magnetic presheath in this model is then given by [4]:

$$L \simeq \frac{r_p^2}{D_\perp} \sqrt{\frac{T_e}{m_i}} \quad (\text{I.81})$$

Fig. (4) from Ref. [7] gives an example of the ion distribution evolution in the presheath as a function of ϕ taken as an abscissa parameterization. Fig. (II-7) shows this distribution at $\phi = -0.57$ for $T_i = ZT_e$

If the opposite limit is taken ($l \ll L$, valid in the absence of anomalous transport when $r_L \ll r_p$) and we are mainly concerned with charge-exchange collisions, the distribution function is simply a stationary Maxwellian (the background atom distribution) with density $n_i = n_\infty/Z \exp(\phi)$ (quasineutrality condition).

Fig. (I-9) shows those distributions, as well as f_i^∞ , f_i^{1D} and f_i^{3D} for $T_i = ZT_e$, $v_d = 0$ and $\phi = -0.57$.

If the ion distribution at infinity is taken to be a drifting Maxwellian, it is possible to relate the flux density upstream Γ_i^U to the flux downstream Γ_i^D under the form

$$R = \frac{\Gamma_i^U}{\Gamma_i^D} = \exp(Kv_d) \quad (\text{I.82})$$

The coefficient K is called the mach-probe calibration factor, and is to a good approximation independent of v_d . For $T_i = ZT_e$, $K \simeq 1.7$ [7].

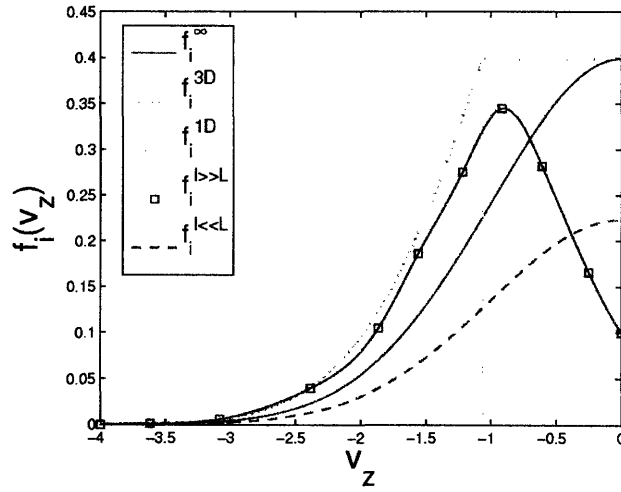


Figure I-9: Different models of ion distribution function in the presheath with $T_i = ZT_e$ and $v_d = 0$, at $\phi = -0.57$. f_i^∞ is the distribution function at infinity, f_i^{3D} and f_i^{1D} assume the ion acceleration in the presheath is purely three-dimensional or adiabatic (Eqs (I.60,I.61)). $f_i^{l \gg L}$ and $f_i^{l \ll L}$ take collisions into account, in the regime where anomalous transport dominates or is negligible. $f_i^{l \gg L}$ is from Fig. (4) from Ref. [7].

Chapter II

Solving the problem with the PIC code SCEPTIC

II.1 SCEPTIC Overview

II.1.1 The unit system

For convenience, the equations have been non-dimensionalized as follows. Each physical quantity can be expressed by its non-dimensional value (A real number \bar{Q}) multiplied by an appropriate product of powers of fundamental units.

Physical quantity	Unit	Value
Mass	$M = \frac{m_i}{Z}$	Ion mass to charge ratio
Charge	e	Elementary charge
Distance	r_p	Probe radius
Energy	T_e	Electron temperature

Table II.1: Set of fundamental units used with SCEPTIC.

For example the electron mass m_e can be written as $m_e = 9.11 \cdot 10^{-31} \text{kg} = \bar{m}_e M$. If the ion species is O^{2+} , then $\frac{m_i}{Z} = 1.34 \cdot 10^{-26} \text{kg}$ and $\bar{m}_e = 6.80 \cdot 10^{-5}$.

For the dependent units several possibilities exist, and our choice is given in Table (II.2). For example the Ion thermal velocity is $v_{ti} = \sqrt{\frac{2T_i}{m_i}} = \bar{v}_{ti} \sqrt{\frac{T_e}{M}}$, with

$\bar{v}_{ti} = \sqrt{2\bar{T}_i}$. Densities are in units of n_∞ (The electron density at infinity).

Physical quantity	Symbol	Unit
Time	\bar{t}	$r_p \sqrt{M/T_e}$
Magnetic field	\bar{B}_z	$\sqrt{MT_e}/er_p$
Ion temperature	\bar{T}_i	ZT_e
Ion density	\bar{n}_i	n_∞/Z
Potential	$\bar{\phi}$	T_e/e
Potential	$\bar{\chi}$	$-T_i/Ze$
Drift velocity	\bar{v}_d	$\sqrt{T_e/M}$
Ion charge flux-density	$\bar{\Gamma}_i$	$n_\infty v_{ti}/2\sqrt{\pi}$

Table II.2: Dependent units in SCEPTIC.

The unit for the particle flux given in Table (II.2) is lower by a factor $\sqrt{\frac{\bar{T}_i}{2\pi}}$ from the corresponding unit used in Refs [2, 3].

II.1.2 The equations

Newton's equation for the ions

We solve the equation of motion for each ion:

$$\frac{m_i}{Z} \frac{d\mathbf{v}}{dt} = e [-\nabla\phi + \mathbf{v} \wedge \mathbf{B}] \quad (\text{II.1})$$

$$M \frac{d\bar{\mathbf{v}}}{d\bar{t}} \frac{\sqrt{\frac{T_e}{M}}}{r_p \sqrt{\frac{M}{T_e}}} = e \left[-\bar{\nabla}\bar{\phi} \frac{T_e}{r_p} + \bar{\mathbf{v}} \wedge \bar{\mathbf{B}} \sqrt{\frac{T_e}{M}} \frac{\sqrt{MT_e}}{er_p} \right] \quad (\text{II.2})$$

$$\frac{d\bar{\mathbf{v}}}{d\bar{t}} = [-\bar{\nabla}\bar{\phi} + \bar{\mathbf{v}} \wedge \bar{\mathbf{B}}] \quad (\text{II.3})$$

Poisson's equation

We solve Poisson's equation for the potential distribution, by assuming that the electrons are Boltzmann distributed (See Section (I.4.1)).

$$\nabla^2 V = \frac{e}{\epsilon_0} [n_e - Zn_i] \quad (\text{II.4})$$

$$\bar{\nabla}^2 \bar{\phi} \frac{T_e}{r_p^2} = \frac{e}{\epsilon_0} [\bar{n}_e - \bar{n}_i] n_\infty \quad (\text{II.5})$$

$$\bar{\nabla}^2 \bar{\phi} = \frac{1}{\bar{\lambda}_{De}} [\bar{n}_e - \bar{n}_i] \quad (\text{II.6})$$

with

$$\bar{n}_e = \exp(\phi) \quad (\text{II.7})$$

Quasineutrality equation

In the quasineutral case, Poisson's equation becomes:

$$\phi = \ln(\bar{n}_i) \quad (\text{II.8})$$

II.1.3 The Geometry

While the ions are three-dimensionally advanced in cartesian coordinates, the potential is defined on a two-dimensional spherical mesh centered on the probe. The cell centers are equally spaced in r (Δr) and $\cos \theta$ ($\Delta \cos \theta$), with the exception of the first and last angular slice where the angular separation is $\frac{1}{2} \Delta \cos \theta$. This is shown in Fig. (II-1).

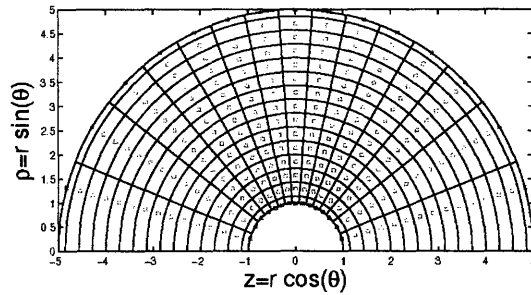


Figure II-1: Spherical mesh used in SCEPTIC. Black lines define the cell boundaries, while red squares are the cell centers.

Each physical quantity, defined at the cell centers, must be understood as a cell-averaged value.

II.2 Development of a parallelized Poisson solver

II.2.1 Successive Over Relaxation

Each cell center is labeled by (i, j) , respectively the radial and angular position. Poisson's equation can then discretized as follows:

$$\begin{aligned}\lambda_{De}^2 \nabla^2 \phi_{i,j} &= a_{i,j} \phi_{i+1,j} + b_{i,j} \phi_{i-1,j} + c_{i,j} \phi_{i,j+1} + d_{i,j} \phi_{i,j-1} - f_{i,j} \phi_{i,j} \\ &= \text{Source} = -\bar{n}_{i,j} + e^{\phi_{i,j}}\end{aligned}\quad (\text{II.9})$$

where the coefficients a,b, ... are chosen in order to make the discretization consistent with the original differential equation.

The standard Successive Over Relaxation (SOR) principle is to update the potential at each cell center using the following formula (ϕ is the old value):

$$\phi^{new} = \omega \phi^* + (1 - \omega) \phi = \phi + \omega(\phi^* - \phi) \quad (\text{II.10})$$

where $\phi_{i,j}^*$ is defined by:

$$a_{i,j} \phi_{i+1,j} + b_{i,j} \phi_{i-1,j} + c_{i,j} \phi_{i,j+1} + d_{i,j} \phi_{i,j-1} - f_{i,j} \phi_{i,j}^* = \text{Source} \quad (\text{II.11})$$

We have the choice between an explicit scheme: $\text{Source} = -\bar{n}_{i,j} + e^{\phi_{i,j}}$ and a semi-implicit scheme: $\text{Source} = -\bar{n}_{i,j} + e^{\phi_{i,j}^*}$. In the first case we get:

$$\phi_{i,j}^* - \phi_{i,j} = \frac{a_{i,j} \phi_{i+1,j} + b_{i,j} \phi_{i-1,j} + c_{i,j} \phi_{i,j+1} + d_{i,j} \phi_{i,j-1} - f_{i,j} \phi_{i,j} + \bar{n}_{i,j} - e^{\phi_{i,j}}}{f_{i,j}} \quad (\text{II.12})$$

and in the second, if we assume $e^{\phi_{i,j}^*} \sim e^{\phi_{i,j}} [1 + (\phi_{i,j}^* - \phi_{i,j})]$:

$$\phi_{i,j}^* - \phi_{i,j} = \frac{a_{i,j} \phi_{i+1,j} + b_{i,j} \phi_{i-1,j} + c_{i,j} \phi_{i,j+1} + d_{i,j} \phi_{i,j-1} - f_{i,j} \phi_{i,j} + \bar{n}_{i,j} - e^{\phi_{i,j}}}{f_{i,j} + e^{\phi_{i,j}}} \quad (\text{II.13})$$

While both discretizations of the source lead to the same result, it is experimentally

found that the semi-implicit version (Eq. (II.13)) converges faster.

The serial code is straightforward. We alternatively upgrade the odd points (This step only requires the potential on the even cells), and the even points (This step only requires the potential on the odd cells), and iterate until the residual $R = \max_{i,j}(\phi_{i,j}^* - \phi_{i,j})$ is smaller than a given limit.

II.2.2 Parallel code structure

Because in the magnetized case strong potential gradients are expected in the magnetic shadow, a high angular resolution is required, typically between 150 and 250 angular cells. In addition, the radial extension of the computational domain must exceed two average Larmor radii, therefore at low β the required number of radial cells is high and can reach values of 200 or more. Under those conditions solving Poisson's equation with the serial code takes approximately half of the total computational time, which is not acceptable. I therefore parallelized the solver using the MPI protocol, starting from a general cartesian n-dimensional block-solver written by Hutchinson.

The principle of a Parallel SOR solver is to subdivide the original grid in several sub-grids on a cartesian topology, and separate the jobs among the processors as shown in Fig. (II.2.2).

II.2.3 Performance expectation

We define n_r and n_θ to be the number of radial and angular cells, and P_r and P_θ the radial and angular size of the processor grid. Therefore $n = n_r n_\theta$ is the total number of cells, and $P = P_r P_\theta$ the total number of processors. An estimation of the iteration time required to reach convergence is:

$$\tau = \frac{K_1}{P_r P_\theta} + \varepsilon_r (K_2 + K_3 \frac{n_\theta}{P_\theta}) + \varepsilon_\theta (K_2 + K_3 \frac{n_r}{P_r}) + K_4 P_r P_\theta \quad (\text{II.14})$$

The term $\frac{K_1}{P_r P_\theta}$ shows that the calculation speed is inversely proportional to the number of processors. $\varepsilon_{r,\theta}$ is 0 or 1 depending on whether the corresponding dimension

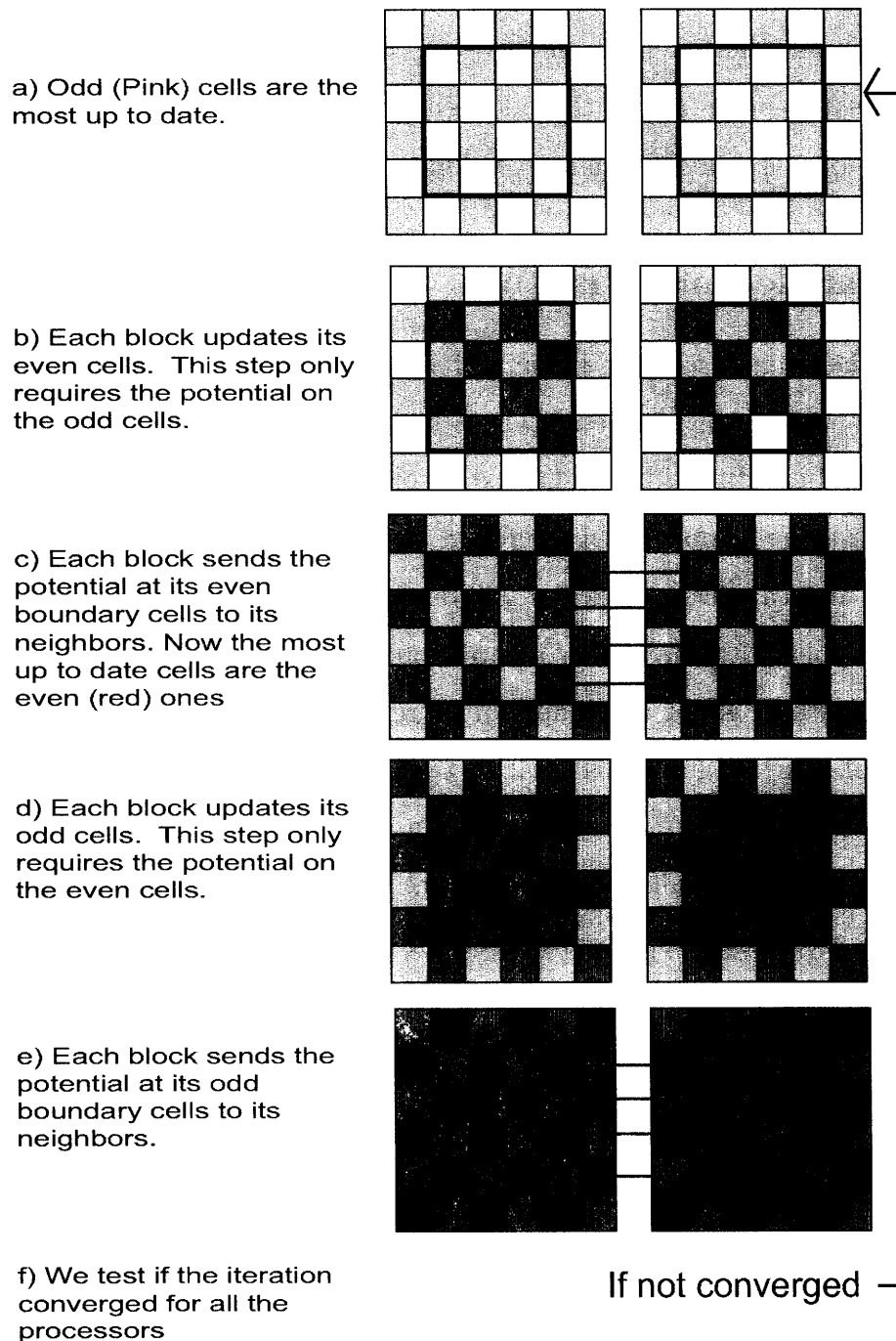


Figure II-2: Principle of the block-solver, where we can see two processors working. The black squares delimitate the cells whose potential is calculated by the corresponding processor, while the one-cell wide crown is made of values computed by the neighboring processors.

has 1 or several processors. $\frac{n_r}{P_r}$ and $\frac{n_\theta}{P_\theta}$ is proportional to the amount of data that two neighboring processors must send to each other at each iteration. $(K_2 + K_3 \frac{n_\theta}{P_\theta})$ and $(K_2 + K_3 \frac{n_r}{P_r})$ are therefore simple estimates of the communication cost. The term $K_4 P_r P_\theta$ arises from the need, at the end of each iteration step, for each slave processor to communicate to the master node for the convergence test.

By inverting τ , we get the following speed-up scale:

$$\frac{1}{\tau} \propto \frac{P}{1 + \alpha_1 \sqrt{P} + \alpha_2 P^2} \quad (\text{II.15})$$

We therefore expect the performance to rise linearly with the number of processors, reach a plateau, and then decrease as the inverse of this number.

II.2.4 Optimization

To get better performance, it is possible to lower τ by means of some trade-off on the K factors. We can reduce K_4 by calling the converging test (step (f) on Fig. (II.2.2)) only every 30 iterations. By doing so K_1 increases slightly because we can superfluously iterate up to 29 times. It is also possible to reduce K_2 and K_3 by subcycling the iteration in each processor. For example we only do alternatively (c) and (e). We therefore save 3 times the cost of boundary values communications. By doing so K_1 slightly increases as well because we need more steps to reach the desired convergence. The optimum parameters (30 and 3) have been found by experimental investigation.

II.2.5 Test

For the purpose of the test we implemented the two optimizations described in the preceding paragraph, although in practice only the first one is used (Calling the convergence test once every 30 iterations).

We performed a test on a $(n_r = 200) \times (n_\theta = 200)$ grid with $\phi_p = -4$ and $\phi(r_b) = 20$ (r_b is the radius of the outer boundary). The ion density is assumed to be uniform and equal to 1, and we start with an initial Coulomb guess, i.e. $\phi \propto 1/r$. Fig. (II-3) shows the performance measured as the inverse of the iteration time,

normalized to the single-processor performance.

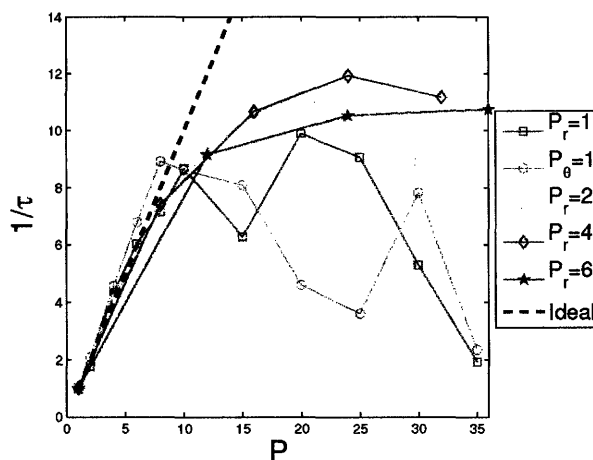


Figure II-3: Bloc solver performance as a function of the processor-grid topology.

The qualitative behavior of the solver follows our expectations: the speed-up is ideal for a low number of processors, and deteriorates as P rises. Because we use the MPI protocol as a black box, we can not quantitatively explain the complicated behavior of the $P_r = 1$ and $P_\theta = 1$ curves. However it is clear that the best performance is obtained for square grids (i.e. $P_r \sim P_\theta$) since those minimize the ratio of surface over volume of the solver blocks. When using SCEPTIC with a non square mesh and have access to P nodes, we therefore set P_r and P_θ such as to minimize this ratio:

$$\begin{aligned}
 P_r &= \text{int}\left(\sqrt{P \frac{n_r}{n_\theta}}\right) \\
 P_\theta &= \text{int}\left(\frac{P}{P_r}\right)
 \end{aligned}
 \tag{II.16}$$

II.3 Development of a symplectic magnetized particle mover

II.3.1 Motivation

The Boris integration scheme [17, 19], designed to integrate a single particle orbit in an electromagnetic field, is widely used in explicit Particle in Cell simulations of plasmas. The reasons for this popularity are twofold. One of them is that it is extremely simple to implement, and offers second order accuracy while requiring only one field evaluation per step. The second reason, maybe even more important, is that it is found that the error on conserved quantities such as the energy, or the canonical angular momentum when the system is axisymmetric, is bounded for an infinite time (The error on those quantities being second order as the scheme).

Those conservation properties are characteristic of symplectic schemes, which are a class of geometric integrators. If the vector $(\mathbf{q}, \mathbf{p})(t)$ is the solution of a symplectic integrator's difference equation, then there exists a Hamiltonian \tilde{H} such as:

$$\frac{d\mathbf{p}}{dt} = -\nabla_{\mathbf{q}}\tilde{H} \quad \frac{d\mathbf{q}}{dt} = \nabla_{\mathbf{p}}\tilde{H} \quad (\text{II.17})$$

This means the symplectic two-form $d\mathbf{p} \wedge d\mathbf{q}$ is conserved, hence the terminology. Because of such properties it has been speculated [20] that the Boris scheme is symplectic. To our knowledge however, this has not previously been proved.

We present here a new second order integrator for the specific case where the magnetic field is time-independent and uniform, symplectic by construction, and based on an extension of the *Kick* and *Drift* concepts of the standard *Leap-frog* algorithm in absence of a magnetic field. For the purpose of this thesis, integrating the ion orbits with a symplectic scheme is not essential since an ion operates at most a few revolutions around the probe before being collected or leaving the domain. We nevertheless use this new integrator because it is shown (See Section II.3.4) to perform better than Boris scheme.

This integrator, called “cyclotronic”, has been developed during my stay at Los

Alamos National Laboratory during the summer 2006, and has first been implemented in the Particle in Cell code *Democritus* [22].

II.3.2 Single particle Hamiltonian

The single particle motion Hamiltonian in the presence of a magnetic field $\mathbf{B} = \nabla \times \mathbf{A}$ can be written as:

$$H = \frac{(p_z - ZeA_z)^2}{2m} + \frac{(p_x - ZeA_x)^2}{2m} + \frac{(p_y - ZeA_y)^2}{2m} + ZeV(q_x, q_y, q_z) \quad (\text{II.18})$$

The equation of motion (Eq. (II.1)) becomes:

$$\begin{cases} \frac{d\mathbf{p}}{dt} = -\nabla_{\mathbf{q}}H \\ \frac{d\mathbf{q}}{dt} = \nabla_{\mathbf{p}}H \end{cases}$$

with $\mathbf{q} = \mathbf{x}$ and $\mathbf{p} = m\mathbf{v} + Ze\mathbf{A}$.

A property of Hamiltonian flows is that there exists a Liouville operator D_H such that:

$$\frac{dz}{dt} = \{z, H(z)\} = D_H z \quad \text{i.e.} \quad \forall \tau \in \mathbf{R} \quad z(\tau) = e^{\tau D_H} z(0) \quad (\text{II.19})$$

where $\{.,.\}$ stands for the Poisson bracket and $z = (\mathbf{p}, \mathbf{q})$. For an introduction to symplectic integrators avoiding unnecessary mathematical formalism, see Ref. [24].

A more complete treatment of Hamiltonian flows can be found in Ref. [25].

In the case of a static uniform magnetic field [$\mathbf{B} = B\mathbf{z}$ and $A_x^2 + A_y^2 = \frac{1}{4}B^2(q_x^2 + q_y^2)$], the Hamiltonian can be separated in two exactly integrable parts as follows:

$$\begin{aligned} T(p, q) &= \frac{p_z^2}{2m} + \frac{(p_x - eA_x)^2}{2m} + \frac{(p_y - eA_y)^2}{2m} \\ V(q) &= ZeV(q) \end{aligned} \quad (\text{II.20})$$

Indeed the operators $D_T(\Delta t)$ and $D_V(\Delta t)$ associated with the Hamiltonians T and

V can be written explicitly:

$$D_T(\Delta t) := \begin{cases} p_z(t) & \mapsto p'_z = p_z(t) \\ p_\perp(t) & \mapsto p'_\perp = \overline{\overline{R}}_{0,\Omega\Delta t}(p_\perp(t)) \\ q_z(t) & \mapsto q'_z = q_z(t) + \frac{p_z(t)}{m}\Delta t \\ q_\perp(t) & \mapsto q'_\perp = \overline{\overline{R}}_{C(t),\Omega\Delta t}(q_\perp(t) - C(t)) \end{cases} \quad (\text{II.21})$$

$$D_V(\Delta t) := p(t) \mapsto p' = p(t) - \Delta t \frac{\partial V}{\partial q} \quad (\text{II.22})$$

Where C is the center of the Larmor circle, and $\overline{\overline{R}}_{C,\alpha}$ is a rotation of center C and characteristic vector α .

D_T can be seen as a *Drift* operator, describing an homogeneous helicoidal trajectory, while D_V is the standard *Kick*, describing the acceleration due to the electric field.

It can be shown, using the Baker-Campbell-Hausdorff (BCH) formula, that

$$e^{\Delta t D_H} = e^{(\Delta t/2)D_V} \cdot e^{\Delta t D_T} \cdot e^{(\Delta t/2)D_V} + O(\Delta t^3) \quad (\text{II.23})$$

A second order symplectic integrator for H , first derived by Verlet [21] but usually called *Leap-frog* algorithm is therefore:

$$D_{\bar{H}}(\Delta t) = D_V(\Delta t/2)D_T(\Delta t)D_V(\Delta t/2) \quad (\text{II.24})$$

For the purpose of PIC codes, it is possible to group the D_V together and define the velocity and position with half a time step of offset. Since the *Drift* corresponds to a cyclotronic motion in absence of electric field, we will refer to this new integrator as cyclotronic.

II.3.3 Practical implementation

A practical implementation in cartesian coordinates of the cyclotronic integrator is:

1. *Kick*:

$$\mathbf{v}' - \mathbf{v} = -Ze\nabla V(\mathbf{x})\Delta t \quad (\text{II.25})$$

2. *Drift*

$$\begin{cases} z' - z = v'_z \Delta t \\ x' - x = \frac{v'_y - v'_y \cos(\Omega\Delta t) + v'_x \sin(\Omega\Delta t)}{\Omega} \\ y' - y = \frac{-v'_x + v'_x \cos(\Omega\Delta t) + v'_y \sin(\Omega\Delta t)}{\Omega} \\ v''_x = v'_x \cos(\Omega\Delta t) + v'_y \sin(\Omega\Delta t) \\ v''_y = v'_y \cos(\Omega\Delta t) - v'_x \sin(\Omega\Delta t) \end{cases} \quad (\text{II.26})$$

where \mathbf{v} and \mathbf{x} are offset by half a time-step.

In the absence of electric field, the present integrator is exact regardless of the time-step. Because the potential gradient is expected to be higher at the probe edge than in the rest of the computational domain, we implemented a subcycling scheme, according to which each particle is advanced with a time-step inversely proportional to its distance to the probe. This procedure is illustrated in Fig. (II-4).

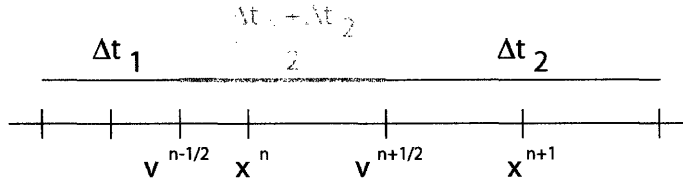


Figure II-4: For each ion, position and velocity are offset by half a time-step. When subcycling is enabled, the change in time-step occurs in the velocity advance portion.

It must be acknowledged that in the general case, a symplectic integrator loses its conservation properties when used with a variable time step [23].

II.3.4 Benchmarking against direct orbit integration

Fig. (II-5) compares the total ion current to the probe as a function of the time-step, for different orbit integrators. For this test case, the electron Debye length is assumed to be infinite in order for the potential to be Coulomb.

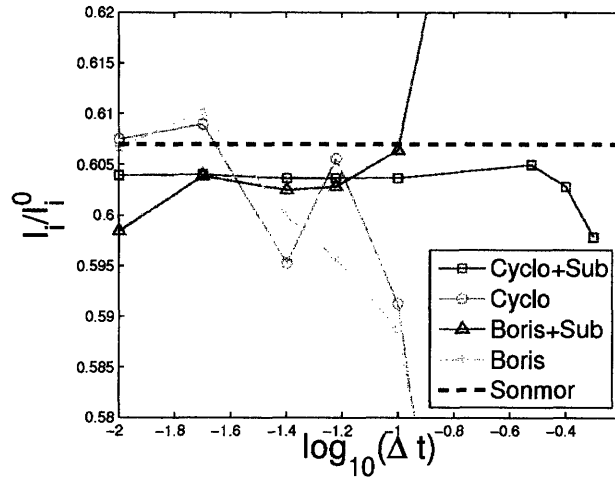


Figure II-5: Total ion current to a spherical probe as a function of the particle mover time-step for different movers. The probe bias is $\chi_p = 4$, the potential distribution is assumed to be Coulomb, and the background magnetic field has magnitude $\beta = 7$. The computational domain has an extension $r_b = 16r_p$. The dashed line corresponds to the result of Sonmor and Laframboise [12].

It can easily be seen that the Cyclotronic mover, when coupled with subcycling, allows to calculate a current essentially independent on the time-step for $\Delta \bar{t} \lesssim 0.2$. Because the extension of the computational domain is $r_b = 16r_p$, an ion in the immediate vicinity of the probe is advanced with a time-step $\Delta \bar{t}/16$. The computed value of the current is $I_i = 0.604I_i^0$, in agreement with the value computed by Sonmor and Laframboise ($I_i = 0.607I_i^0$) within the 1% accuracy claimed in their publication [12].

II.4 The boundary conditions

II.4.1 Conditions on the potential

Inner boundary

If the electron Debye length λ_{De} is finite, we impose the potential at $r = r_p$ to be the probe potential ϕ_p .

If $\lambda_{De} = 0$ however, ϕ_p (provided it is negative enough) is irrelevant because an infinitesimally thin Debye sheath forms at the probe surface, at the entrance of which the Bohm criterion must be satisfied. At each iteration we self-consistently compute the ratio of specific heats in the radial direction for each angular cell at the probe edge (Eq. (I.8)), and deduce the radial sound speed distribution there. An effective probe potential is then calculated for each angular cell in order for the ions to be accelerated to the sound speed.

Outer boundary

As emphasized in the first chapter, the problem shows two scale lengths. A collisionless sheath and presheath, extending a few r_p from the probe, followed by an elongated collisional or “quasi-collisionless” presheath extending a few mean free paths along the magnetic axis. This situation is illustrated in Fig. (II-6)

Our purpose is, using SCEPTIC, to simulate the collisionless presheath. If the electron Debye length is negligible, the potential is straightforwardly given by applying the quasineutrality equation (Eq. (II.8)). When λ_{De} is finite however, conditions on the potential are needed at the outer boundary of the computational domain in order to solve Poisson’s equation, and it would be incorrect to impose $\phi = 0$ there. Indeed however large r_b is, cross field transport is required for the magnetic shadow of the probe to merge in the unperturbed plasma. Because far from the probe the potential gradient in the radial direction is negligible, the problem adopts the symmetry of the magnetic field: cylindrical. With the scale length of the quasi-collisionless presheath being much longer than the collisionless presheath, we can write:

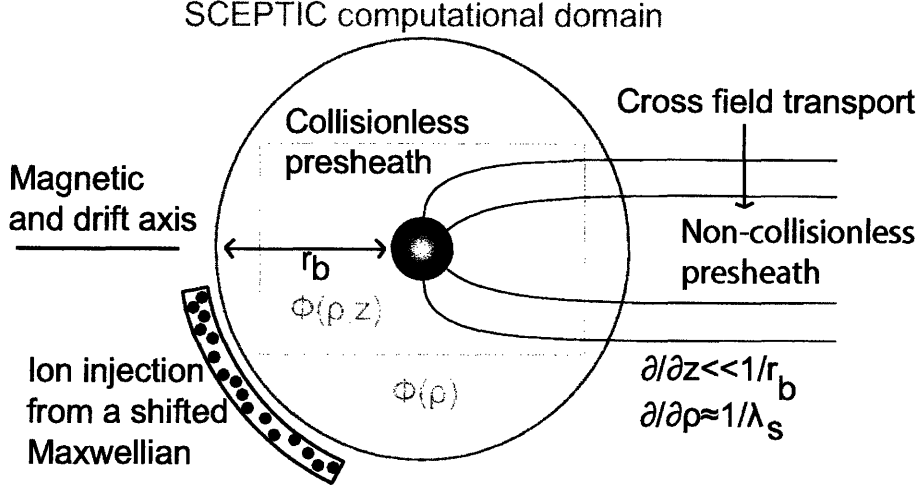


Figure II-6: Schematic view of the problem. SCEPTIC simulates the collisionless presheath, assumed to have an extension r_b . The quasi-collisionless presheath has an extension L , controlled by cross-field transport or collisions, and is not simulated in the present work. On the collisionless scale length, $\partial/\partial z = 0$ at the outer boundary of the computational domain. Indeed a few probe radii away from the probe surface, the problem adopts the cylindrical symmetry of the magnetic field.

$$\frac{\partial}{\partial z} = 0 \quad \text{at} \quad r = r_b \quad (\text{II.27})$$

On axis this can readily be translated in a boundary condition on the potential:

$$\frac{\partial \phi}{\partial r} \Big|_{\text{Axis}} = \frac{\tan \theta}{r} \frac{\partial \phi}{\partial \theta} \quad (\text{II.28})$$

Because Eq. (II.28) is ill conditioned at $\cos \theta \sim 0$ ($\infty \cdot 0$), $\frac{\partial \phi}{\partial \rho}$ is needed as well in this region. Let us assume that $Zn_i = 1$ there. This choice can be motivated as follows. The ion density outside the computational domain is dictated by unknown collisional dynamics, but can not exceed the Boltzmann factor: $Zn_i \leq \exp(-Z\phi T_e/T_i) \sim 1 - Z\phi T_e/T_i$. What is more, in order for the potential to monotonically decay to 0, collisions act such as to impose $Zn_i \geq n_e$. Therefore $1 - Z\phi T_e/T_i \geq Zn_i \geq n_e \sim 1 + \phi$. Choosing $Zn_i = 1$ appears as an appropriate average of the two limits. The potential therefore obeys the following equation far from the magnetic shadow:

$$\frac{1}{\rho} \frac{\partial}{\partial \rho} \left(\rho \frac{\partial \phi}{\partial \rho} \right) - \frac{\phi}{\lambda_{De}^2} = 0 \quad (\text{II.29})$$

The decaying solution to this equation is $\phi(\rho) \propto K_0(\frac{\rho}{\lambda_{De}}) \sim \frac{1}{\sqrt{\rho}} \exp(-\frac{\rho}{\lambda_{De}})$. The appropriate boundary condition far from the magnetic axis is therefore $\frac{\partial \phi}{\partial \rho} = -\phi(\frac{1}{\lambda_{De}} + \frac{1}{2\rho})$, or in spherical coordinates:

$$\frac{\partial \phi}{\partial r}|_{\text{Top}} = -\phi \left(\frac{1}{2r} + \frac{\sin \theta}{\lambda_{De}} \right) \quad (\text{II.30})$$

The two boundary conditions given by Eq. (II.28,II.30), both implying that $\frac{\partial \phi}{\partial z} = 0$, can be associated by linear combination in a single equation valid for $\cos \theta \in [-1; 1]$:

$$\frac{\partial \phi}{\partial r} = \cos^2 \theta \frac{\partial \phi}{\partial r}|_{\text{Axis}} + \sin^2 \theta \frac{\partial \phi}{\partial r}|_{\text{Top}} = \frac{\sin \theta \cos \theta}{r} \frac{\partial \phi}{\partial \theta} - \phi \left(\frac{\sin^2 \theta}{2r} + \frac{\sin^3 \theta}{\lambda_{De}} \right) \quad (\text{II.31})$$

Eq. (II.31) is the outer boundary condition on the potential that we use when $\lambda_{De} \neq 0$.

II.4.2 Particle reinjection

Neither Eq. (I.60) or Eq. (I.61) are immediately appropriate expressions for the inward ($v_r < 0$) ion distribution at $r = r_b$ because they do not account for momentum exchange that the ions experienced in the non-collisionless presheath. Fig. (II-7) shows the one-dimensional flux-density distributions corresponding to the distribution functions shown in Fig. (I-9) at $\phi = -0.57$ for $\bar{T}_i = 1.0$. If we simulate a configuration in which the transition between the collisionless and collisional presheaths is at a potential $\phi_t \simeq -0.6$, the type of collisionality has a strong influence on the appropriate reinjection.

$|\phi_t|$ is an increasing function of β . Indeed if $\beta = 0$ a fully collisionless treatment is possible and $\phi_t = 0$. We therefore expect $f_{i \ll L}$ and $f_{i \gg L}$ to approach f_i^∞ when $\beta \rightarrow 0$. In the opposite limit of $\beta \gg 1$, the quasi-collisionless presheath extends up to the sheath edge and $\phi_t = \phi_s$.

If we were to reinject the ions with one of the distribution functions shown in

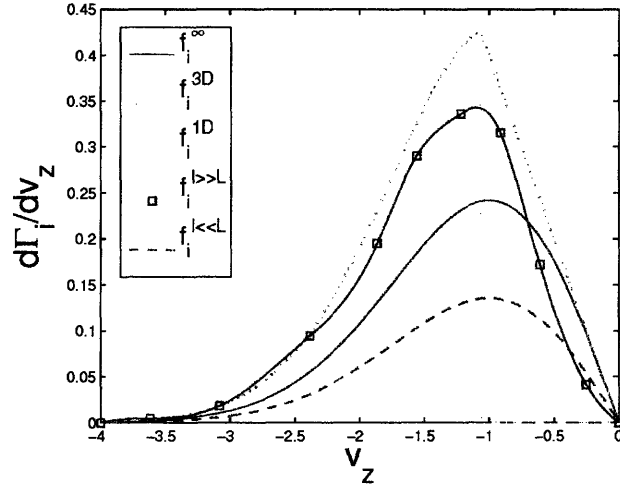


Figure II-7: Differential flux ($d\Gamma_i^\infty/dv_z = -v_z f_i(v_z)$) of incoming ions at the transition between the collisional and collisionless presheaths for $\phi_t = -0.57$ and $\bar{T}_i = 1$ for the models already discussed in Fig. (I-9).

Fig. (I-9), the differential flux distributions shown in Fig. (II-7) would govern the number of ions having a given v_z that would be reinjected at each time step, $d\Gamma_i^\infty/dv_z$ is to a good approximation the average of $d\Gamma_i^{l \ll L}/dv_z$ and $d\Gamma_i^{l \gg L}/dv_z$. f_∞ appears therefore to be a reasonable reinjection distribution for a situation where $l \simeq L$, which for weakly magnetized plasma is precisely the case of classical transport [4].

Physically plausible results when collisionality is low can therefore be obtained by using a computational domain large enough to resolve the whole collisionless presheath, and by reinjecting the ions at the boundary with their *distribution function at infinity* regardless of the potential distribution at the boundary. This is the approximation we use.

Chapter III

Solutions for a stationary plasma

III.1 Weakly-focusing and Strongly-focusing regimes

The Canonical upper bound (Eq. (I.43)), Helical upper bound (Eq.(I.78)), and Adiabatic lower bound (Eq.(I.79)) depend on β and on the ion-energy normalized probe potential χ_p . In the limit of infinite Debye length, the exact ion current only depends on those two quantities as well [12]. \bar{T}_i does not enter into these preceding expressions because none of them depends on the electron dynamics (Recall that $\bar{T}_i = T_i/ZT_e$). This is obviously not the case when $\bar{\lambda}_{De} < \infty$, since $\bar{n}_e = \exp(\phi)$ is required to solve Poisson's equation (Eq. (I.45)) or to use the quasineutrality relationship (Eq. (II.8)). In the limit $\lambda_{De} = 0$, the current becomes independent of the probe potential.

We see that in no regime does the ion current explicitly depend on the electron energy-normalized probe potential ϕ_p . If $\bar{\lambda}_{De} \lesssim 0.1$, the ions see a “virtual” probe potential equal to the sheath-entrance potential: $\phi_s \sim -1$ or $\chi_s \sim ZT_e/T_i$. At higher Debye lengths, the ions see the real probe potential χ_p . We can distinguish between weakly-focusing and strongly-focusing regimes on the basis of the magnitude of the ion energy-normalized potential effectively seen by the ions.

Fig. (III-1) shows some characteristic ion orbits for $\bar{\lambda}_{De} = 1$, $\phi_p = -4$, and $\beta = 1$ at two different temperatures. At $\bar{T}_i = 1$ (Fig. (III-1a)) are plotted orbits of ions with initial velocity $v_z = v_{ti}$ and $v_\rho = \sqrt{\frac{\pi}{2}} \sqrt{\frac{T_i}{m_i}}$, starting with $z = -8r_p$ and various ρ . The choice of transverse velocity corresponds to a gyroradius equal to r_L (Average Larmor

radius). This would be an example of weakly-focusing regime since the ion-energy normalized potential is relatively small ($\chi_p = 4$), and because of the small electron Debye length this potential is strongly shielded. At $\bar{T}_i = 0.1$ (Fig. (III-1b)) are plotted orbits of ions with zero initial velocity, in order to accentuate the difference with the case $\bar{T}_i = 1$. This is an example of strongly focusing regime.

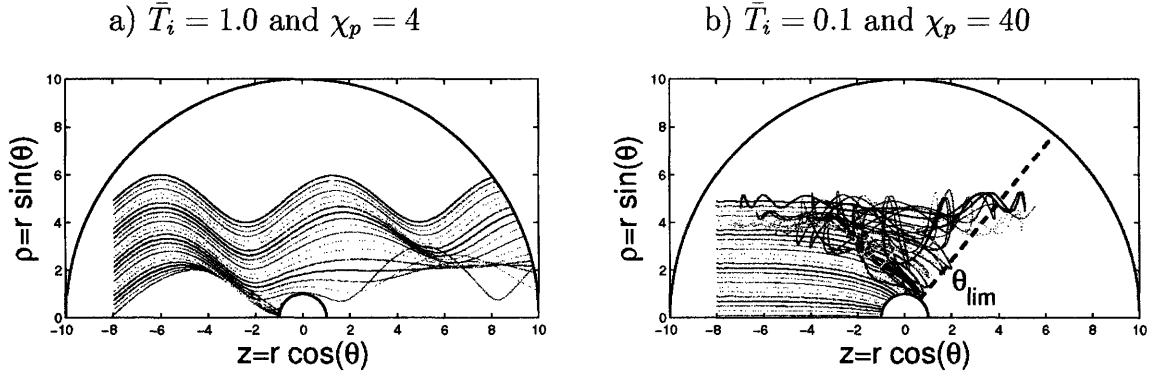


Figure III-1: Characteristic ion orbits for $\bar{\lambda}_{De} = 1$ and $\beta = 1$ in a weakly-focusing and strongly-focusing regime. In order for the orbits to be more visible, SCEPTIC runs have been made with a θ -averaged potential; this does not change the qualitative picture. Obviously because $\bar{v}_d = 0$, the physics is symmetric with respect to $\cos \theta = 0$. On Fig. b, θ_{lim} indicates the depletion cone boundary as given by Eq. (IV.10).

It can be seen that in a weakly-focusing regime the ion collection mainly occurs on axis, and the ion density is quite unperturbed at $r \sim r_p$ and $\cos \theta \sim 0$. On the other hand, in a strongly-focusing regime the ion stream is focused on the probe surface at $\cos \theta \sim 0$. Because the probe electrostatic potential is much higher than the ions' thermal energy, some ions are reflected several times, and space-charge builds up outside the depletion cone delimited by θ_{lim} (Eq. (IV.10)).

III.2 Space-charge distribution

III.2.1 Quasineutral plasma

Because in the limit of zero Debye length the ion density is linked to the potential by the quasineutrality relation (Eq. (II.8)), it is sufficient to study the ion charge-density distribution. Fig. (III-2) shows the axial ($\cos \theta = 1$) and perpendicular ($\cos \theta = 0$)

radial density profiles when the ion temperature at infinity is unity ($\bar{T}_i = 1$), for three different magnetic field strengths.

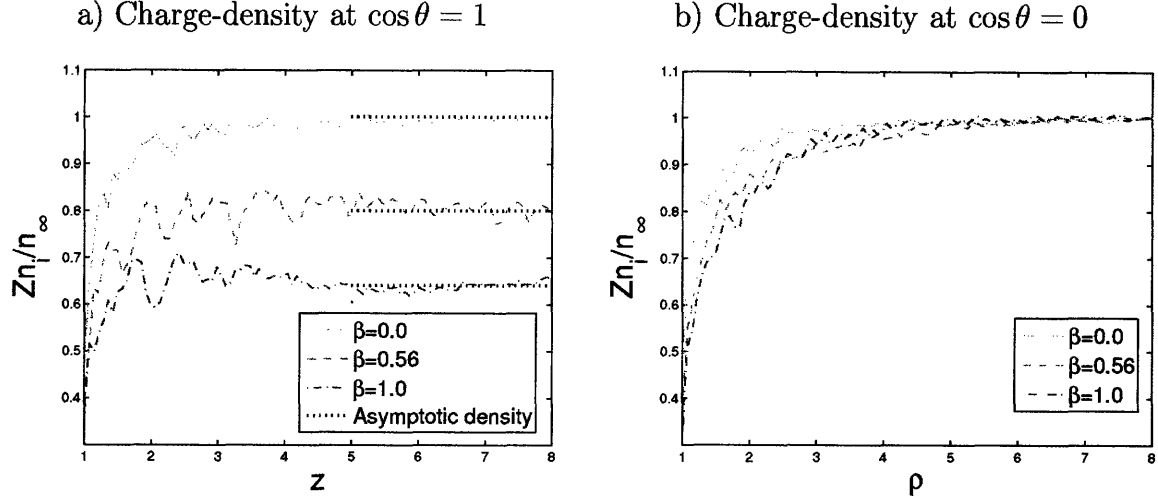


Figure III-2: Axial and Perpendicular charge-density profiles at $\bar{T}_i = 1$ and $\bar{\lambda}_{De} = 0$ for $\beta = 0$, $\beta = 0.56$ and $\beta = 1.0$. On axis (Fig. a), the ion density reaches an asymptote within the computational domain, confirming our hypothesis that $\partial/\partial z = 0$ at the outer boundary (Eq.(II.27)). Fig. b shows that the perpendicular geometrical shielding length λ_\perp grows with β .

The profiles $\cos \theta = 1$ show that the ion density reaches an asymptote within the computational domain, which is consistent with the fact that we are only resolving the collisionless presheath. Intuitively the ion charge-density at the transition collisionless-collisional presheath (Edge of the computational domain) drops as β rises since the ion mobility across the field lines is reduced. Because we reinject an unperturbed Maxwellian regardless of the potential at the boundary, our model would give an ion charge density in the magnetic shadow of $\bar{n}_i = 1/2$ in the limit $\beta = \infty$. In reality, because of cross field transport and collisions in the far presheath the value might be $\bar{n}_i > 1/2$. By restricting ourselves to $\beta \leq 1$ we shall not worry about this issue.

Although we are considering a zero-Debye length situation, it is still possible to qualitatively define a geometrical perpendicular shielding length λ_\perp , measuring the radial potential decay at $\cos \theta = 0$. The profiles show that λ_\perp rises with β . Indeed the higher the magnetic field, the more adiabatically the ions are accelerated in the z direction; therefore the ion density at $r \sim r_p$ and $\cos \theta \sim 0$ is a decreasing function

of β .

It is possible to get a better understanding of the preceding remarks through an analysis of charge-density contour plots. Fig. (III-3) compares the ion space-charge distribution at $\beta = 0.36$ and $\beta = 1.00$ for $\bar{T}_i = 0.3$. In each case, the flux tubes are straight cylinders aligned with the magnetic field. Because we do not solve Poisson's equation this result is not the consequence of an imposed boundary condition. Comparison of the two plots shows that raising the magnetic field opens equipotentials that were closed around the probe. The $\bar{n}_i = 0.95$ line, open in both cases, moves from $\rho \sim 3r_p$ to $\rho \sim 4r_p$, which is consistent with λ_\perp rising with β (Fig. (III-2b)).

Fig. (III-4) compares the ion space-charge distribution at two different temperatures ($\bar{T}_i = 0.1$ and $\bar{T}_i = 1.0$) for $\beta = 1.0$. The perpendicular shielding length λ_\perp is higher at small \bar{T}_i . Indeed typical sheath edge potentials are $\phi_s \sim -1$, independent of \bar{T}_i . However the effective potential drop felt by the ions from infinity to the sheath edge is $\chi = -\phi \frac{ZT_e}{T_i}$. At low \bar{T}_i this potential well is deeper, and since the ions are accelerated preferentially in the z direction their density around the probe is lower, and λ_\perp higher.

III.2.2 Plasma with finite shielding

When the electron Debye length is non negligible, the potential at a given point depends on the whole charge density distribution, and density perturbations are smoothed over a scale-length $\lambda_s \sim \lambda_{De} / \sqrt{1 + ZT_e/T_i}$ (Eq. (I.52)). This can be seen in Fig. (III-5), where axial and perpendicular profiles for $\bar{T}_i = 1$ and $\bar{\lambda}_{De} = 1$ are shown.

On axis (Fig. (III-5a)) and far from the probe, $\phi \sim \ln(\bar{n}_i)$ for $\beta \lesssim 0.3$. Indeed in such a regime the average ion Larmor radius is substantially larger than the probe size, and the magnetic shadow radius. The ion density depletion is therefore transversely spread over several $\bar{\lambda}_{De}$ ($\nabla_\perp n_i \ll 1/\lambda_{De}$). For $\beta \lesssim 0.3$ quasineutrality is satisfied down to $z \sim 4$: this is the sheath entrance.

At $\beta = 1$ ($r_L = r_p$), the density depletion on axis is approximately limited to $2r_p$

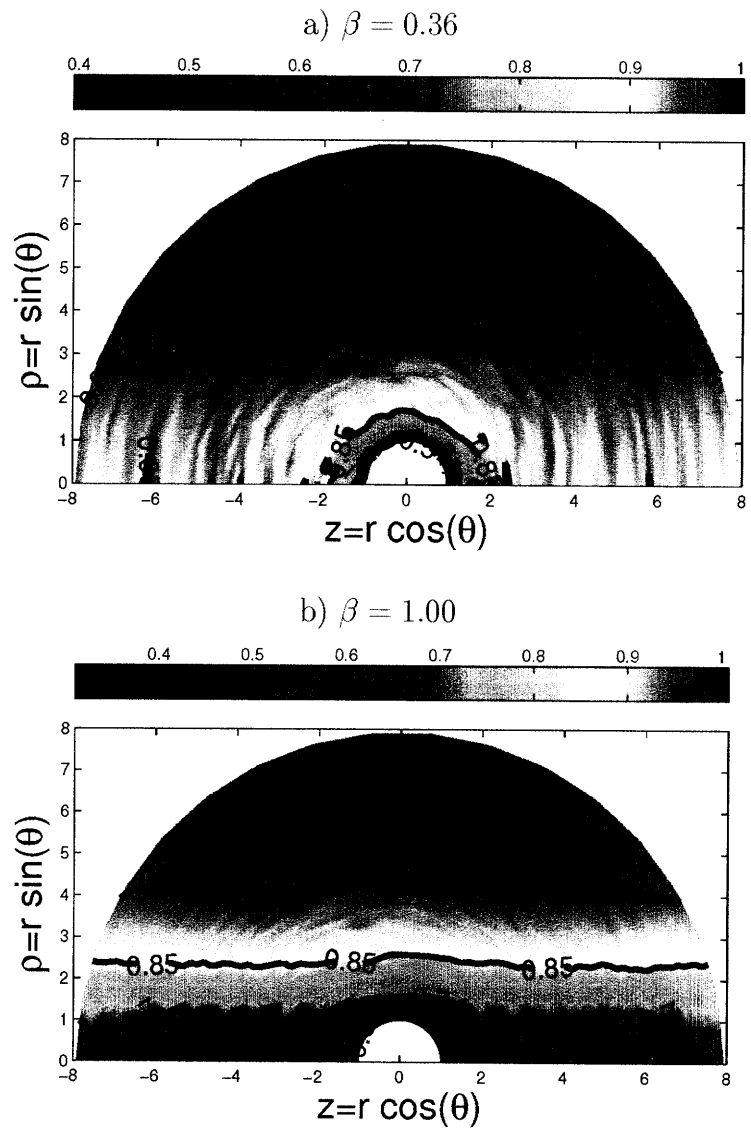


Figure III-3: Ion charge-density contour plots at $\bar{T}_i = 0.3$ in the quasineutral regime for $\beta = 0.36$ and $\beta = 1$. The solid lines are charge-density contours.

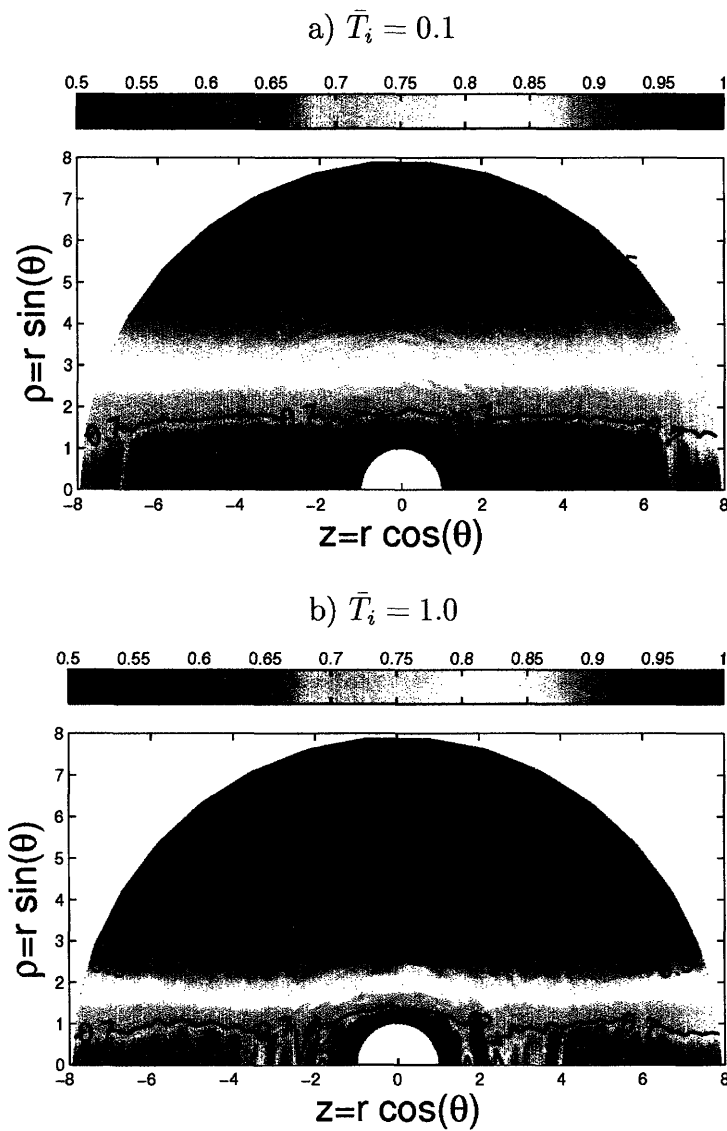


Figure III-4: Charge-density contour plots at $\beta = 1$ in the quasineutral regime for $\bar{T}_i = 0.1$ and $\bar{T}_i = 1.0$. The solid lines are charge-density contours.

in the transverse direction. Therefore Poisson's equation "smooths" the potential, and $\phi > \ln(\bar{n}_i)$. In this case it is not really appropriate to distinguish between sheath and presheath anymore.

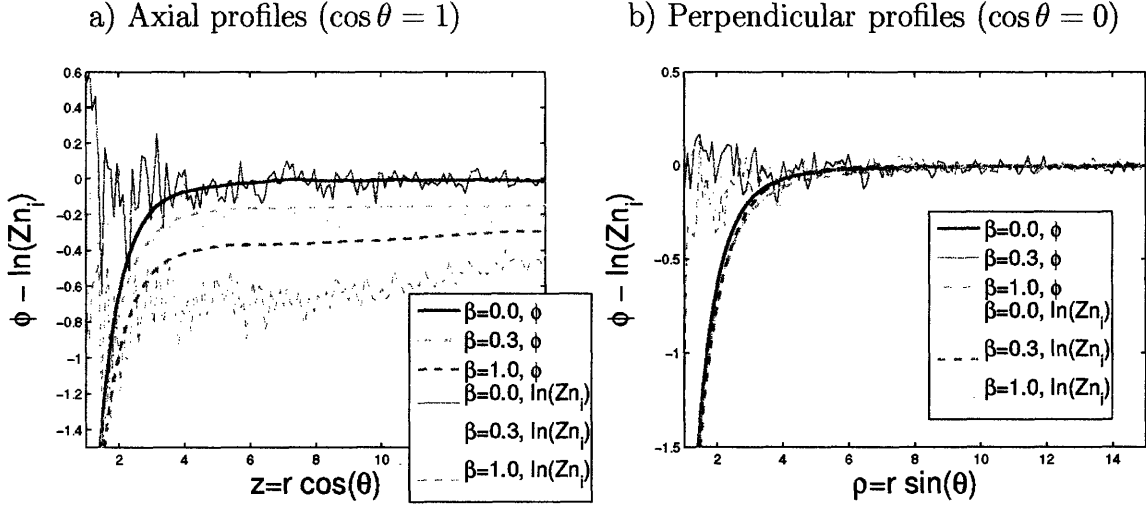


Figure III-5: Axial and Perpendicular space-charge profiles at $\bar{T}_i = 1$ and $\bar{\lambda}_{De} = 1$ for different magnetic fields strengths, and a probe potential $\phi_p = -3$. The density is shown as $\ln(Zn_i)$ in order to indicate the regions where quasineutrality is satisfied. On axis (Fig. a), the potential reaches an asymptote within the computational domain, although we see that at $\beta = 1.0$ we are at the limit of not satisfying $\partial\phi/\partial z = 0$. Increasing the domain size would not help, and this is an indication that our collisionless treatment would fail at higher magnetic fields. This issue is more visible on the ion density profile. Fig. b shows that the plasma density is approximately unperturbed in the transverse direction.

By comparing charge-density contour plots at two different Debye lengths, but with the other parameters kept fixed, one can see that in the magnetic shadow the transverse density variation only weakly depends on the shielding length. Fig. (III-6) shows such contour plots for $\bar{\lambda}_{De} = 0.3$ and $\bar{\lambda}_{De} = 3.0$, with $\beta = 1.0$ and $\bar{T}_i = 0.1$. In both cases, the contour lines $\bar{n}_i = 0.5$ and $\bar{n}_i = 0.7$ are at $\rho \sim 2$ and $\rho \sim 3$. Fig. (III-6b) ($\bar{\lambda}_{De} = 3.0$) shows a strong density enhancement at $\cos \theta \sim 0$ and $r \lesssim 4r_p$. This phenomenon, characteristic of strong focusing regimes, corresponds to the orbit accumulation shown in Fig. (III-1b).

Fig. (III-7) shows the potential contour plots for the same parameters. In this case the electron Debye length has a strong influence on the contour lines. In the vicinity of the probe where the equipotentials are closed, their spacing grows with

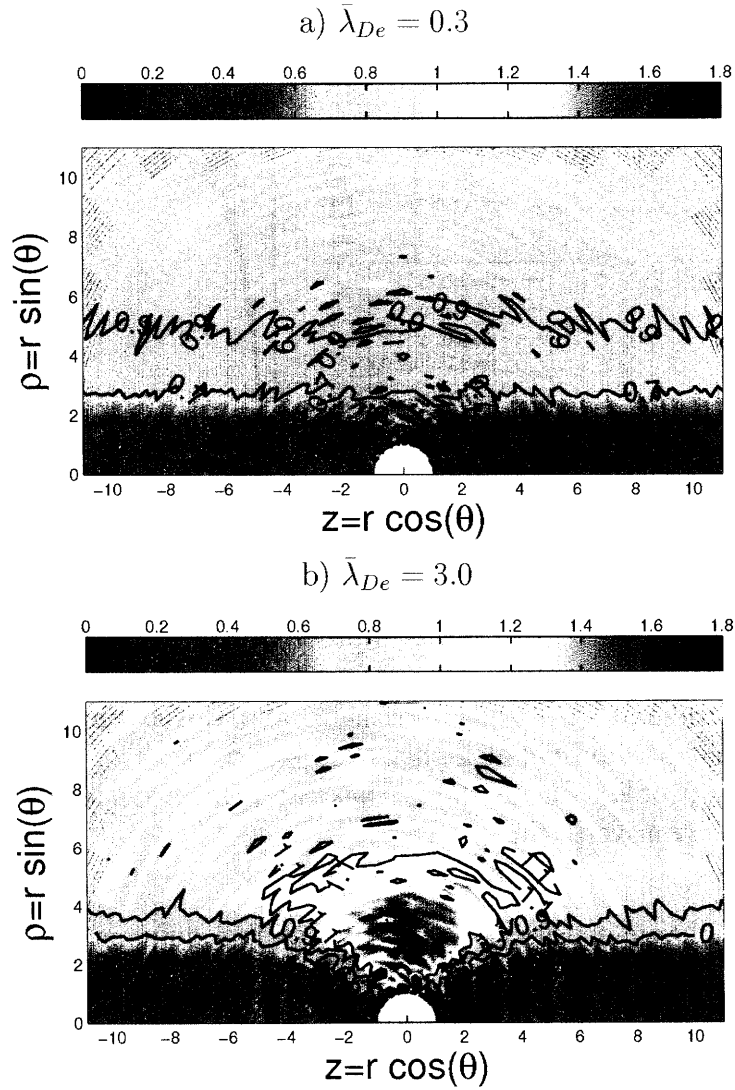


Figure III-6: Charge-density contour plots for $\bar{T}_i = 0.1$ and $\beta = 1.0$. The computational domain size is $r_b = 24r_p$, but for convenience we only show the region of interest. Although the color scale is bounded by $Zn_i = 1.8$, the ion charge-density reaches higher values in the accumulation region.

λ_{De} as expected. The magnetic shadow potential is higher (lower in magnitude) in the high Debye length case, since Poisson's equation operates a transverse smoothing of the potential over a few λ_{De} and the potential on axis "does not know" that the ion density is depleted there. Also because of this smoothing effect, the strong density enhancement at $\cos\theta \sim 0$ and $r \lesssim 4r_p$ is not translated into a potential barrier.

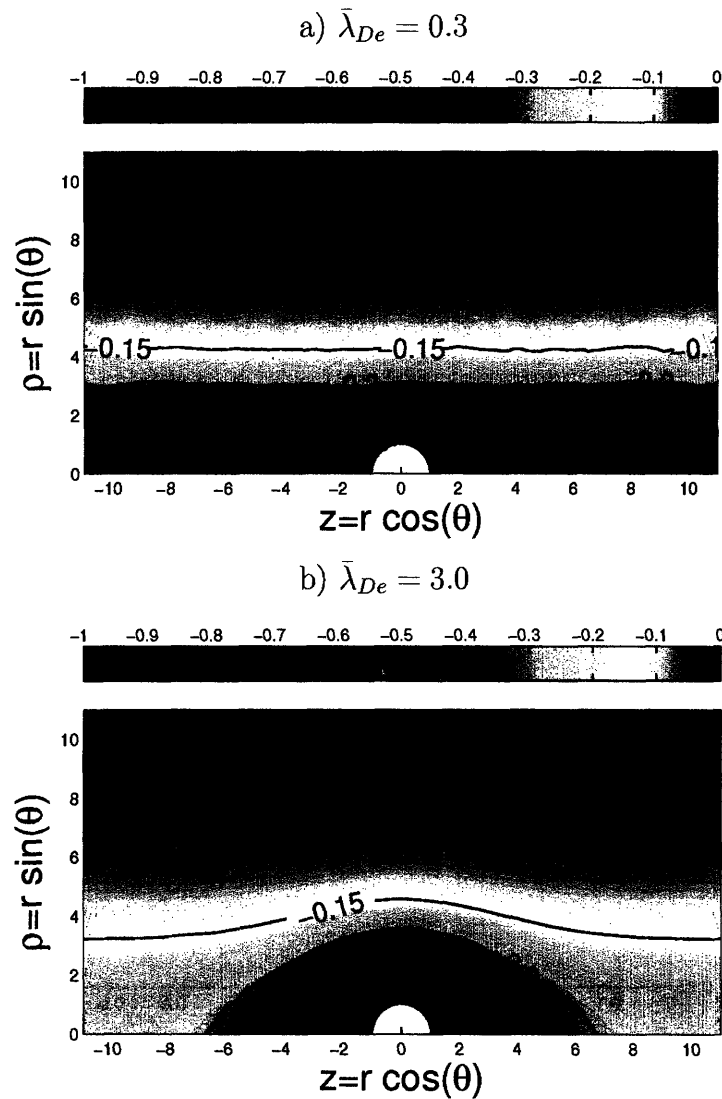


Figure III-7: Potential contour plots for $\bar{T}_i = 0.1$ and $\beta = 1.0$. The computational domain size is $r_b = 24r_p$, but for convenience we only show the region of interest.

III.3 Total ion current to the probe

III.3.1 Dependence on β

Fig. (III-8) shows the ion current dependence on β in the quasineutral regime ($\lambda_{De} = 0$) for three different ion temperatures. It clearly appears that for small β the dependence is linear, in accordance with the analytical calculations for a sphere at space-potential (Eq. (I.26)). Interestingly if we scale the ion current to its value at $\beta = 0$, the slope of this linear dependence is independent of \bar{T}_i . Fitting the ion current in the form:

$$I_i = I_i^{\beta=0} [1 - C_\beta \beta] + 0(\beta^2) \quad (\text{III.1})$$

we find $C_\beta = 0.21$. The free-flight calculations give $I_i^{\beta=0} = I_i^0$ and $C_\beta = 1/3\pi \sim 0.106$ (Eq. (I.24)).

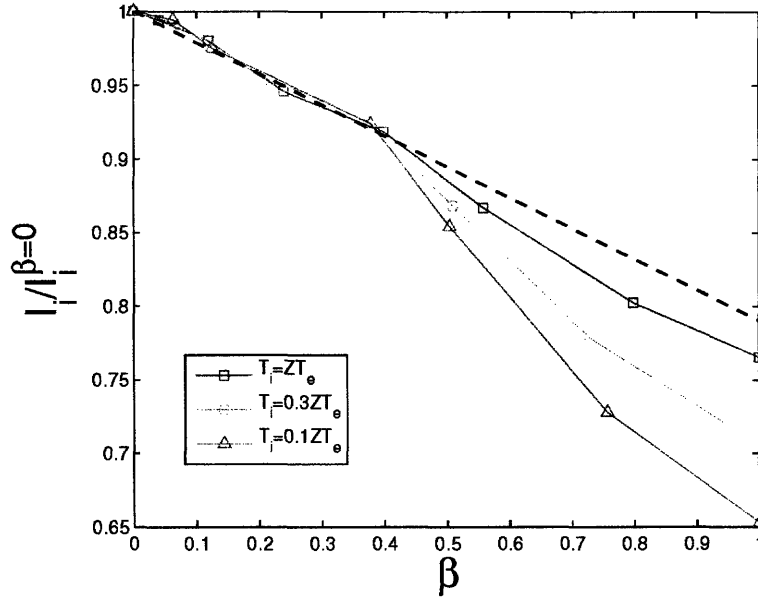


Figure III-8: Total ion current to the sphere as a function of the magnetic field for different ion temperatures, with $\bar{\lambda}_{De} = 0$. The current is scaled to its value at $\beta = 0$. $I_i^{\beta=0}(\bar{T}_i = 1.0) = 1.57I_i^0$; $I_i^{\beta=0}(\bar{T}_i = 0.3) = 2.49I_i^0$; $I_i^{\beta=0}(\bar{T}_i = 0.1) = 4.28I_i^0$. Also shown is the linear dependance given by Eq. (III.1) with $C_\beta = 0.21$.

Figs (III-9,III-10,III-11) show the ion current dependence on β for $\bar{T}_i = 1.0$, $\bar{T}_i =$

0.3 and $\bar{T}_i = 0.1$ when the shielding length is finite. The probe potential is set to $\phi_p = -3$. Also shown is the lower of the Helical and Canonical Upper bounds. As expected the current drops with a rising magnetic field, and the dependence at $\beta = 0$ is linear. We see that for our parameters, the ion current is systematically lower than the Upper bounds, except at $\bar{\lambda}_{De} \gg 1$ and $\beta = 0$ in which case the current is simply given by the OML formula (Eq. (I.35)).

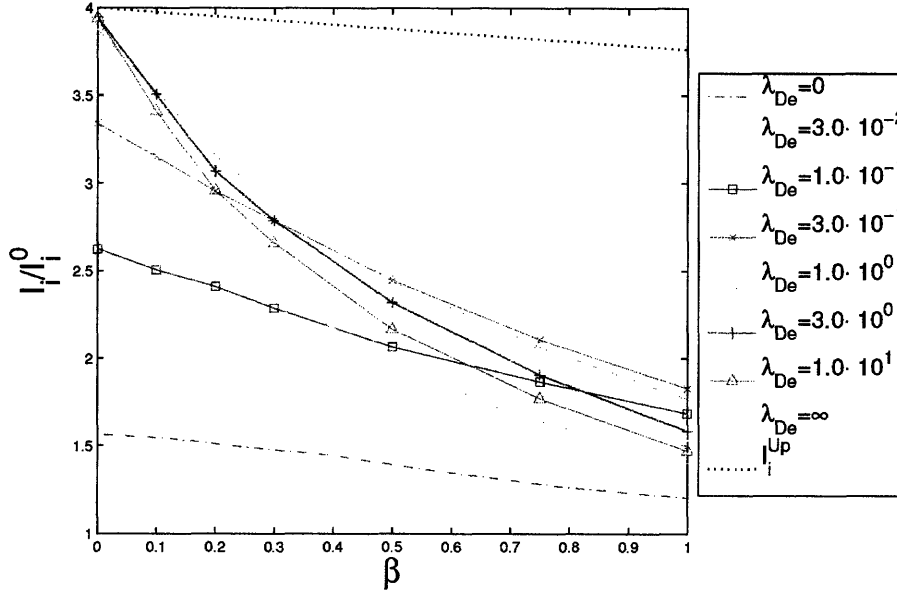


Figure III-9: Total ion current to the sphere as a function of the magnetic field for different electron Debye lengths at $\bar{T}_i = 1.0$ and $\phi_p = -3$. The values at $\bar{\lambda}_{De} = \infty$ are taken from Ref. [12]. Also shown as a dotted line is the lower of the Helical and the Canonical upper bounds (Eqs (I.43, I.78)).

III.3.2 Dependence on λ_{De}

Fig. (III-12) shows the evolution of the slope factor C_β occurring in Eq. (III.1), and defined as:

$$C_\beta = -\frac{1}{I_i^{\beta=0}} \frac{dI_i}{d\beta} \Big|_{\beta=0} \quad (III.2)$$

The slope factor is a rising function of λ_{De} , which is intuitive since the ion current must decrease from its value at $\beta = 0$ (a rising function of λ_{De}) to its value at $\beta = \infty$

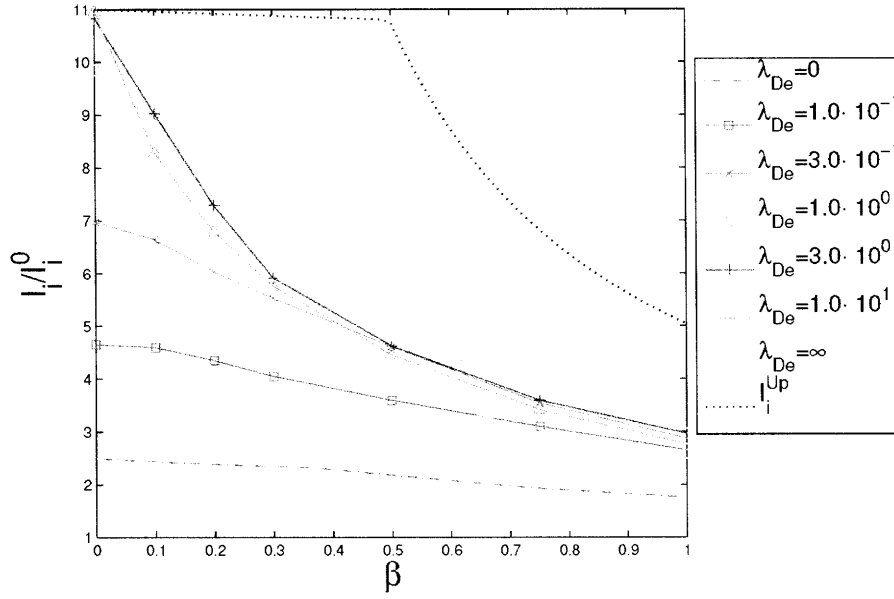


Figure III-10: Total ion current to the sphere as a function of the magnetic field for different electron Debye lengths at $\bar{T}_i = 0.3$ and $\phi_p = -3$. The figures at $\bar{\lambda}_{De} = \infty$ are taken from Ref. [12]. Also shown as a dotted line is the lower of the Helical and the Canonical upper bounds (Eqs (I.43, I.78)).

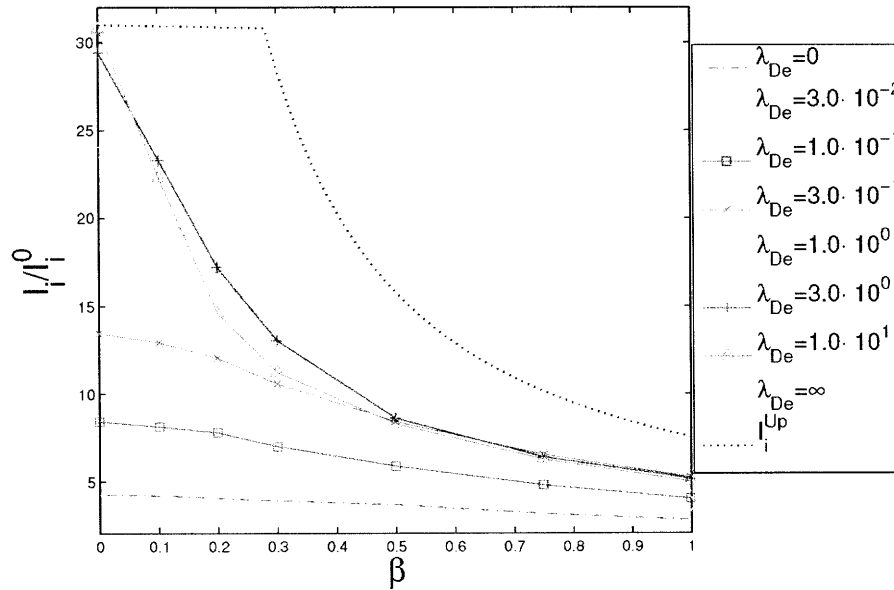


Figure III-11: Total ion current to the sphere as a function of the magnetic field for different electron Debye lengths at $\bar{T}_i = 0.1$ and $\phi_p = -3$. The figures at $\bar{\lambda}_{De} = \infty$ are taken from Ref. [12]. Also shown as a dotted line is the lower of the Helical and the Canonical upper bounds (Eqs (I.43, I.78)).

(independent of λ_{De} in our collisionless model). For $\bar{\lambda}_{De} \lesssim 0.3$, the slope factor does not depend on \bar{T}_i .

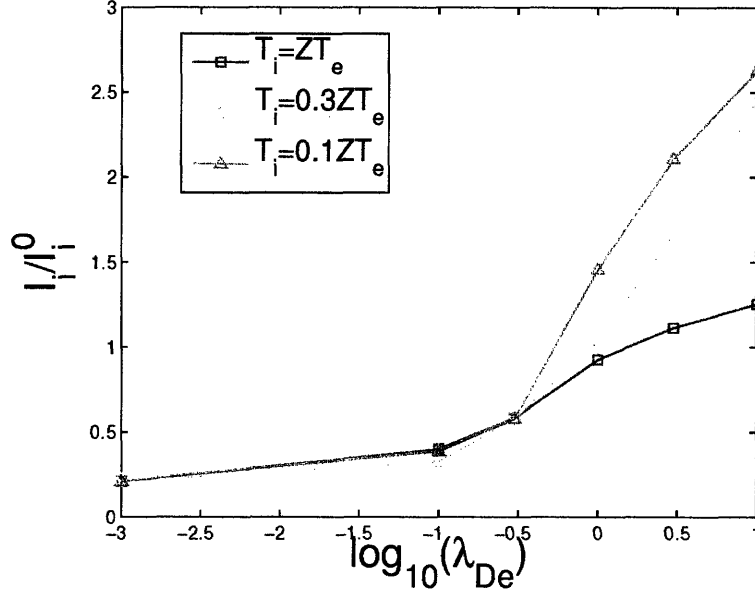


Figure III-12: Variation of the slope factor C_β with the electron Debye length. For the purpose of the semi-log plot, we assume $\bar{\lambda}_{De} = 1 \cdot 10^{-3}$ in the quasineutral regime.

It can be seen on Figs (III-9,III-11) that some current curves cross each-other: when the magnetic field is non zero, a large Debye length does not maximize the ion current. Fig. (III-13) shows the ion current dependence on λ_{De} at $\beta = 0.5$ in different regimes. It is found that the current systematically peaks at $\lambda_{De} \lesssim r_p$. The physics behind this result is a competition between two effects. If we raise the Debye length from $\bar{\lambda}_{De} \sim 1$ the current drops because the scale length of potential variation grows, hence the ions are accelerated more adiabatically. If we reduce $\bar{\lambda}_{De}$, we create intermediate potential barriers close to the probe, and the ion current drops as well.

III.3.3 Dependence on χ_p

If the current were exactly given by the Helical upper-bound limit (Eq. (I.78)), raising χ_p would increase the ion focusing on the probe, hence the ion current. On the other hand if the current were exactly given by the adiabatic limit (Eq. (I.79)), increasing

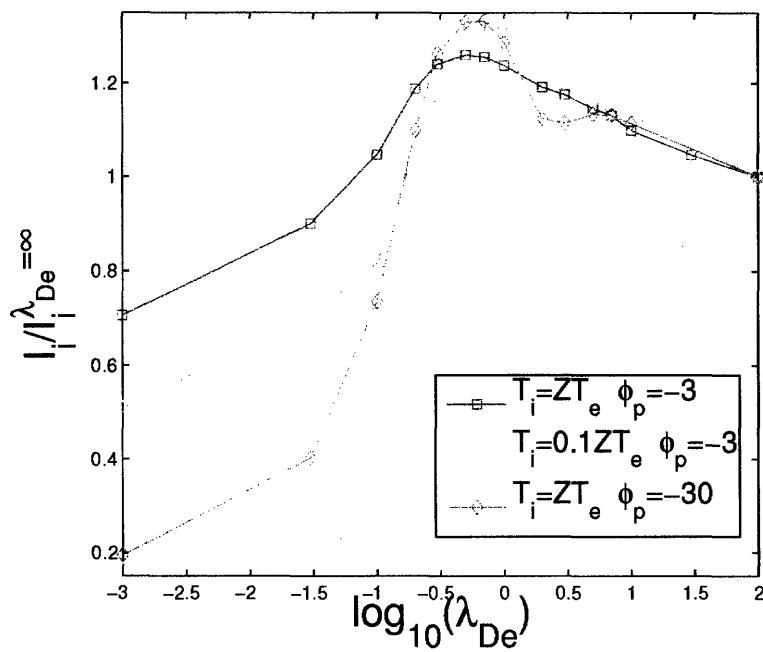


Figure III-13: Total ion current to the sphere as a function of λ_{De} for different combinations of ion temperature and probe potential, normalized to their value at $\bar{\lambda}_{De} = \infty$ taken from Ref. [12]. For the purpose of the semi-log plot, we assume $\bar{\lambda}_{De} = 1 \cdot 10^{-3}$ in the quasineutral regime, and $\bar{\lambda}_{De} = 1 \cdot 10^2$ in the Coulomb case.

χ_p would increase the average pitch-angle of the orbits close to the probe, resulting in a current reduction. Because the ion acceleration is never purely adiabatic or purely tri-dimensional, depending on the conditions the balance between those two effects can be positive or negative. Fig. (III-14) shows the ion current dependence on the probe potential under different magnetization conditions, for $\bar{T}_i = 1$ and $\bar{\lambda}_{De} = 1$. At least for $\beta \leq 1$, I_i is a rising function of χ_p .

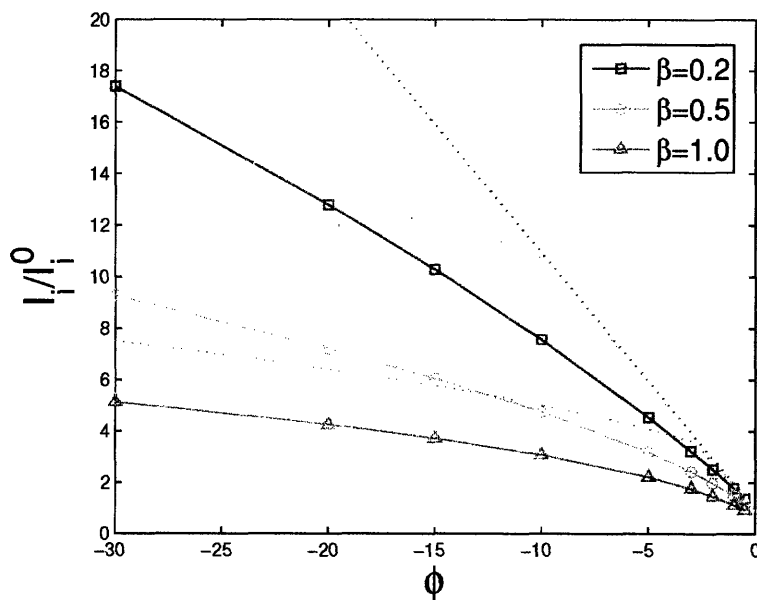


Figure III-14: Total ion current to the sphere as a function of its potential for different magnetic field strengths. $\bar{T}_i = 1$ and $\bar{\lambda}_{De} = 1$. For this ion temperature, $\chi_p = -\phi_p$. Also shown as dotted lines are the lower of the Helical and the Canonical upper bounds (Eqs (I.43, I.78)).

Sonmor and Laframboise [12] show that in the limit $\bar{\lambda}_{De} = \infty$, there are regimes where I_i decreases with χ_p . This usually involves $\beta \gg 1$, and is therefore outside our range of interest. At $\beta \leq 1$, the ion acceleration is not adiabatic enough for a “negative resistance” effect to show.

III.4 Angular distribution of the ion current

III.4.1 Quasineutral regime

Fig. (III-15) shows the angular distribution of the ion current to the probe for different values of β at $\bar{T}_i = 0.1$ and $\bar{T}_i = 1$, in the quasineutral regime. The main features of the plot are independent of the ion temperature. The angular distribution of collected current is flat at $\beta = 0$, and progressively becomes convex as β rises. Only for $\bar{T}_i = 0.1$ and $\beta \lesssim 0.01$ is the distribution concave.

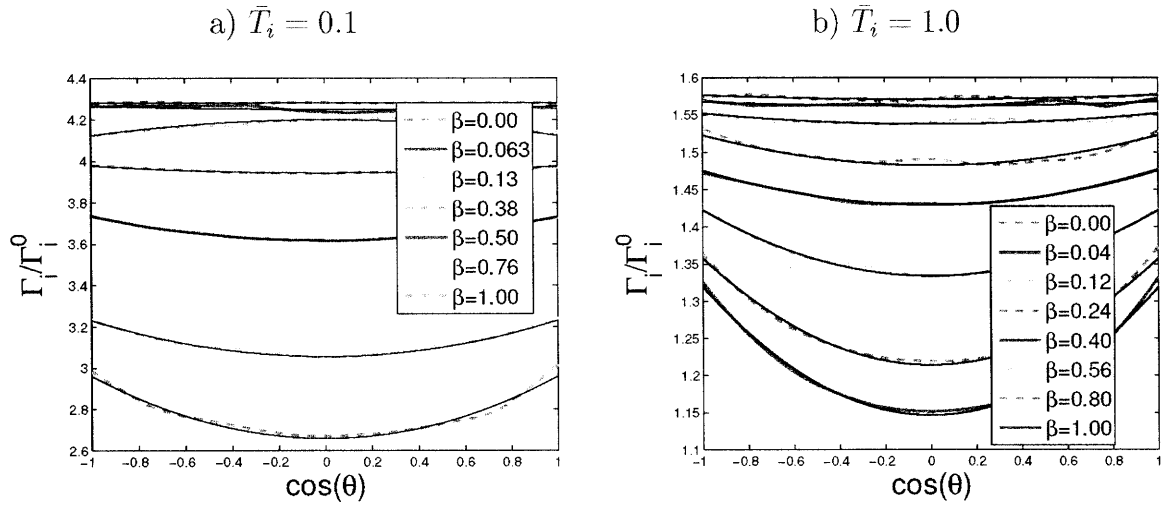


Figure III-15: Angular dependence of the ion flux density in units of $\Gamma_i^0 = n_\infty v_{ti}/2\sqrt{\pi}$ as a function of the magnetic field for $\bar{T}_i = 0.1$ and $\bar{T}_i = 1.0$ in the quasineutral regime, fitted to Eq. (III.3).

In order to quantify those features we can look for an even second order spherical harmonic fitting to those curves:

$$\Gamma_i = \Gamma_i^0 \frac{I_i}{I_i^0} \left(1 + A_\beta \frac{1}{2} (3 \cos^2 \theta - 1)\right). \quad (\text{III.3})$$

, where Γ_i^0 is the random flux density in a stationary unmagnetized plasma. A_β is a measure of the asymmetry introduced by the magnetic field, and I_i/I_i^0 is plotted on Fig. (III-8).

Fig. (III-15) shows that this choice of fitting is extremely satisfactory (The error on the flux is systematically less than 1%, which is below other uncertainties).

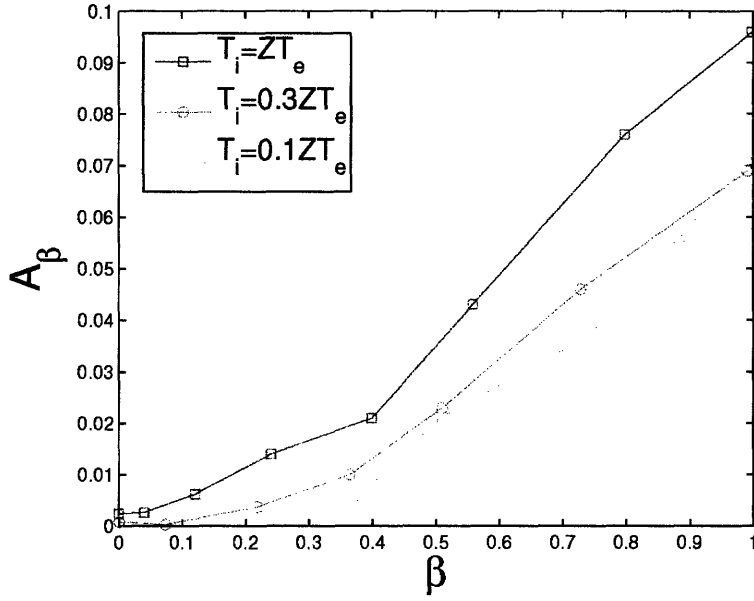


Figure III-16: A_β fitting parameter. A_β at $\bar{T}_i = 0.1$ and $\beta \lesssim 0.2$ is slightly negative, but its magnitude is below numerical uncertainties.

The fitting coefficient A_β is plotted on Fig. (III-16), and rises with β . However we expect from SCEPTIC an accuracy of 1% (within our hypothesis for the collisional presheath dynamics); therefore only the trend given by Fig. (III-16) is relevant, since the numerical values are of the order of 1%. At $\bar{T}_i = 0.1$ and $\beta \lesssim 0.2$ we find $A_\beta < 0$. Unfortunately the magnitude of A_β in this region is too low to say for sure if this negative value is physical.

III.4.2 Plasma with finite shielding

Fig. (III-17) shows the angular distribution of the ion flux density to the probe as a function of the shielding length for $\phi_p = -3$ and two different ion temperatures.

Fig. (III-17a) is similar to Fig. (III-15) in the sense that the collection is convex. In this case, $\bar{T}_i = 1.0$, hence $\chi_p = -\phi_p = 3$ and we are in a weakly focusing regime. Fig. (III-17b) shows that for highly focusing probes (Here $\bar{T}_i = 0.1$, hence $\chi_p = -10\phi_p = 30$) collection becomes concave. This difference is a direct consequence of the way ions are focused on the probe, as explained in Section III.1.

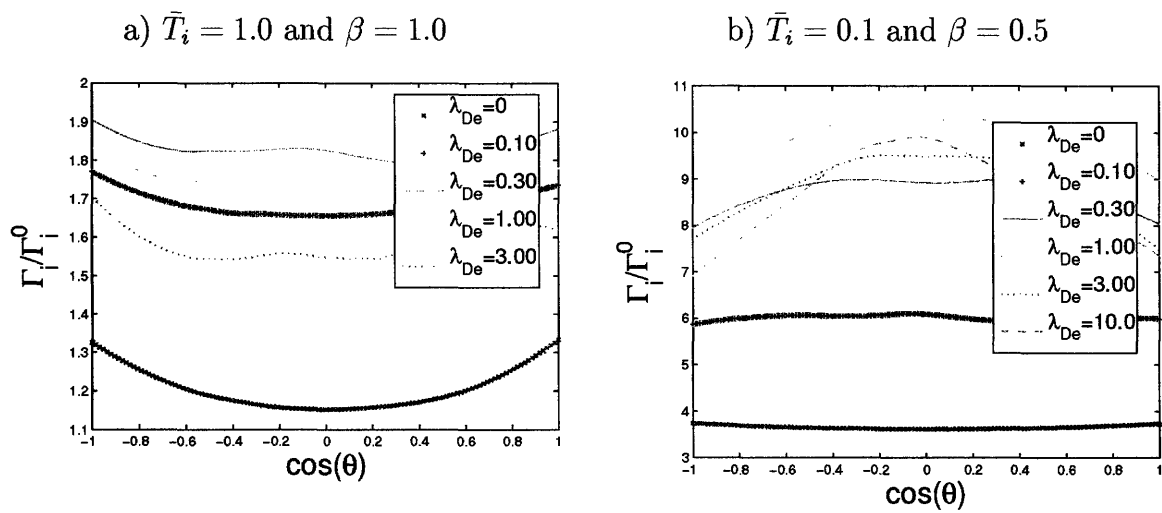


Figure III-17: Angular distribution of the ion flux density to the probe for $\phi_p = -3$. In a weakly focusing regime (Fig. a) the collection is convex, while it is concave in the opposite situation (Fig. b).

Chapter IV

Solutions for a flowing plasma

IV.1 Cold ion orbits in a flowing plasma

Because the spherical symmetry of the problem is broken by a plasma drift regardless of the magnetic field strength, the distinction between weakly and strongly focusing regimes has already been pointed out by Hutchinson [3] in the context of unmagnetized plasmas. Although it was known that probe focusing causes the density to peak downstream, Hutchinson found the unexpected result that for $T_i \lesssim 0.1ZT_e$ and $\lambda_{De} \sim r_p$, the focusing is strong enough to induce a reversal of the angular distribution of ion flux density to the sphere. In other words, in this regime the probe collects more current downstream than upstream.

Fig. (IV-1) shows some ion orbits with $\bar{\lambda}_{De} = 1.0$, $\bar{T}_i = 0.1$ and $\bar{v}_d = 1.0$ at $\beta = 0$. In order to emphasize that $v_{ti} \ll v_d$, only orbits whose initial velocity is equal to the drift velocity are plotted; the simulation has obviously been run with the full ion distribution function. For the purpose of showing more visible orbits, in this section SCEPTIC has been used with a θ -averaged potential as in Section III.1. None of our conclusions are affected by this manipulation.

It can be seen that the probe strongly focuses the ion flux at $\cos \theta \sim 1$. Although the radial (ρ) spacing between collection orbits downstream is higher than upstream, the poloidal (φ) spacing at a point of cylindrical radius ρ is reduced by an amount ρ_∞/ρ , where ρ_∞ is the orbit impact parameter. Because of particle conservation,

the flux asymmetry is reversed if the poloidal reduction overcompensates the radial increase. For the particular example shown in Fig. (IV-1) this is the case.

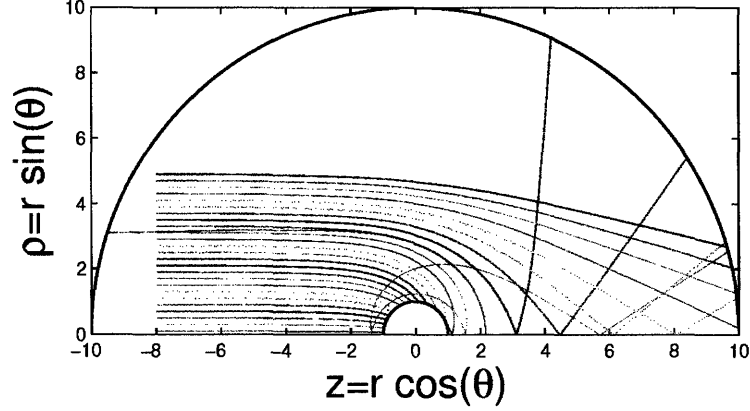


Figure IV-1: Cold ion orbits for $\bar{T}_i = 0.1$, $\bar{v}_d = 1$, $\phi_p = -4$ and $\bar{\lambda}_{De} = 1$ for $\beta = 0$. The probe strongly focuses the ion flux downstream, resulting in a reversal of the flux-density collection asymmetry.

The effect of a magnetic field parallel to \mathbf{v}_d on cold orbits is to create a depletion cone downstream, whose angle grows with β . This situation is similar to what we have seen in Fig. (III-1) for a stationary plasma, the difference being that in a flowing plasma cold ions only come from upstream, hence no current at all is collected in the depletion region. Fig. (IV-2) shows ion orbits whose initial velocities are equal to the drift velocity (Cold plasma limit) for the same parameters as Fig. (IV-1), at two different magnetic field strengths.

Fig. (IV-3) illustrates the influence of the shielding length on cold orbits, still using a θ -averaged potential. For this purpose, it is assumed that $\beta = 1$, $\bar{T}_i = 0.1$, and $\bar{v}_d = 1.0$. When λ_{De} is small, the potential gradients are confined in a thin crown around the probe, therefore orbits whose initial impact parameter is large enough are barely affected. In the opposite limit of large electron Debye length, the probe perturbs the plasma on a longer scale-length. The depletion cone angle however does not depend on λ_{De} .

In order to quantify the angular aperture of the depletion cone, we recall that conservation of energy and canonical angular momentum for a cold ion reads (Eq. I.40):

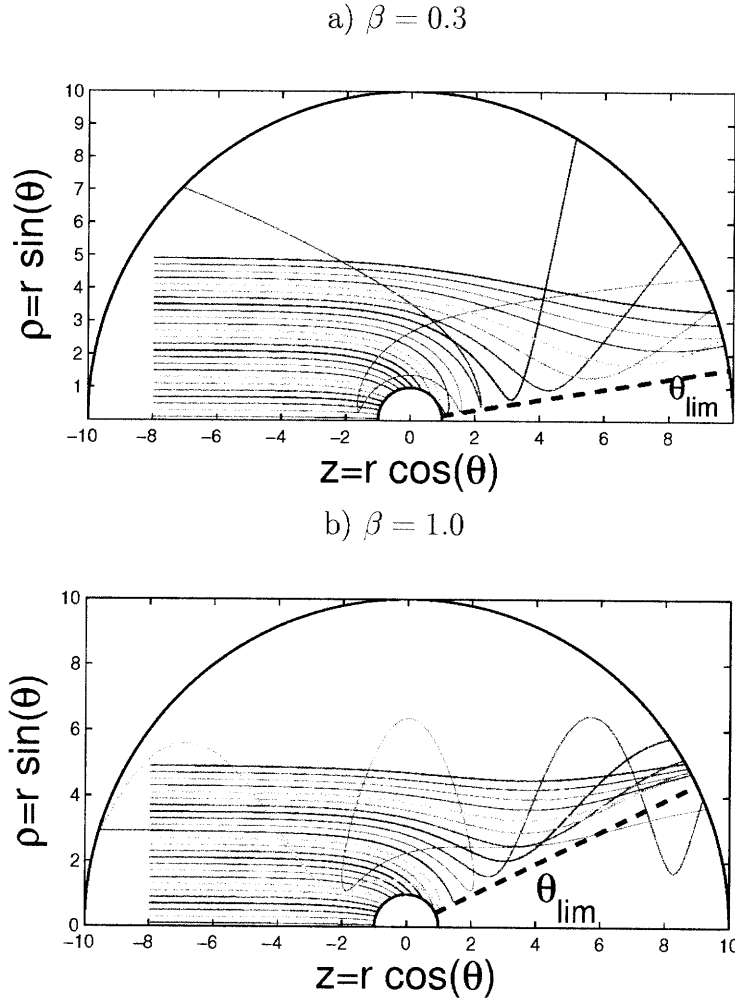


Figure IV-2: Cold ion orbits for $\bar{\lambda}_{De} = 1$, $\bar{T}_i = 0.1$, $\phi_p = -4$ and $\bar{v}_d = 1$ for two different magnetic field strengths. Also shown by a dashed line is the depletion cone, whose angle θ_{lim} is given by Eq. (IV.10).

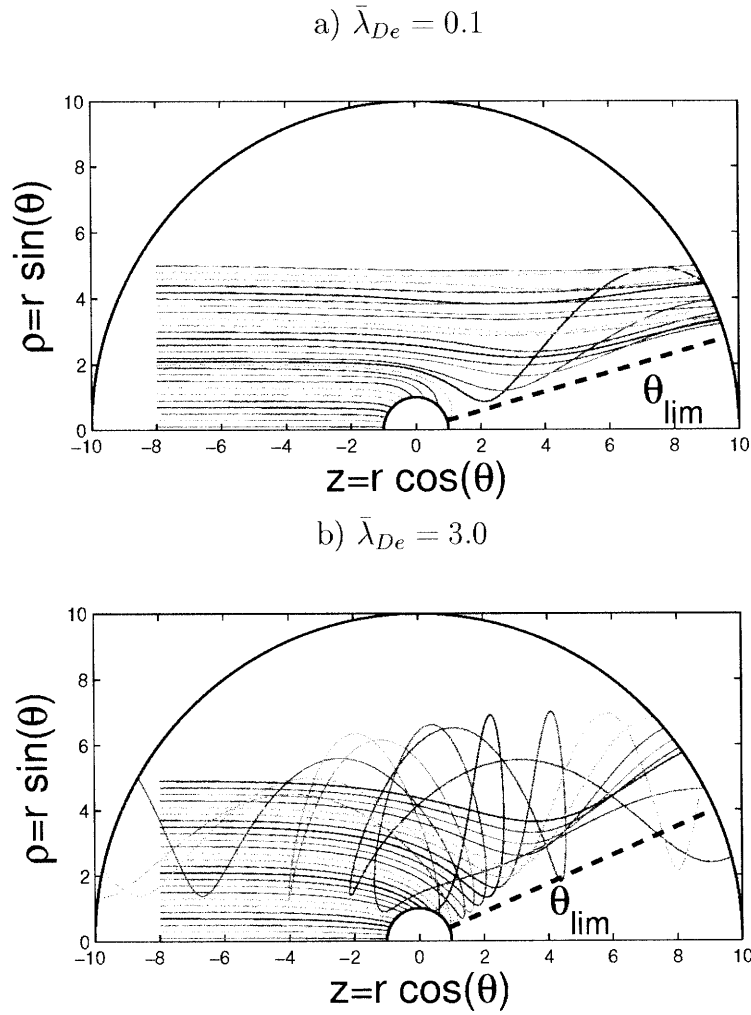


Figure IV-3: Cold ion orbits for $\beta = 1$, $\bar{T}_i = 0.1$, $\phi_p = -4$ and $\bar{v}_d = 1$ for two different electron Debye lengths. Also shown by a dashed line is the depletion cone, whose angle θ_{lim} is given by Eq. (IV.10).

$$\rho^2 \geq \frac{\rho_\infty^2}{1 + \frac{2m_i}{ZeB} \left[\frac{2}{m_i \rho^2} \left(\frac{1}{2} m_i v_d^2 - ZeV(\rho, z) \right) \right]^{1/2}} \quad (\text{IV.1})$$

The preceding equation can be rewritten as:

$$\rho \geq \frac{\rho_\infty^2 \Omega}{\Omega \rho + 2\sqrt{2} \left[\frac{1}{2} v_d^2 - ZeV(\rho, z)/m_i \right]^{1/2}} \quad (\text{IV.2})$$

(ρ, z) is the trajectory of an ion whose impact parameter is ρ_∞ . In the vicinity of the probe if $\beta \leq 1$ and $\bar{T}_i \leq 0.1$, it is in practice always the case that:

$$2\sqrt{2} \left[\frac{1}{2} v_d^2 - ZeV(\rho, z)/m_i \right]^{1/2} \gg \Omega \rho \quad (\text{IV.3})$$

For example in the unfavorable case $\bar{v}_d = 0$, if we take $\phi = \phi_p = -2.5$, $\rho = r_p$ and $\bar{\Omega} = 0.4$ (corresponding to $\beta \simeq 1$ for $\bar{T}_i = 0.1$), Eq. (IV.3) is equivalent to $4.47 \gg 0.4$. Eq. (IV.2) can therefore be simplified as:

$$\rho \geq \frac{\rho_\infty^2 \Omega}{2\sqrt{2} \left[\frac{1}{2} v_d^2 - ZeV(\rho, z)/m_i \right]^{1/2}} \quad (\text{IV.4})$$

Because it is more convenient to work in spherical coordinates, we rewrite

$$\rho = r \sin \theta = r_p \left(1 + \frac{\delta}{r_p} \right) \sin \theta \quad \text{where} \quad \delta = r - r_p \quad (\text{IV.5})$$

If we approximate the potential as Debye-Hückel with shielding length λ_s (Eq. (I.53)), then:

$$V(r) = V_p \left(1 - \frac{\delta}{r_p} - \frac{\delta}{\lambda_s} \right) + O(\delta^2) \quad (\text{IV.6})$$

Let us assume that the impact parameter of the last collection orbit, ρ_∞^0 , is known. To first order in δ , there exists an unknown constant k such that $\rho_\infty = \rho_\infty^0 \left(1 + k \frac{\delta}{\rho_\infty^0} \right)$. Eq. (IV.4) becomes:

$$r_p \left(1 + \frac{\delta}{r_p}\right) \sin \theta \geq \frac{(\rho_\infty^0)^2 \Omega (1 + 2k \frac{\delta}{\rho_\infty^0})}{2\sqrt{2} \left[\frac{1}{2}v_d^2 - \frac{ZeV_p}{m_i}\right]^{1/2}} \left[1 - \frac{ZeV_p/m_i}{2 \left[\frac{1}{2}v_d^2 - \frac{ZeV_p}{m_i}\right]} \left(\frac{\delta}{r_p} + \frac{\delta}{\lambda_s}\right)\right] \quad (\text{IV.7})$$

Because in most of the cases $\frac{1}{2}v_d^2 \ll \frac{ZeV_p}{m_i}$, to first order in δ Eq. (IV.7) can be expanded as follows:

$$\sin \theta \geq \frac{(\rho_\infty^0)^2 \Omega / r_p}{2\sqrt{2} \left[\frac{1}{2}v_d^2 - \frac{ZeV_p}{m_i}\right]^{1/2}} [1 + \kappa \delta] \quad (\text{IV.8})$$

with κ defined by:

$$\kappa = \frac{1}{2\lambda_s} - \frac{1}{2r_p} + \frac{2k}{\rho_\infty^0} \quad (\text{IV.9})$$

If $\kappa \geq 0$, cold orbits are depleted in a cone centered on the probe with aperture angle given by:

$$\sin \theta_{\text{lim}} = \frac{(\rho_\infty^0)^2 \Omega / r_p}{2\sqrt{2} \left[\frac{1}{2}v_d^2 - \frac{ZeV_p}{m_i}\right]^{1/2}} \quad (\text{IV.10})$$

If $\lambda_s \leq r_p$, κ is necessarily positive. For longer shielding lengths this property can not be proved, although it is in practice always satisfied. Indeed as shown in Fig. (IV-3b), for $\bar{\lambda}_{De} \gtrsim 1$ the spacing between orbits close to the probe downstream is approximately equal to their spacing upstream at infinity. Therefore in this situation $k \sim 1$, and unless $\rho_\infty^0 \geq 4$, κ is positive.

When $\bar{T}_i \ll 1$, ρ_∞^0 can easily be evaluated if the total current to the probe is known, using the formula:

$$\pi(\rho_\infty^0)^2 n_\infty v_d = I_i \quad (\text{IV.11})$$

Because the orbits are readily available in our plots however, θ_{lim} in Figs (III-1, IV-2, IV-3) has been calculated with the “real” ρ_∞^0 .

θ_{lim} is an accurate estimate of the depletion cone aperture only to first order in $\delta = r - r_p$, and in the limit $\bar{T}_i \ll 1$. It is however interesting to notice that experimentally its validity extends a few r_p from the probe surface (See Figs (III-1, IV-

2,IV-3)). When $v_{ti} \gtrsim \min(v_d, v_{ti}\sqrt{\chi_p})$, transverse thermal motion blurs the depletion cone boundary, and θ_{lim} must then only be seen as a scaling parameter.

An important point to notice is that the magnetic field enters in θ_{lim} under the non-dimensional form $\frac{\Omega r_p}{v_p}$, where v_p is a typical particle velocity at the probe edge. Therefore β does not directly control the depletion cone width.

IV.2 Space-charge distribution

IV.2.1 Quasineutral regime

Fig. (IV-4) shows the radial dependence of the density upstream and downstream for two very different situations, in the quasineutral regime.

If the flow is subthermal, the density distribution at $\beta = 0$ is highly symmetric far enough from the probe and similar to what we would get in the flow-free case. As β rises this symmetry breaks; since the ion mobility across the field lines is reduced, the density upstream rises past the flow-free level and the density downstream drops. The important point however is that the density still reaches an asymptote within our computational domain.

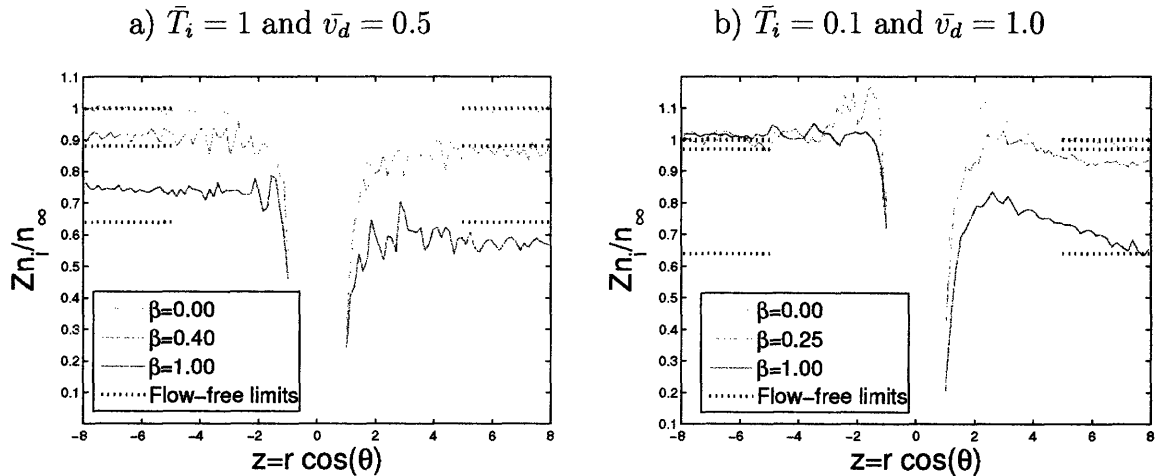


Figure IV-4: Upstream and Downstream ion charge-density as a function of z ($|\cos\theta| = 1$) for different magnetic field strengths in the quasineutral regime. Fig. a is for $\bar{T}_i = 1$ and $\bar{v}_d = 0.5$, the flow is therefore subsonic. Fig. b is for $\bar{T}_i = 0.1$ and $\bar{v}_d = 1.0$, the flow is therefore suprathermal and approximately sonic. The dotted lines correspond to the asymptotic limit of the charge-density in the flow-free case.

If the flow is suprathermal, the drift velocity approaches the sound speed and the Bohm criterion is nearly satisfied by the flow at infinity: the upstream charge-density is therefore hardly perturbed. Because the plasma is cold, there is little thermal motion across the field lines, and increasing a magnetic field parallel to the plasma drift does not influence this result.

The downstream side is on the contrary affected by a change in β . As β rises, the density there is reduced because of the depletion cone discussed in Section IV.1. For $\beta = 1$, we notice that the collisionless perturbation downstream extends out of the computational domain. This is not an issue since the number of ions entering the computational domain from the downstream side is negligible compared to the ions entering upstream. Because in the quasineutral regime outer boundary conditions on the potential are not required, there is no need to extend the domain.

It has been pointed out by Hutchinson [2] that at low ion temperatures Landau Damping is weak enough to allow the formation of a Mach-cone for sufficiently high flow velocities. However even in the regime $v_d \lesssim c_s$ a Mach-cone shaped rarefaction sometimes forms. The angle made by this rarefaction with the drift axis is different from the standard Mach-cone angle given by

$$\theta_{\text{Mach}} = \arcsin(v_d/c_s) \quad (\text{IV.12})$$

, because the underlying physics is different. In the present case, it can be seen on Fig. (IV-1) that for $z \gtrsim 1$, orbit spacing is increased by the probe focusing. At $\cos \theta \sim 1$ this effect is compensated by the reduction in cross-sectional area $2\pi\rho d\rho$ (This is the effect discussed in Section IV.1 causing the ion flux asymmetry reversal). At $\cos \theta \sim 0$, the orbits are not significantly deflected yet, hence the density is hardly perturbed. There is however an angle in between where the density decreases.

As can be seen in Fig. (IV-5), the effect of the magnetic field is to shift the Mach-cone shaped rarefaction down to the magnetic axis.

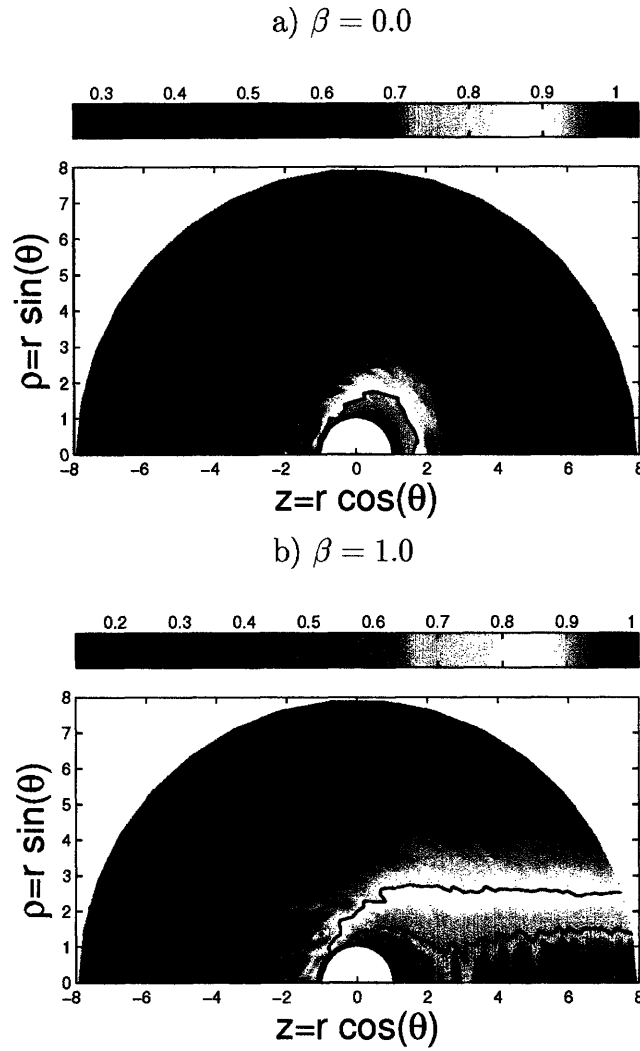


Figure IV-5: Charge-density contour plots for $\bar{T}_i = 0.3$ and $\bar{v}_d = 1.0$ in the quasineutral regime. a) $\beta = 0.0$. b) $\beta = 1.0$. The contour lines are for $Zn_i = 0.7, 0.85, 0.95, 0.98n_\infty$. The Mach-cone shaped rarefaction is shifted towards the drift axis by the magnetic field.

IV.2.2 Plasma with finite shielding

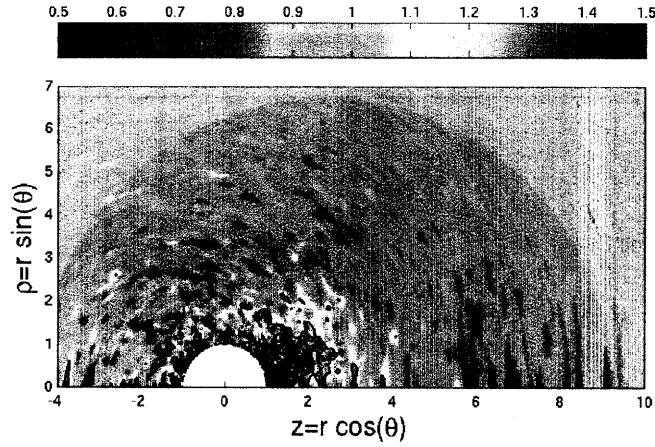
As explained in Section III.1, the focusing properties of the probe are maximal when the shielding length is of the order of the probe radius. When the plasma is flowing and no background magnetic field is present, this results in a strong density peak downstream [3].

Fig. (IV-6) shows the evolution of this density peak when the background magnetic field strength rises, for $\bar{\lambda}_{De} = 1.0$, $\bar{T}_i = 1.0$, and $\bar{v}_d = 1.5$. In accordance with the cold ion orbits picture developed in Section IV.1, the background magnetic field causes an ion depletion in the downstream side of the magnetic shadow. In the present case $\bar{T}_i \neq 0$, therefore the depletion is not total. The transition between the unmagnetized and magnetized regime occurs at $\beta \sim 0.5$. Indeed Fig. (IV-6b) shows simultaneously the density peak due to ion focusing and, starting a few r_p from the probe edge, the ion-depleted magnetic shadow.

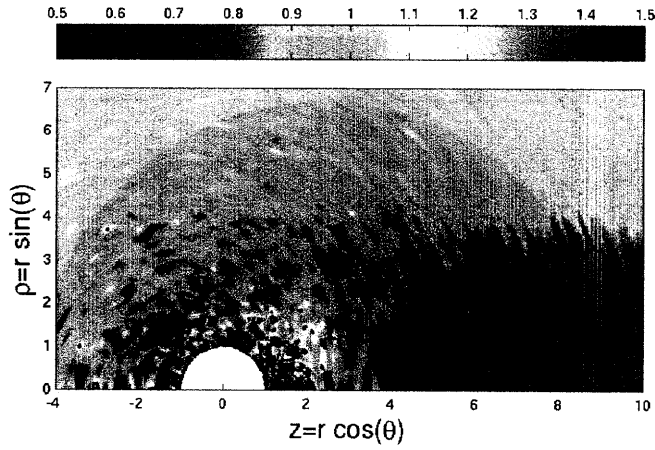
The qualitative differences between the charge-density and potential contour plots when the electron Debye length is non zero arise from the smoothing operated by Poisson's equation over a range of a few λ_{De} , and have already been discussed in Section III.2.2 in the context of stationary plasmas. The potential contour plots corresponding to Fig. (IV-6) are shown in Fig. (IV-7). At $\beta \gtrsim 1.0$ it can be seen on Fig. (IV-7c) that the $\phi = -0.02$ contour line opens upstream. For $\bar{v}_d \gtrsim 2$ this would not be the case since the Bohm criterion would be naturally satisfied by the flow at infinity.

When the temperature is low and the shielding length of comparable magnitude with the probe radius, the wake shows three different regions. Fig. (IV-8) illustrates this phenomenon for the case $\bar{T}_i = 0.01$, $\bar{v}_d = 2$, $\phi_p = -3$, $\bar{\lambda}_{De} = 1$ and $\beta = 1$. At very small θ can be seen the depletion cone due to the magnetic field. The white solid line shows the region delimited by θ_{lim} , calculated using Eqs (IV.10,IV.11). For this purpose we used additional information provided by SCEPTIC, namely the total collected current $I_i = 31.2I_i^0$. For the considered parameters, $\bar{\Omega} = \beta\sqrt{\bar{T}_i\pi/2} = 0.125$. At an angle $\theta = \theta_{Mach}$ (Eq. (IV.12)), the V-shaped depletion region characteristic of

a) Zn_i/n_∞ for $\beta = 0.2$



b) Zn_i/n_∞ for $\beta = 0.5$



c) Zn_i/n_∞ for $\beta = 1.0$

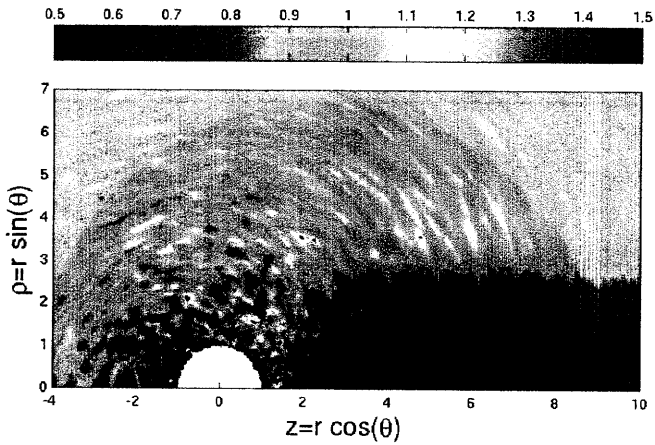


Figure IV-6: Evolution of the ion charge-density distribution with a rising magnetic field at $\bar{T}_i = 1.0$, $\bar{\lambda}_{De} = 1.0$, $\bar{v}_d = 1.5$ and $\phi_p = -5$. The computation has been performed on a domain of size $r_b = 20r_p$, but only the region of interest is shown.

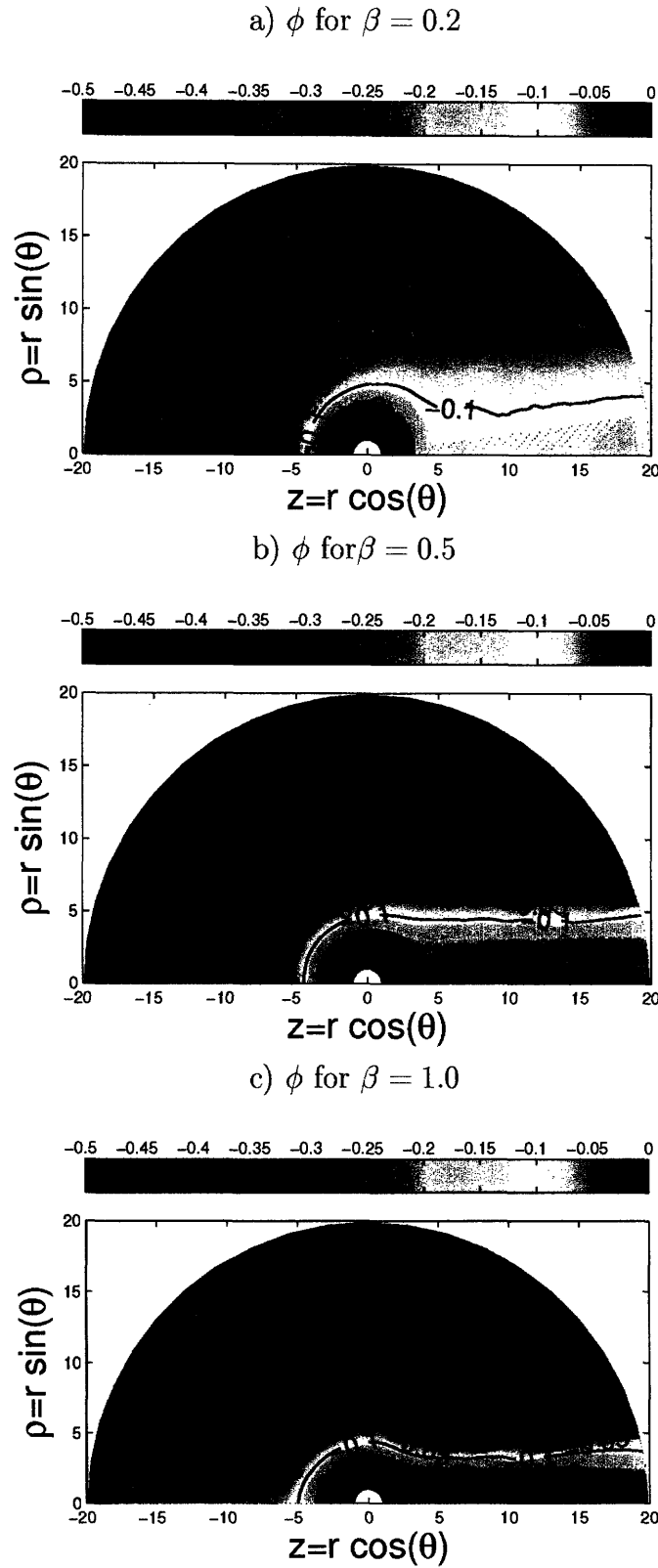


Figure IV-7: Evolution of the potential distribution $\phi(\mathbf{r})$ with a rising magnetic field at $\bar{T}_i = 1.0$, $\bar{\lambda}_{De} = 1.0$, $\bar{v}_d = 1.5$ and $\phi_p = -5$.

Mach-cones is present, shown as a white dashed line in the charge-density contour plot. Because of the negligible ion temperature, the sound speed is simply given by $\bar{c}_s = 1$, hence the Mach number is $M = 2$. On the other hand, the ion charge-density in the region $\theta \in [\theta_{\text{lim}} : \theta_{\text{Mach}}]$ is much higher than n_∞ , due to probe focusing. Because the drift velocity is high, the density peak detaches from the immediate downstream region, and extends on a long, linear stripe.

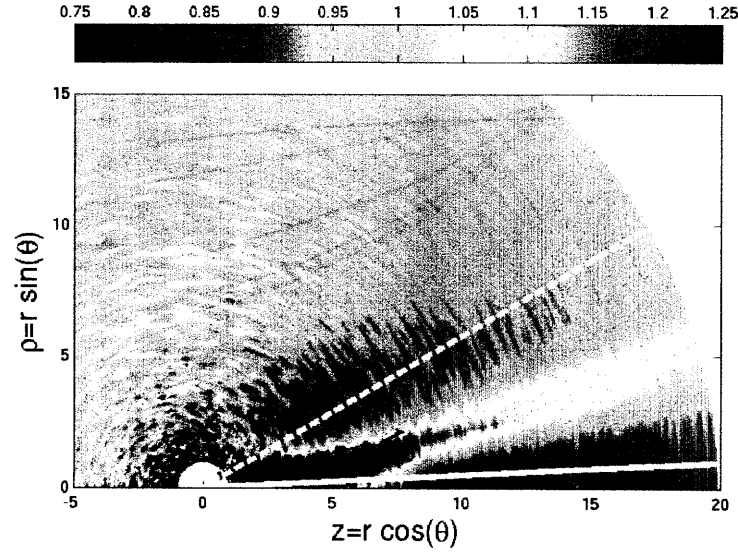


Figure IV-8: Charge-density contour plot of the downstream wake in a supersonic, magnetized regime. Here $\bar{T}_i = 0.01$, $\bar{v}_d = 2$, $\phi_p = -3$, $\bar{\lambda}_{De} = 1$ and $\beta = 1$. The dashed line indicates the Mach cone (θ_{Mach}), and the solid line the magnetic depletion cone (θ_{lim}).

IV.3 Total collected current

Fig. (IV-9) shows the ion current dependence on β at $\bar{T}_i = 1.0$, $\phi_p = -5$ and $\bar{\lambda}_{De} = 1.0$, for several drift velocities.

This dependence can be seen to be linear in β for low β , and the slopes decrease with an increasing magnetic field. This is in agreement with our results for the sphere at space potential (See Fig. (I-5)) although the slope magnitudes are obviously

different. Because the electron Debye length is equal to the probe size, the current at $\beta = 0$ is slightly lower than the OML value given by Eq. (I.34). However for $\beta \lesssim 0.3$ it can be seen that the current drops with a rising drift velocity, a property typical of the unmagnetized OML regime (See Fig. (B-3a)). For $\beta \gtrsim 0.3$, the current rises with the drift velocity as expected.

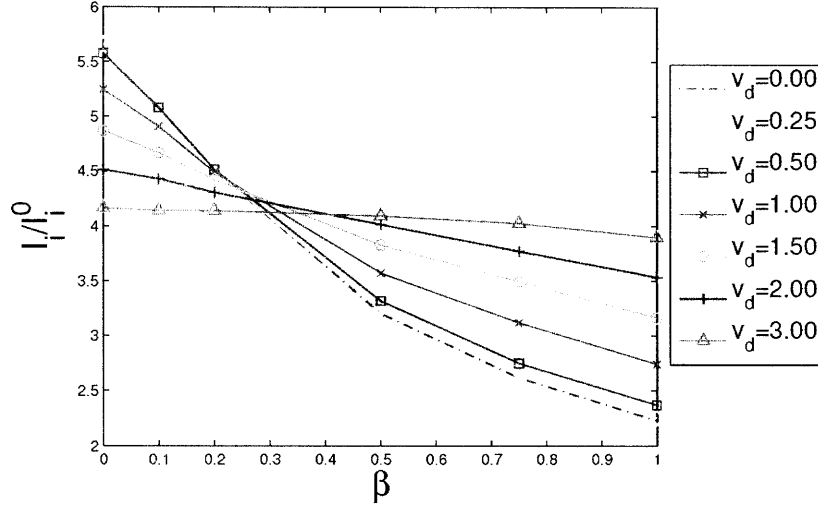


Figure IV-9: Total ion current to the sphere as a function of the magnetic field for different drift velocities at $\bar{T}_i = 1.0$, $\bar{\lambda}_{De} = 1.0$ and $\phi_p = -5$.

For lower shielding lengths the picture is slightly different, as can be seen on Fig. (IV-10). In this case the current rises with v_d regardless of the magnetic field.

IV.4 Angular distribution of the ion current for weakly focusing probes

IV.4.1 Quasineutral regime

The main purpose of a Mach probe is to determine the drift velocity of a plasma, usually by comparing the upstream flux density (Γ_i^U) with the downstream flux density (Γ_i^D). In the unmagnetized or the strongly magnetized case, different heuristic and theoretical models have been developed, most of them expressed as a calibration

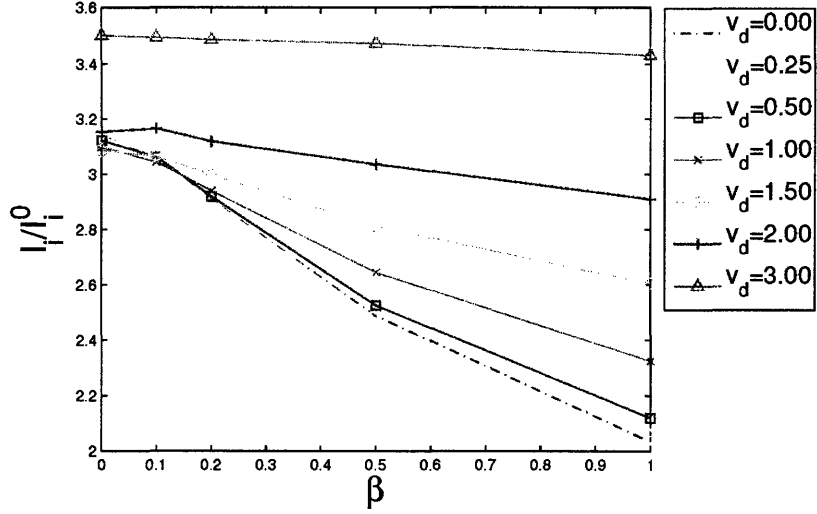


Figure IV-10: Total ion current to the sphere as a function of the magnetic field for different drift velocities at $\bar{T}_i = 1.0$, $\bar{\lambda}_{De} = 0.1$ and $\phi_p = -5$.

of the form:

$$\frac{\Gamma_i^U}{\Gamma_i^D} = \exp(Kv_d) \quad (\text{IV.13})$$

Inversion of Eq. (IV.13) gives the drift velocity as:

$$v_d = \frac{1}{K} \ln\left(\frac{\Gamma_i^U}{\Gamma_i^D}\right) \quad (\text{IV.14})$$

In order to find the constant K in the non magnetized case, Hutchinson [2] fitted the angular current collected by a spherical probe at $\bar{\lambda}_{De} = 0$ and $\bar{T}_i = 1$ to:

$$\Gamma_i(v_d, \cos \theta) = \Gamma_i^{v_d=0} [1/2v_d((1 - \cos \theta)K_u - (1 + \cos \theta)K_d)] \quad (\text{IV.15})$$

with $\Gamma_i^{v_d=0} = 1.56\Gamma_i^0$, $K_u = 0.64$, $K_d = 0.70$, yielding $K = K_u + K_d = 1.34$.

Fig. (IV-11) shows the angular distribution of the ion flux for $\bar{T}_i = 1$ and $\bar{T}_i = 0.1$ at subthermal and suprathermal velocities. Because the magnetic field impedes the downstream ion focusing, the coefficient K grows with β .

At high velocities, the magnetic field is not perceptible for $\bar{T}_i = 1$. At $\bar{T}_i = 0.1$ and $\beta = 0$, the angular distribution of the ion flux is non monotonic due to ion focusing, but because $\bar{\lambda}_{De} = 0$, this effect is not strong enough to cause reversal of the flux

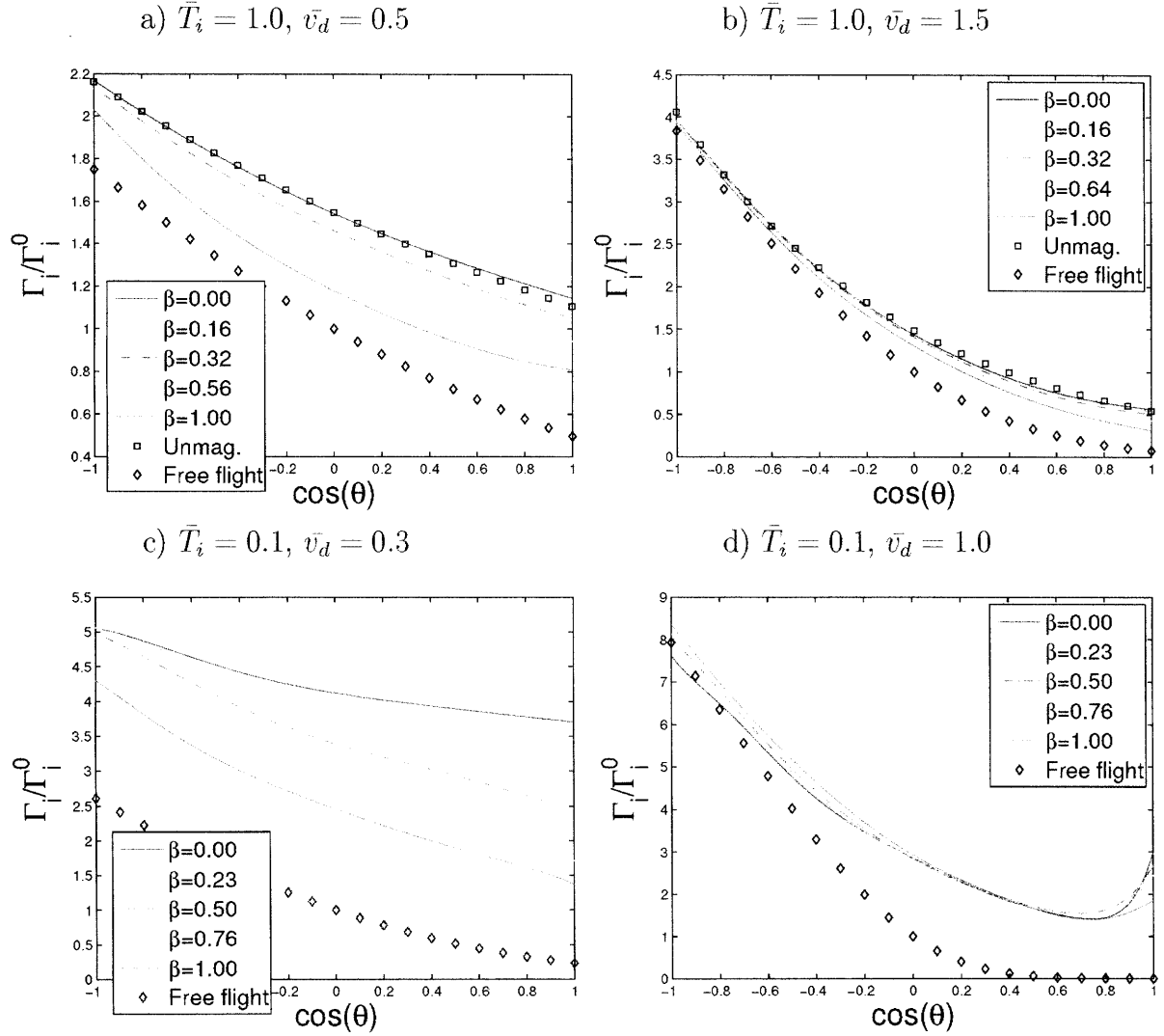


Figure IV-11: Angular distribution of the ion flux as a function of β at subthermal and suprathermal velocities in the quasineutral regime, for $\bar{T}_i = 1.0$ and $\bar{T}_i = 0.1$. Also plotted are the unmagnetized fittings at $\bar{T}_i = 1.0$ (Eq. (IV.15)), and the free flight solution (Eq. (I.15)).

asymmetry. The magnetic field reduces the focusing, but at $\beta = 1$ the downstream current is still more than 1000 times larger than the free flight value, implying that the downstream current comes from upstream. This point is important from the computational point of view. Indeed at high flow velocities the plasma is hardly perturbed upstream, hence the potential at $\cos\theta = -1$ tends to a value close to zero: our approximation of reinjecting the ions as an unperturbed Maxwellian regardless of the potential at the outer boundary becomes asymptotically exact as v_a rises. Since as mentioned in Section III.1 the potential well felt by the ions depends on $\chi = -\phi \frac{ZT_e}{T_i}$, it is no surprise if the curves at $\bar{T}_i = 1$ are closer to the free flight model.

Calibrating Mach-probes at low temperature appears problematic because of this focusing effect, we will therefore concentrate on the $\bar{T}_i = 1$ case. Fig. (IV-12) shows that K is not simply a function of β , but also of \bar{v}_a . For $\beta = 0$, K has a value within 10% of 1.34 as predicted by Hutchinson calibration. K is a growing function of β , having a larger slope at low velocities, confirming the conclusions drawn from Fig. (IV-11). Fig. (IV-12) also shows the calibration factor derived by Hutchinson for the strongly magnetized case assuming $l \gg L$ in the collisional presheath [7] (See Section I.5.5 for a summary of the theory). Unless the drift velocity is highly supersonic, we notice that our computed value of K rises higher than Hutchinson's limit near $\beta \simeq 1$. This feature is unlikely to depend on our assumption $l \simeq L$ in the collisional presheath since for example at $\bar{v}_a = 1$ we would find that the potential upstream tends to 0 within the collisionless presheath. Since the current collected downstream also comes from upstream, collisionality does not influence this result. The most plausible hypothesis is that K is not a monotonic function of β , but peaks somewhere around $\beta = 1$, and drops afterwards. The asymptotic value at $\beta \gg 1$ would then depend on the collisional hypothesis on the perturbation downstream, as in this limit the upstream and downstream sides of the probe are separated. A collisional treatment of the full magnetized presheath problem is required to find this limit.

Fig. (IV-12) also shows the Mach-probe calibration factor in the form of contour lines. Good calibration properties require vertical lines in order for K to be inde-

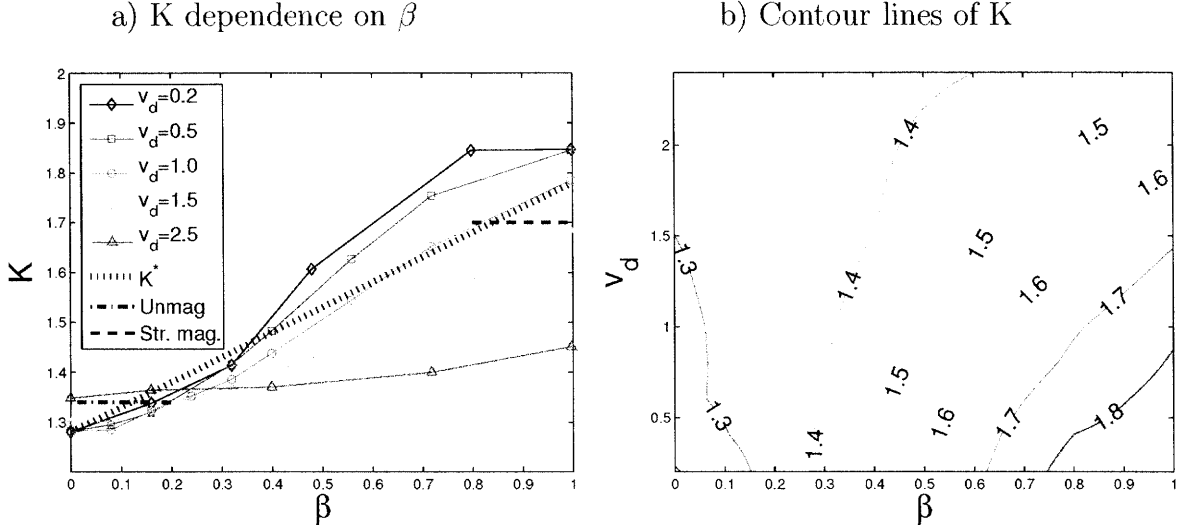


Figure IV-12: Mach-probe calibration factor for $\bar{T}_i = 1.0$ and $\bar{\lambda}_{De} = 0$. Fig. a shows the data (as well as the unmagnetized and strongly magnetized values calculated by Hutchinson, respectively $K = 1.34$ and $K = 1.7$) under the form $K = f(\beta)$. Fig. b shows the same data under the form of contour lines. Good calibration properties require vertical lines.

pendent of v_d in the presence of a given magnetic field. We see that for $\beta \lesssim 0.3$, the contour lines are almost vertical and rather spaced. Hence Hutchinson's calibration factor can be applied for $\beta \lesssim 0.3$ and arbitrary reasonable drift velocity.

Since in typical experiments flux-ratio measurements can have uncertainties up to 30%, we can safely use the following expression, valid for $0 < v_d < 1.5$ and $\beta_i \leq 1$ to within 10% (See Fig. (IV-12)):

$$K^*(\bar{T}_i = 1, \bar{\lambda}_{De} = 0, \beta) = 1.28 + 0.50\beta \quad (\text{IV.16})$$

IV.4.2 Plasma with finite shielding and equithermal ions and electrons

In Figs (IV-13,IV-14) are shown flux density versus angle for $\beta \in [0 : 1]$, and respectively $\bar{\lambda}_{De} = 1.0$ and $\bar{\lambda}_{De} = 0.1$.

The key features of those plots are similar to what has been seen in Fig. (IV-11). The main effect of the magnetic field is to impede ion collection downstream. Because for low drifts ions come from both sides of the probe, the effect of a rising field is to

shift the whole flux-density curve down, while slightly increasing the magnitude of its slope. For higher drifts, the flux density upstream is hardly affected by β , and the angular flux density flattening present at $\cos\theta \sim 1$ is progressively removed.

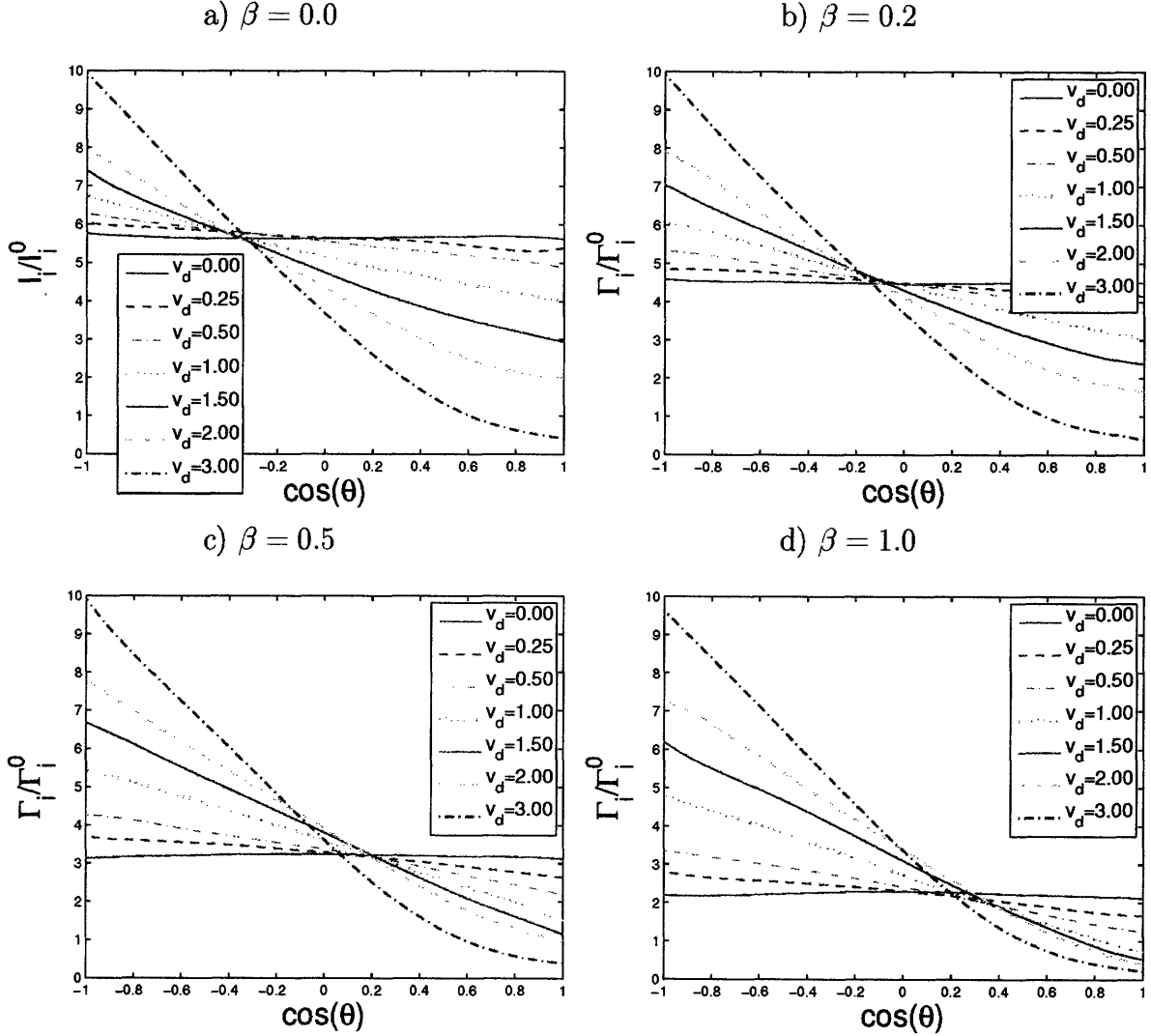


Figure IV-13: Angular distribution of the ion flux density to the probe for $\phi_p = -5$, $\bar{\lambda}_{De} = 1.0$, and a wide range of drift velocities ($\bar{v}_d \in [0 : 3]$) and magnetic field strengths ($\beta \in [0 : 1]$).

The flux ratio as defined by Eq. (IV.13) is therefore expected to be a rising function of β as in the quasineutral regime. This is confirmed by SCEPTIC computations as shown in Fig. (IV-15).

For $\beta \sim 0$, the calibration factor K is similar for $\bar{\lambda}_{De} = 1.0$ and $\bar{\lambda}_{De} = 0.1$, well below the $\bar{\lambda}_{De} = 0$ value. The physical reason is that downstream focusing is much

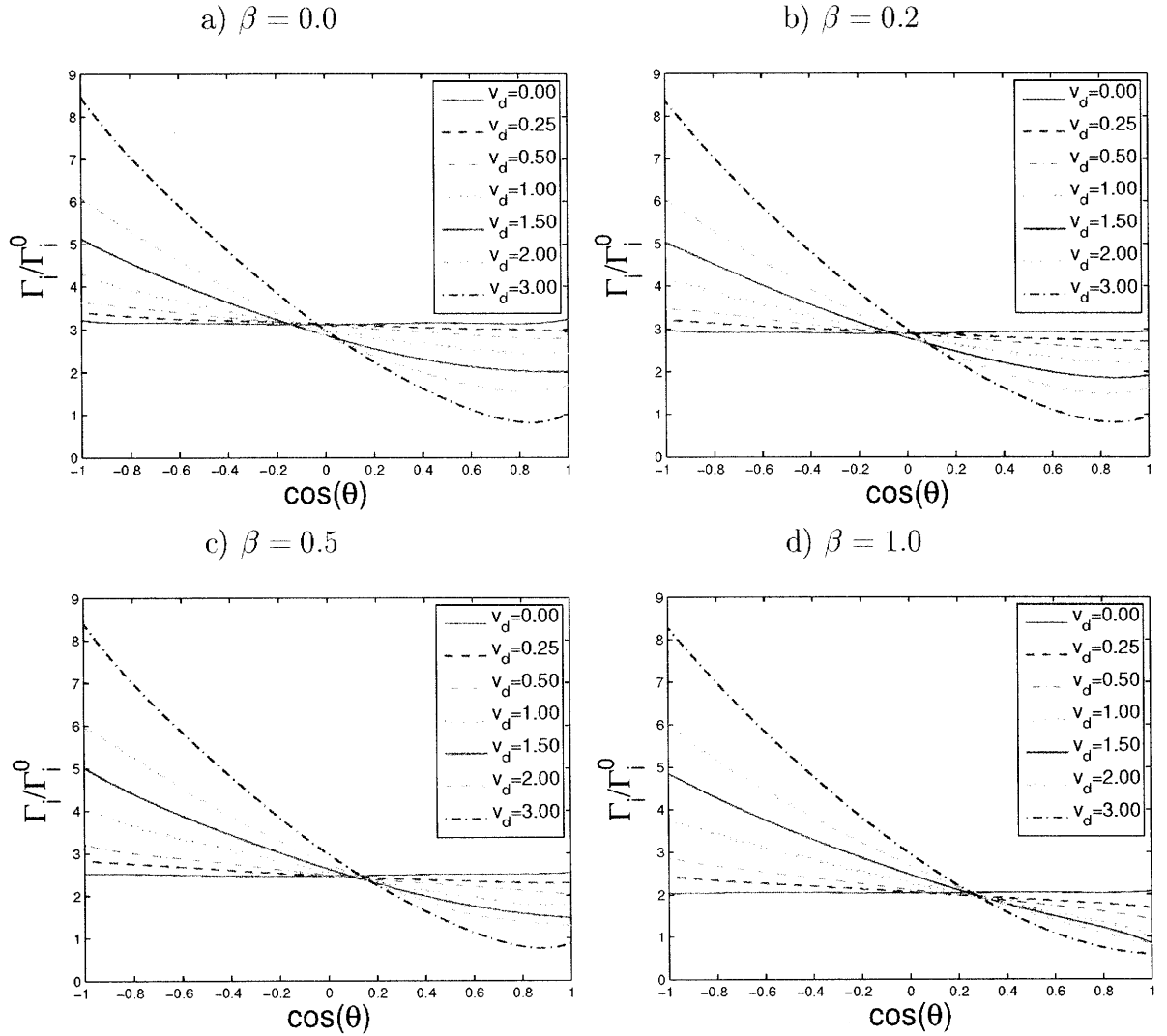


Figure IV-14: Angular distribution of the ion flux density to the probe for $\phi_p = -5$, $\bar{\lambda}_{De} = 0.1$, and a wide range of drift velocities ($\bar{v}_d \in [0 : 3]$) and magnetic field strengths ($\beta \in [0 : 1]$).

weaker in the quasineutral regime.

On the other hand for $\beta \sim 1$, similarities in K exist between the case $\bar{\lambda}_{De} = 0$ and $\bar{\lambda}_{De} = 1.0$, while flux ratios are much lower for $\bar{\lambda}_{De} = 0.1$. The physical interpretation is as follows. At $\bar{\lambda}_{De} = 0.1$, the radial extension of the probe potential perturbation is shorter than at $\bar{\lambda}_{De} = 1.0$. This implies that the maximum impact parameter is smaller, resulting in a narrower depletion cone in the presence of a background magnetic field (See Fig. (IV-3)). This directly results in a reduced flux-ratio. When $\bar{\lambda}_{De}$ is further decreased however, the total collected current drops significantly over the whole sphere, helping the flux ratio to increase.

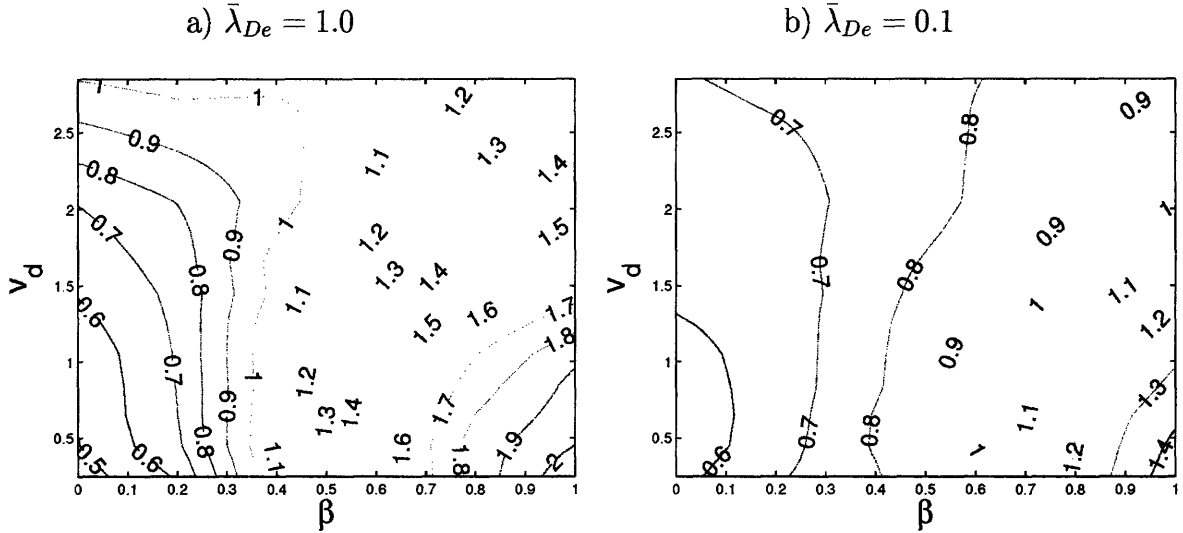


Figure IV-15: Mach-probe calibration factor contour lines for $\bar{\lambda}_{De} = 1.0$ and $\bar{\lambda}_{De} = 0.1$ at $\bar{T}_i = 1.0$ and $\phi_p = -5$.

Fig. (IV-15) shows that for moderate drift velocities the calibration factor is approximately independent of the drift velocity at a given β . Expressions for K valid to within 10% for $\bar{v}_d \leq 1.5$ are given by (See Fig. (IV-16)):

$$K^*(\bar{T}_i = 1, \bar{\lambda}_{De} = 1.0, \beta) = 0.55 + 1.36\beta \quad (\text{IV.17})$$

$$K^*(\bar{T}_i = 1, \bar{\lambda}_{De} = 0.1, \beta) = 0.55 + 0.78\beta \quad (\text{IV.18})$$

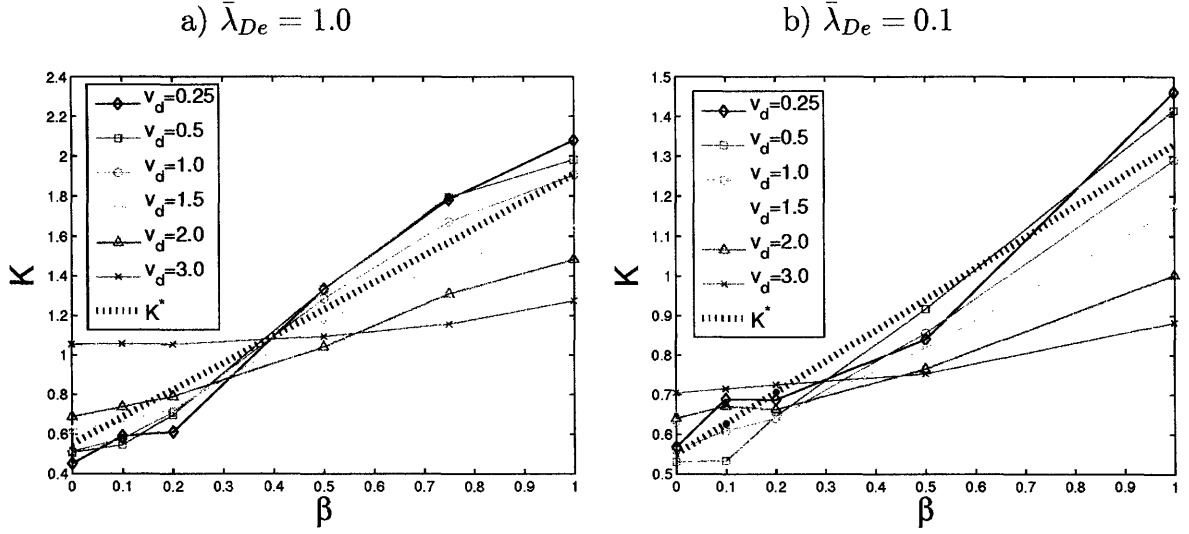


Figure IV-16: Mach-probe calibration factor as a function of β for $\bar{\lambda}_{De} = 1.0$ and $\bar{\lambda}_{De} = 0.1$ at $\bar{T}_i = 1.0$ and $\phi_p = -5$. Also shown as dotted lines are the fittings of Eqs (IV.17,IV.18).

IV.5 Flux asymmetry reversal suppression for strongly focusing probes

Ion collection asymmetry reversal, already discussed in Section IV.1, requires strongly focusing conditions, which for reasonable probe potentials this implies low ion temperature.

Fig. (IV-17) shows the evolution of the angular distribution of collected current for different magnetic field strengths and drift velocities for $\phi_p = -3$, $\bar{T}_i = 0.1$ and $\bar{\lambda}_{De} = 1$. The overall effect of raising the magnetic field strength is, as expected, to reduce the total ion current. As for the $\bar{T}_i = \bar{T}_e$ case, the flux ratio increases with β ; however because at $\beta = 0$ we start with a negative $K = \ln(\Gamma_i^U/\Gamma_i^D)$, and the flux-ratio contour lines differ sensibly from those in Fig. (IV-15).

This is shown in Fig. (IV-18). At low β , K is negative, and rapidly grows with the magnetic field. In no (weak) magnetic-field regime however are the contour lines vertical, implying that calibrating a mach probe under the form of Eq. (IV.13) in a weakly magnetized plasma is hardly feasible if ZT_i is substantially lower than T_e .

When the ion temperature is further decreased, we can approach the regime where

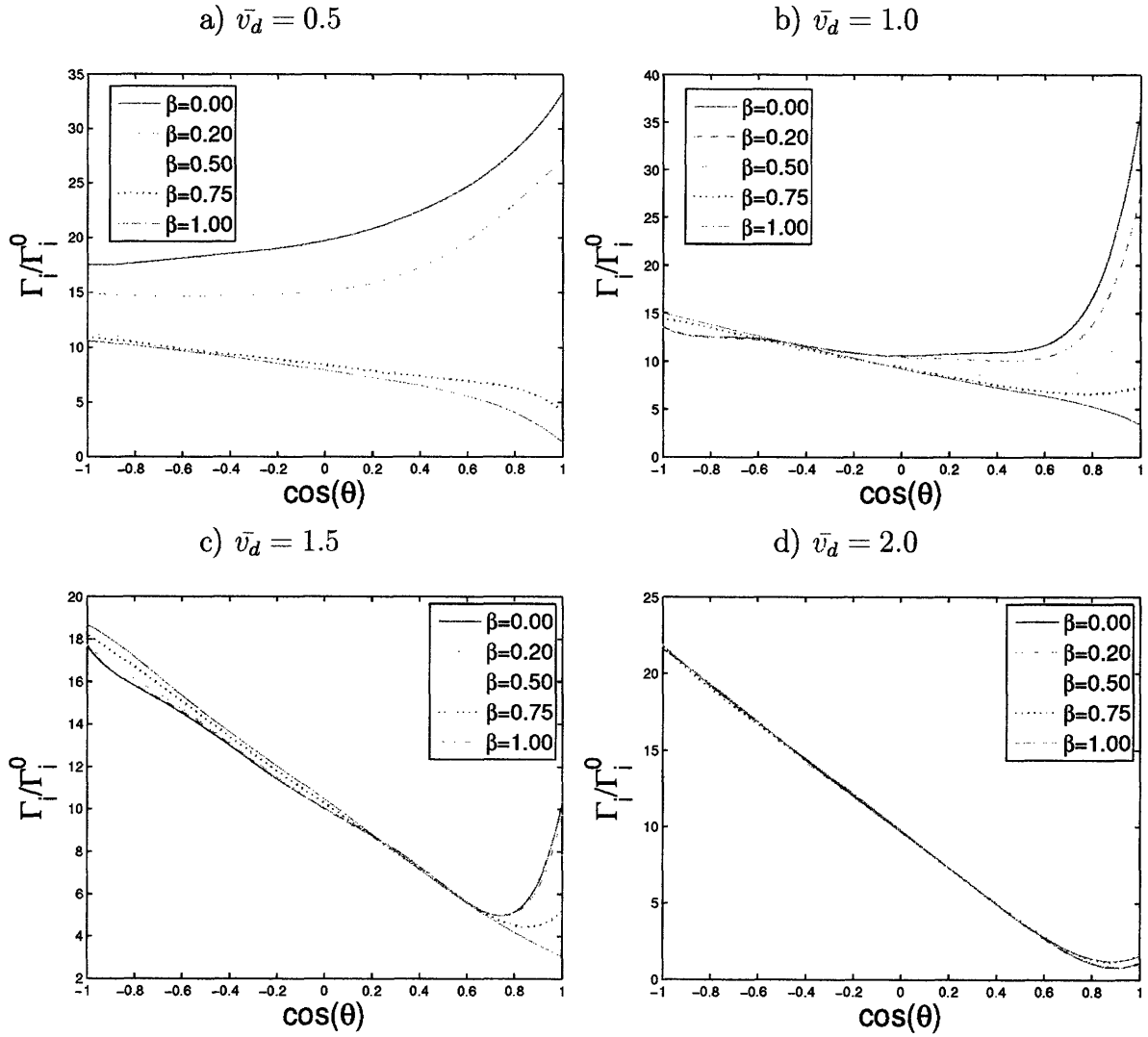


Figure IV-17: Angular distribution of the ion flux density to the probe for $\phi_p = -3$, $T_i = 0.1$, $\bar{\lambda}_{De} = 1.0$, and a wide range of drift velocities ($\bar{v}_d \in [0.5 : 2]$) and magnetic field strengths ($\beta \in [0 : 1]$).

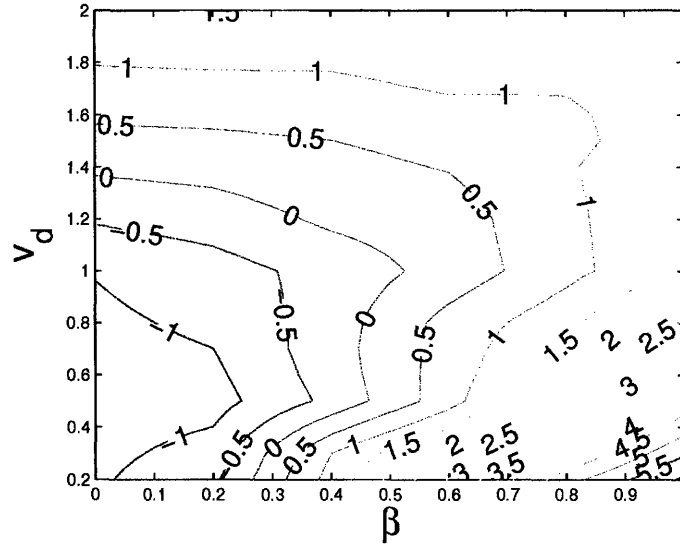


Figure IV-18: Mach-probe calibration factor contour lines for $\bar{T}_i = 0.1$ and $\bar{\lambda}_{De} = 1.0$, and $\phi_p = -3$. In no region are the lines vertical, hence calibrating a Mach-probe using Eq. (IV.13) at low ion temperature and weak magnetic field does not appear feasible.

the plasma can be considered as a cold beam provided v_d is high enough. The downstream region delimited by θ_{lim} (Eqs (IV.10,IV.11)) is therefore depleted, while the rest of the probe collects a comparable amount of current regardless of β .

This effect causes the angular ion flux-density distribution to peak at $\cos \theta \lesssim 1$, as shown on Fig. (IV-19). At $\bar{v}_d = 0.5$, the ratio of drift over thermal energy is not high enough for the ion flux-density distribution to peak at $\cos \theta \sim \cos \theta_{lim}$. When $\bar{v}_d = 1$, the ratio of drift over thermal energy is higher, and the peak is exactly at $\cos \theta = \cos \theta_{lim}$. The values of $\cos \theta_{lim}$, indicated by small vertical bars on the graphs, have been calculated using the total ion current computed by SCEPTIC. It is interesting to notice that depending on the drift velocity, raising the magnetic field displaces the peak at lower or higher angles. In practice electrodes have a finite width, and it is not obvious that this effect could be experimentally verified.

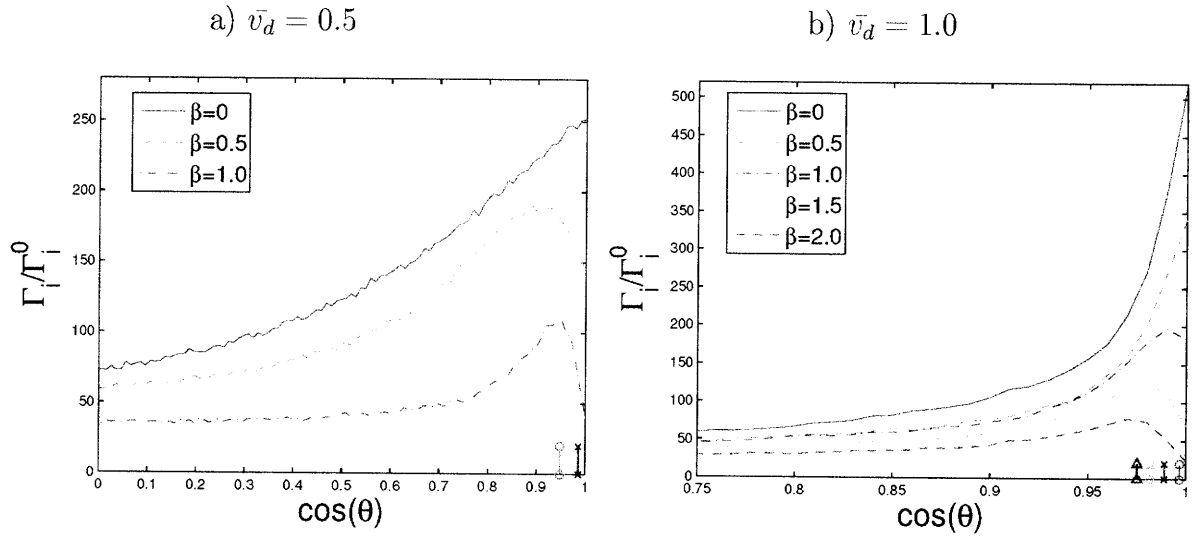


Figure IV-19: Angular distribution of the ion flux-density at $\bar{T}_i = 0.01$, $\phi_p = -3$ and $\bar{\lambda}_{De} = 1.0$ for $\bar{v}_d = 0.5$ and $\bar{v}_d = 1.0$, and various magnetic field strengths. Vertical bars indicate the angles θ_{lim} (Eqs (IV.10,IV.11)) corresponding to the curves. Circles: $\beta = 0.5$, Cross: $\beta = 1.0$, Squares: $\beta = 1.5$, Triangles: $\beta = 2.0$.

Chapter V

Conclusions

V.1 Review of our computation hypothesis

Perhaps the most difficult task in any quantitative analysis is to provide an estimate of the results accuracy. In the present case uncertainties arise from inherently numerical reasons, as well as from our choice of boundary conditions.

In theory numerical uncertainties are not an issue. By increasing the number of computational particles per Debye-cube, the noise on the charge-density distribution and the potential can be made arbitrarily small. By simultaneously reducing the ion orbit integrator time-step, the error on the ion trajectories, hence the ion current, becomes negligible. In preceding SCEPTIC publications [2, 3] as well as in this thesis, the number of computational particles and the orbit-integrator time-step are chosen in order for the computation to be 1% accurate or more.

Provided the computational domain is large enough, the potential boundary condition has been shown not to be a cause of uncertainties. Indeed in the quasineutral regime we do not solve for the potential, and in the limit of zero collisionality it is exact to assume $\partial/\partial z = 0$ on the collisionless presheath scale length: This is the condition we use to solve Poisson equation when when plasma shielding is finite.

The real challenge is to estimate the error introduced by assuming that momentum loss in the non-collisionless presheath can be modeled by reinjecting the unperturbed ion distribution function at the outer boundary, regardless of the potential there. A

simple *a posteriori* estimate of the error bound on the total ion current is given by:

$$\frac{|\Delta I_i|}{I_i} \leq \frac{\langle \phi_b \rangle}{\tilde{\phi}_p} \quad (\text{V.1})$$

where $\langle \phi_b \rangle$ is the average potential seen (but not felt) by collection ions when they enter the computational domain, and $\tilde{\phi}_p$ the “effective” probe potential felt by the ions, that is to say $\tilde{\phi}_p = \phi_p$ if $\bar{\lambda}_{De} \gg 1$ and $\tilde{\phi}_p = \phi_s$ if $\bar{\lambda}_{De} \ll 1$. Because a typical sheath entrance potential is $\phi_s \sim -1$, and $|\langle \phi_b \rangle|$ is maximal in the flow-free case, higher error bounds are found in the regime $\bar{v}_d = 0$ and $\bar{\lambda}_{De} = 0$. A typical worse case is therefore given by the parameters of Fig. (III-3b), i.e. $\bar{v}_d = 0$, $\bar{\lambda}_{De} = 0$, $\bar{T}_i = 0.3$ and $\beta = 1$. Because in this case SCEPTIC computes $I_i = 1.77I_i^0$ (See Fig. (III-8)), a crude approximation to $\langle \phi_b \rangle$ is $\langle \phi_b \rangle = \phi_b(\rho = r_p\sqrt{1.77}) \sim -0.2$. The error bound is therefore on the order of 20%.

This value of 20% is high, but it is only a guarantee that the error can not be higher. Because we heuristically modeled the non-collisionless presheath dynamics, the result computed by SCEPTIC might be much closer to the reality. In addition we considered the worse possible regime. By taking $\beta < 1$, $\bar{\lambda}_{De} \neq 0$ or $\bar{v}_d \neq 0$, the error bound quickly goes to 0.

V.2 Implications of our results

Several results presented in this thesis are relevant to dusty plasma physics, and flux-collecting probes operation.

We proved, within the free flight approximation, that the ion current dependence on the magnetic field is linear in β (the ratio of probe radius over a mean ion gyroradius) for $\beta \ll 1$. Furthermore numerical investigation clearly indicates that this property is valid for an arbitrary probe potential. This result is in contradiction with the statement of Rubinstein and Laframboise [11], and implies that the magnetic field effect on ion collection is non negligible even for small β .

Mach-probe calibration factors independent of the drift velocity have been pro-

vided when $T_i = ZT_e$ for $\lambda_{De} = 0$, $\lambda_{De} = 0.1r_p$ and $\lambda_{De} = r_p$, covering the typical regimes of Mach-probes operation. Although in the strongly magnetized regime Mach-probes can easily be calibrated even at low ion temperature [7], ion focusing causes this task to be more difficult when $\beta \lesssim 1$.

V.3 Suggestions for future work

This thesis leaves many questions unanswered, and several paths for future investigation exist. One route would be to solve the potential on a three-dimensional mesh in order to assess the effect of turbulence, and to be able to study regimes where the flow is not parallel to the magnetic field. Also of major importance would be to resolve the whole non-collisionless presheath in order to bridge the gap between $\beta \sim 1$ and $\beta = \infty$.

However those undertakings require deep modifications of SCEPTIC. There is perhaps more straightforward yet interesting physics to be done with the present code. The two next steps will be to compute the ion drag force in the weakly magnetized regime (See Ref. [26] for an explanation of the procedure when $\beta = 0$), and to investigate the influence of ion charge-exchange collisions on the collection current (The reader is referred to Ref. [27] for a description of the implementation of charge-exchange collisions in SCEPTIC).

Appendix A

Low β expansion of Whipple-like integrals

A.1 Sphere at space potential in a drifting plasma

The current drawn by a spherical probe at space potential from a drifting Maxwellian is given by Eqs (I.21,I.25), that we repeat here for convenience under the following form using the notation $\iota = I_i/I_i^0$:

$$\iota(\beta, v_d) = \iota^{in}(\beta, v_d) + \iota^{out}(\beta, v_d) \quad (\text{A.1})$$

with

$$\iota^{in}(\beta, v_d) = \frac{1}{4}\pi^2\beta^4 \int_{s=0}^{\infty} \int_{t=0}^{\infty} \tilde{f}(\beta, v_d, s, t) \frac{1}{2}\theta(1-s)(1-s)^2 st dt ds \quad (\text{A.2})$$

and

$$\iota^{out}(\beta, v_d) = \frac{1}{4}\pi^2\beta^4 \int_{s=0}^{\infty} \int_{t=0}^{\infty} \tilde{f}(\beta, v_d, s, t) \int_{u=|s-1|}^{s+1} \frac{1}{2\pi} \int_{\psi=0}^{2\pi} \text{H}(u, s, t, \psi) u du st dt ds \quad (\text{A.3})$$

We recall that

$$\tilde{f}(\beta, v_d, s, t) = \frac{1}{2} \left[\exp\left(-\frac{\pi}{4}\beta^2\left(s^2 + \left(t - \frac{v_d}{v_{ti}} \frac{2}{\beta\sqrt{\pi}}\right)^2\right)\right) + \exp\left(-\frac{\pi}{4}\beta^2\left(s^2 + \left(t + \frac{v_d}{v_{ti}} \frac{2}{\beta\sqrt{\pi}}\right)^2\right)\right) \right] \quad (\text{A.4})$$

In the rest of this section, ι is implicitly assumed to be a function of β and v_d , so that “ (β, v_d) ” can be dropped.

A.1.1 Current drawn from orbits in the magnetic shadow:

ι^{in}

Eq. (A.2) counts the orbits with $s+u < 1$, that we know for sure are collection orbits. The contribution of those orbits to the total current is of order β^2 , as can be seen by directly evaluating the integral:

$$\begin{aligned} \iota^{in} &= \frac{1}{4}\pi^2\beta^4 \int_{s=0}^{\infty} \int_{t=0}^{\infty} \tilde{f}(\beta, v_d, s, t) \\ &\quad \exp\left(-\frac{\pi}{4}\beta^2(s^2 + t^2)\right) \frac{1}{2}\theta(1-s)(1-s)^2 st dt ds \end{aligned} \quad (\text{A.5})$$

$$\begin{aligned} &= \frac{1}{4}\pi^2\beta^4 \left[\sqrt{\pi} \frac{v_d}{v_{ti}} \operatorname{erf}\left(\frac{v_d}{v_{ti}}\right) + \exp\left(-\frac{v_d^2}{v_{ti}^2}\right) \right] \\ &\quad \left[-\frac{4\operatorname{erf}\left(\frac{1}{2}\beta\sqrt{\pi}\right)}{\pi^2\beta^5} - \frac{8\exp\left(-\frac{1}{4}\pi\beta^2\right)}{\pi^3\beta^6} + \frac{2}{\pi^2\beta^4} + \frac{8}{\pi^3\beta^6} \right] \end{aligned} \quad (\text{A.6})$$

$$= \pi \left[\sqrt{\pi} \frac{v_d}{v_{ti}} \operatorname{erf}\left(\frac{v_d}{v_{ti}}\right) + \exp\left(-\frac{v_d^2}{v_{ti}^2}\right) \right] \frac{\beta^2}{48} + O(\beta^4) \quad (\text{A.7})$$

A.1.2 Current drawn from the other orbits: ι^{out}

Eq. (A.3) counts the current collected from the orbits with $s+u \geq 1$ and $|u-s| \leq 1$. That is to say helices part in the magnetic shadow and part outside. $H(u, s, t, \psi)$ is an impact factor equal to 1 if the orbit characterized by (u, s, t, ψ) intersects the sphere at least once, and 0 otherwise.

$\frac{1}{2\pi} \int_{\psi=0}^{2\pi} H(u, s, t, \psi) d\psi$ can be replaced by $\min(1, \frac{t^*(s,t,u)}{t})$. The significance of t^* is as follows: If $t < t^*(s, t, u)$, the orbits characterized by (s, t, u) cross the sphere at least once regardless of ψ . If $t \geq t^*(s, t, u)$, orbits do not cross the sphere or cross it only once depending on ψ .

$$\iota^{out} = \frac{1}{4}\pi^2\beta^4 \int_{s=0}^{\infty} \int_{t=0}^{\infty} \tilde{f}(\beta, v_d, s, t) \int_{u=|s-1|}^{s+1} \min(1, \frac{t^*(s, t, u)}{t}) u d u s t d s d t \quad (\text{A.8})$$

$$\begin{aligned} &= \frac{1}{4}\pi^2\beta^4 \int_{s=0}^{\infty} \int_{u=|s-1|}^{s+1} \left[\int_{t=0}^{\tilde{t}(s, u)} \tilde{f}(\beta, v_d, s, t) (t - t^*(s, t, u)) d t \right. \\ &\quad \left. + \int_{t=0}^{\infty} \tilde{f}(\beta, v_d, s, t) t^*(s, t, u) d t \right] u d u s d s \end{aligned} \quad (\text{A.9})$$

where $\tilde{t}(s, u)$ is defined by $t^*(s, \tilde{t}(s, u), u) = \tilde{t}(s, u)$

For convenience we now rewrite ι^{out} as:

$$\iota^{out}(\beta, v_d) = \iota_L^{out}(\beta, v_d) + \iota_C^{out}(\beta, v_d) \quad (\text{A.10})$$

with:

$$\begin{aligned} \iota_L^{out} &= \frac{1}{8}\pi^2\beta^4 \int_{s=0}^{\infty} \exp(-\frac{\pi}{4}\beta^2 s^2) s \int_{u=|s-1|}^{s+1} u \int_{t=0}^{\tilde{t}(s, u)} (t - t^*(s, t, u)) \\ &\quad \left[\exp(-\frac{\pi}{4}\beta^2 (t - \frac{v_d}{v_{ti}} \frac{2}{\beta\sqrt{\pi}})^2) + \exp(-\frac{\pi}{4}\beta^2 (t + \frac{v_d}{v_{ti}} \frac{2}{\beta\sqrt{\pi}})^2) \right] d s d u d t \end{aligned} \quad (\text{A.11})$$

and

$$\begin{aligned} \iota_C^{out} &= \frac{1}{8}\pi^2\beta^4 \int_{s=0}^{\infty} \exp(-\frac{\pi}{4}\beta^2 s^2) s \int_{u=|s-1|}^{s+1} u \int_{t=0}^{\infty} t^*(s, t, u) \\ &\quad \left[\exp(-\frac{\pi}{4}\beta^2 (t - \frac{v_d}{v_{ti}} \frac{2}{\beta\sqrt{\pi}})^2) + \exp(-\frac{\pi}{4}\beta^2 (t + \frac{v_d}{v_{ti}} \frac{2}{\beta\sqrt{\pi}})^2) \right] d s d u d t \end{aligned} \quad (\text{A.12})$$

A.1.3 Analysis of $t^*(s, t, u)$

In this section we implicitly assume that $u \in [|s-1|, s+1]$.

$t^*(s, t, u)$ has been calculated analytically in Ref. [11], and is given by:

$$t^*(s, t, u) = \frac{1}{\pi} \sqrt{-(s^2 + u^2 - 1 + 2t^2) + 2\sqrt{(s^2 + u^2 - 1)t^2 + t^4 + s^2u^2}} + \frac{t}{\pi} \arccos\left(\frac{-t^2 + \sqrt{(s^2 + u^2 - 1)t^2 + t^4 + s^2u^2}}{su}\right) \quad (\text{A.13})$$

This expression has a simple limit when $t \rightarrow 0$ with (s, u) fixed:

$$\lim_{t \rightarrow 0} t^*(s, t, u) = \frac{\sqrt{1 - (s - u)^2}}{\pi} + O(t^2) \quad (\text{A.14})$$

The physical meaning of Eq. (A.14) is as follows. An orbit characterized by $t \ll 1$ is, locally, a straight line perpendicular to the magnetic axis. Therefore $2\pi t^*(s, t, u)$ is simply the width of the unit sphere at $\rho = |s - u|$, i.e. $2 \cos(\arcsin(|s - u|)) = 2\sqrt{1 - (s - u)^2}$.

The expansion of $t^*(s, t, u)$ as $(s, u) \rightarrow \infty$ with t fixed can easily be calculated as well:

$$\lim_{(s, u) \rightarrow \infty} t^*(s, t, u) = \frac{\sqrt{1 - (s - u)^2}}{\pi} + \frac{1}{2\pi} \frac{t^2 \sqrt{1 - (s - u)^2}}{s^2} + O\left(\frac{1}{s^4}\right) \quad (\text{A.15})$$

We recall that $|s - u| \leq 1$, therefore when $(s, u) \rightarrow \infty$, $\frac{1}{s^2} \sim \frac{1}{su}$.

The equation $t^*(s, \tilde{t}(s, u), u) = \tilde{t}(s, u)$ can not be analytically solved for $\tilde{t}(s, u)$, however we have the following property, that can be easily shown from the symmetry $t^*(s, t, u) = t^*(u, t, s)$:

$$\forall (s, u) : \tilde{t}(s, u) \leq \tilde{t}(s, s) \leq \tilde{t}\left(\frac{1}{2}, \frac{1}{2}\right) \quad (\text{A.16})$$

We have, for example, $\tilde{t}\left(\frac{1}{2}, \frac{1}{2}\right) = \frac{1}{2}$ and $\tilde{t}(1, 1) \simeq 0.336$. An expansion for $\tilde{t}(s, u)$ as $(s, u) \rightarrow \infty$ can be calculated using Eq. (A.15) :

$$\lim_{(s, u) \rightarrow \infty} \tilde{t}(s, u) = \frac{\sqrt{1 - (s - u)^2}}{\pi} + \frac{(1 - (s - u)^2)^{3/2}}{2\pi^3 s^2} + O\left(\frac{1}{s^4}\right) \quad (\text{A.17})$$

When $t \rightarrow \infty$ with (s, u) fixed we have:

$$\lim_{t \rightarrow \infty} t^*(s, t, u) = \arccos\left(\frac{s^2 + u^2 - 1}{2su}\right) \frac{t}{\pi} + O\left(\frac{1}{t}\right) \quad (\text{A.18})$$

If we then let $(s, u) \rightarrow \infty$, we get:

$$\lim_{(s,u) \rightarrow \infty | t \gg (s,u)} t^*(s, t, u) = \sqrt{\frac{1 - (s-u)^2}{su}} \frac{t}{\pi} + O\left(\frac{1}{t}\right) \quad (\text{A.19})$$

If $(s, t, u) \gg 1$, and we make the assumption $t \ll s^2$ (That is to say t and s have the same magnitude), we can expand $t^*(s, t, s)$ with $\alpha = \frac{t}{s} \ll s$ and obtain:

$$\begin{aligned} \lim_{(s,u) \gg 1 | \alpha \ll s} t^*(s, \alpha s, u) &= \frac{\sqrt{\alpha^2 + 1} \sqrt{1 - (s-u)^2}}{\pi} \\ &+ \frac{1}{2\pi} \frac{\alpha^2 (s-u) \sqrt{1 - (s-u)^2}}{s \sqrt{1 + \alpha^2}} + O\left(\frac{1}{s^2}\right) \end{aligned} \quad (\text{A.20})$$

A.1.4 Analysis of t_L^{out}

We have seen that $\tilde{t}(s, u) \leq \frac{1}{2}$, therefore the t integral is over a compact (i.e. $[0, \tilde{t}(s, u)]$), and we can Taylor expand $\exp(-\frac{\pi}{4} \beta^2 (t \pm \frac{v_d}{v_{ti}} \frac{2}{\beta \sqrt{\pi}})^2)$ for low β inside the t integral.

Because of the term $\exp(-\frac{\pi}{4} \beta^2 s^2)$, when $\beta \rightarrow 0$ the s integral is determined by the value of the integrand at large s . It is therefore appropriate to use the asymptotic values of t^* given by Eq. (A.15) and \tilde{t} given by Eq. (A.17). For the same reason we replace $|s - 1|$ by $s - 1$.

$$\begin{aligned}
\iota_L^{out} &= \frac{1}{4}\pi^2\beta^4 \int_{s=0}^{\infty} \exp(-\frac{\pi}{4}\beta^2 s^2) s \int_{u=s-1}^{s+1} u \int_{t=0}^{\frac{\sqrt{1-(s-u)^2}}{\pi} + O(\frac{1}{s^2})} \left[\exp(-\frac{v_d^2}{v_{ti}^2}) + O(\beta) \right] \\
&\quad \left[t - \sqrt{1-(s-u)^2} \left(\frac{1}{\pi} + O(\frac{1}{s^2}) \right) \right] dt du ds + O(\beta^3) \tag{A.21}
\end{aligned}$$

$$\begin{aligned}
&= \frac{1}{4}\pi^2\beta^4 \int_{s=0}^{\infty} \exp(-\frac{\pi}{4}\beta^2 s^2) s \int_{u=s-1}^{s+1} u \\
&\quad \int_{t=0}^{\frac{\sqrt{1-(s-u)^2}}{\pi}} \exp(-\frac{v_d^2}{v_{ti}^2}) \left[t - \frac{\sqrt{1-(s-u)^2}}{\pi} \right] dt du ds + O(\beta^2) \tag{A.22}
\end{aligned}$$

$$\begin{aligned}
&= \frac{1}{4}\pi^2\beta^4 \exp(-\frac{v_d^2}{v_{ti}^2}) \int_{s=0}^{\infty} \exp(-\frac{\pi}{4}\beta^2 s^2) s \\
&\quad \int_{u=s-1}^{s+1} u \left[-\frac{1}{2} \frac{1-(s-u)^2}{\pi^2} \right] du ds + O(\beta^2) \tag{A.23}
\end{aligned}$$

$$= -\frac{1}{4}\pi^2\beta^4 \exp(-\frac{v_d^2}{v_{ti}^2}) \int_{s=0}^{\infty} \exp(-\frac{\pi}{4}\beta^2 s^2) \frac{2}{3} \frac{s^2}{\pi^2} ds + O(\beta^2) \tag{A.24}$$

$$= -\exp(-\frac{v_d^2}{v_{ti}^2}) \frac{\beta}{3\pi} + O(\beta^2) \tag{A.25}$$

A.1.5 Analysis of ι_C^{out}

Let us rewrite ι_C^{out} as:

$$\begin{aligned}
\iota_C^{out} &= \frac{1}{8}\pi^2\beta^4 \int_{s=0}^{\infty} \exp(-\frac{\pi}{4}\beta^2 s^2) s \int_{t=0}^{\infty} \left[\exp(-\frac{\pi}{4}\beta^2 (t - \frac{v_d}{v_{ti}} \frac{2}{\beta\sqrt{\pi}})^2) \right. \\
&\quad \left. + \exp(-\frac{\pi}{4}\beta^2 (t + \frac{v_d}{v_{ti}} \frac{2}{\beta\sqrt{\pi}})^2) \right] \int_{u=s-1}^{s+1} t^*(s, t, u) u du ds dt \tag{A.26}
\end{aligned}$$

We are interested in the whole range of $\alpha = \frac{t}{s}$. However when $\beta \rightarrow 0$ the weight of the triple integral is given by the value of the integrand for $(s, t, u) \gg 1$. We can use the following change of variables:

$$\begin{pmatrix} t \\ s \end{pmatrix} \rightarrow \begin{pmatrix} \alpha = \frac{t}{s} \\ s \end{pmatrix} \tag{A.27}$$

The Jacobian of the transformation is $J = s$, we therefore have $dt ds = s d\alpha ds$.

In order to get the first terms of the taylor expansion of the whole triple integral at low β , we can replace $t^*(s, t, u)$ by its asymptotic expansion at high s , but without making any assumption on α (Eq. (A.20)).

$$\int_{u=s-1}^{s+1} t^*(s, \alpha s, u) u du = \frac{\sqrt{\alpha^2 + 1}}{\pi} \int_{u=s-1}^{s+1} \sqrt{1 - (s-u)^2} u du + \frac{\alpha^2}{2\pi\sqrt{\alpha^2 + 1}} \int_{u=s-1}^{s+1} \frac{s-u}{s} \sqrt{1 - (s-u)^2} u du \quad (\text{A.28})$$

$$= \frac{s\sqrt{\alpha^2 + 1}}{2} - \frac{\alpha^2}{16s\sqrt{\alpha^2 + 1}} + O\left(\frac{1}{s^2}\right) \quad (\text{A.29})$$

$$= \frac{s\sqrt{\alpha^2 + 1}}{2} + O\left(\frac{1}{s}\right) \quad (\text{A.30})$$

$$(\text{A.31})$$

We can now rewrite ι_C^{out} as:

$$\begin{aligned} \iota_C^{out} &= \frac{1}{8}\pi^2\beta^4 \int_{s=0}^{\infty} \exp\left(-\frac{\pi}{4}\beta^2 s^2\right) s \int_{\alpha=0}^{\infty} \left[\exp\left(-\frac{\pi}{4}\beta^2\left(\alpha s - \frac{v_d}{v_{ti}} \frac{2}{\beta\sqrt{\pi}}\right)^2\right) \right. \\ &\quad \left. + \exp\left(-\frac{\pi}{4}\beta^2\left(\alpha s + \frac{v_d}{v_{ti}} \frac{2}{\beta\sqrt{\pi}}\right)^2\right) \right] s \frac{\sqrt{\alpha^2 + 1}}{2} s d\alpha ds + O(\beta^2) \end{aligned} \quad (\text{A.32})$$

$$\begin{aligned} &= \frac{1}{16}\pi^2\beta^4 \int_{\alpha=0}^{\infty} \sqrt{\alpha^2 + 1} \int_{s=0}^{\infty} \left[\exp\left(-\frac{\pi}{4}\beta^2\left(s^2 + \left(\alpha s - \frac{v_d}{v_{ti}} \frac{2}{\beta\sqrt{\pi}}\right)^2\right)\right) \right. \\ &\quad \left. + \exp\left(-\frac{\pi}{4}\beta^2\left(s^2 + \left(\alpha s + \frac{v_d}{v_{ti}} \frac{2}{\beta\sqrt{\pi}}\right)^2\right)\right) \right] s^3 ds d\alpha + O(\beta^2) \end{aligned} \quad (\text{A.33})$$

$$\begin{aligned} &= \frac{1}{2} \int_{\alpha=0}^{\infty} \frac{1}{(1 + \alpha^2)^3} \left[(2\alpha^3 \frac{v_d^3}{v_{ti}^3} + 3\alpha^3 \frac{v_d}{v_{ti}} + 3\alpha \frac{v_d}{v_{ti}}) \sqrt{\pi} \operatorname{erf}\left(\frac{\alpha v_d / v_{ti}}{\sqrt{1 + \alpha^2}}\right) \exp\left(-\frac{v_d^2 / v_{ti}^2}{1 + \alpha^2}\right) \right. \\ &\quad \left. + 2(\alpha^2 + \alpha^2 \frac{v_d^2}{v_{ti}^2} + 1) \sqrt{1 + \alpha^2} \exp\left(-\frac{v_d^2}{v_{ti}^2}\right) \right] d\alpha + O(\beta^2) \end{aligned} \quad (\text{A.34})$$

$$= \frac{1}{2} \exp\left(-\frac{v_d^2}{v_{ti}^2}\right) + \frac{\sqrt{\pi}}{2} \left(\frac{v_d}{v_{ti}} + \frac{v_{ti}}{2v_d}\right) \operatorname{erf}\left(\frac{v_d}{v_{ti}}\right) + O(\beta^2) \quad (\text{A.35})$$

A.1.6 Conclusion

Therefore, the total current to the probe is:

$$I_i/I_i^0 = \left[\frac{1}{2} \exp\left(-\frac{v_d^2}{v_{ti}^2}\right) + \frac{\sqrt{\pi}}{2} \left(\frac{v_d}{v_{ti}} + \frac{v_{ti}}{2v_d}\right) \operatorname{erf}\left(\frac{v_d}{v_{ti}}\right) \right] - \exp\left(-\frac{v_d^2}{v_{ti}^2}\right) \frac{\beta}{3\pi} + O(\beta^2) \quad (\text{A.36})$$

A.2 Charged sphere in a stationary plasma: Upper bound

The upper bound current drawn by a spherical probe with normalized potential χ_p from a stationary Maxwellian is given by Eqs (I.75,I.22) that we repeat here for convenience under the following form:

$$I^{Up}(\beta, \chi_p) = I_{in}^{Up}(\beta, \chi_p) + I_{out}^{Up}(\beta, \chi_p) \quad (\text{A.37})$$

with

$$I_{in}^{Up}(\beta, \chi_p) = \frac{\exp(\chi_p)}{4} \pi^2 \beta^4 \int_{s=0}^{\infty} \int_{t=0}^{\infty} \theta(s^2 + t^2 - D^2) \tilde{f}(\beta, s, t) \frac{1}{2} \theta(1-s)(1-s)^2 s t ds dt \quad (\text{A.38})$$

and

$$I_{out}^{Up}(\beta, \chi_p) = \frac{\exp(\chi_p)}{4} \pi^2 \beta^4 \int_{s=0}^{\infty} \int_{t=0}^{\infty} \theta(s^2 + t^2 - D^2) \tilde{f}(\beta, s, t) \int_{u=s-1}^{s+1} \frac{1}{2\pi} \int_{\psi=0}^{2\pi} \mathrm{H}(u, s, t, \psi) u du s t ds dt \quad (\text{A.39})$$

where

$$\tilde{f}(\beta, s, t) = \exp\left(-\frac{\pi}{4} \beta^2 (s^2 + t^2)\right) \quad (\text{A.40})$$

and

$$D = \frac{2}{\beta} \sqrt{\frac{\chi_p}{\pi}} \quad (\text{A.41})$$

A.2.1 Current drawn from the orbits in the magnetic shadow:

ι^{in}

The contribution to the upper bound current from the orbits with $s + u < 1$ is quadratic in β . Indeed using Eq. (A.7) we can write:

$$\iota_{in}^{Up} \leq \exp(\chi_p) \iota^{in}(\beta, 0) \quad (\text{A.42})$$

$$\leq \exp(\chi_p) \frac{\pi \beta^2}{48} \quad (\text{A.43})$$

A.2.2 Current drawn from the other orbits: ι^{out}

For convenience, we rewrite ι_{out}^{Up} as:

$$\iota_{out}^{Up}(\beta, \chi_p) = \iota_L^{Up}(\beta, \chi_p) + \iota_C^{Up}(\beta, \chi_p) \quad (\text{A.44})$$

with:

$$\begin{aligned} \iota_L^{Up} = & \frac{\exp(\chi_p)}{4} \pi^2 \beta^4 \int_{s=0}^{\infty} \exp(-\frac{\pi}{4} \beta^2 s^2) s \int_{u=s-1}^{s+1} u \\ & \int_{t=0}^{\tilde{t}(s,u)} \theta(s^2 + t^2 - D^2) (t - t^*(s, t, u)) \exp(-\frac{\pi}{4} \beta^2 t^2) ds du dt \end{aligned} \quad (\text{A.45})$$

and

$$\begin{aligned} \iota_C^{Up} = & \frac{\exp(\chi_p)}{4} \pi^2 \beta^4 \int_{s=0}^{\infty} \exp(-\frac{\pi}{4} \beta^2 s^2) s \int_{u=s-1}^{s+1} u \\ & \int_{t=0}^{\infty} t^*(s, t, u) \theta(t^2 + s^2 - D^2) \exp(-\frac{\pi}{4} \beta^2 t^2) ds du dt \end{aligned} \quad (\text{A.46})$$

A.2.3 Analysis of ι_L^{Up}

Following the same procedure as in Section A.1.4 we can write, for low β :

$$\begin{aligned}
\iota_L^{Up} &= \frac{\exp(\chi_p)}{4} \pi^2 \beta^4 \int_{s=0}^{\infty} \exp(-\frac{\pi}{4} \beta^2 s^2) s \int_{u=s-1}^{s+1} u \\
&\quad \int_{t=0}^{\frac{\sqrt{1-(s-u)^2}}{\pi}} \theta(s^2 + t^2 - D^2) (t - \frac{\sqrt{1-(s-u)^2}}{\pi}) dt du ds + O(\beta^3) \quad (\text{A.47}) \\
&= \frac{\exp(\chi_p)}{4} \pi^2 \beta^4 \int_{s=D}^{\infty} \exp(-\frac{\pi}{4} \beta^2 s^2) s \int_{u=s-1}^{s+1} u \\
&\quad \int_{t=0}^{\frac{\sqrt{1-(s-u)^2}}{\pi}} (t - \frac{\sqrt{1-(s-u)^2}}{\pi}) dt du ds \\
&+ \frac{\exp(\chi_p)}{4} \pi^2 \beta^4 \int_{s=0}^D \exp(-\frac{\pi}{4} \beta^2 s^2) s \int_{u=s-1}^{s+1} u \\
&\quad \int_{t=\sqrt{D^2-s^2}}^{\frac{\sqrt{1-(s-u)^2}}{\pi}} (t - \frac{\sqrt{1-(s-u)^2}}{\pi}) dt du ds + O(\beta^3) \quad (\text{A.48})
\end{aligned}$$

Because at low β , $\int_{s=0}^D \exp(-\frac{\pi}{4} \beta^2 s^2) \sim D$ (Independent of β), the second term in Eq. (A.48) is of lower order than the first. Hence:

$$\begin{aligned}
\iota_L^{Up} &= \frac{\exp(\chi_p)}{4} \pi^2 \beta^4 \int_{s=D}^{\infty} \exp(-\frac{\pi}{4} \beta^2 s^2) s \int_{u=s-1}^{s+1} \\
&\quad u \left[-\frac{1}{2} (t - \frac{1-(s-u)^2}{\pi^2}) \right] du ds + O(\beta^3) \quad (\text{A.49})
\end{aligned}$$

$$= \frac{\exp(\chi_p)}{4} \pi^2 \beta^4 \int_{s=D}^{\infty} \exp(-\frac{\pi}{4} \beta^2 s^2) \frac{2}{3} \frac{s^2}{\pi^2} ds + O(\beta^3) \quad (\text{A.50})$$

$$= - \left[\frac{1}{3\pi} \text{erfc}(\sqrt{\chi_p}) \exp(\chi_p) + \frac{2}{3} \frac{\sqrt{\chi_p}}{\pi^{3/2}} \right] \beta + O(\beta^3) \quad (\text{A.51})$$

A.2.4 Analysis of ι_C^{Up}

Following the same procedure as in Section A.1.5 we can write, for low β :

$$\begin{aligned}
\iota_C^{Up} &= \frac{\exp(\chi_p)}{4} \pi^2 \beta^4 \int_{s=0}^{\infty} \exp\left(-\frac{\pi}{4} \beta^2 s^2\right) s \int_{\alpha=0}^{\infty} \theta\left((1+\alpha^2)s^2 - D^2\right) \\
&\quad \exp\left(-\frac{\pi}{4} \beta^2 \alpha^2 s^2\right) s \frac{\sqrt{\alpha^2+1}}{2} s d\alpha ds + O(\beta^2) \tag{A.52}
\end{aligned}$$

$$\begin{aligned}
&= \frac{\exp(\chi_p)}{8} \pi^2 \beta^4 \int_{\alpha=0}^{\infty} \sqrt{\alpha^2+1} \\
&\quad \int_{s=\frac{D}{\sqrt{1+\alpha^2}}}^{\infty} \exp\left(-\frac{\pi}{4} \beta^2 (1+\alpha^2) s^2\right) s^3 ds d\alpha + O(\beta^2) \tag{A.53}
\end{aligned}$$

$$= \frac{\exp(\chi_p)}{8} \pi^2 \beta^4 \int_{\alpha=0}^{\infty} \frac{\exp(-\chi_p)(\chi_p+1)}{2 \left[\frac{\pi}{4} \beta^2 (1+\alpha^2)\right]^2} \sqrt{1+\alpha^2} d\alpha \tag{A.54}$$

$$= 1 + \chi_p + O(\beta^2) \tag{A.55}$$

A.2.5 Conclusion

Therefore, the total Upper bound current to the probe is:

$$I_i^{Up}/I_i^0 = (1 + \chi_p) - \left[\frac{1}{3\pi} \operatorname{erfc}(\sqrt{\chi_p}) \exp(\chi_p) + \frac{2}{3} \frac{\sqrt{\chi_p}}{\pi^{3/2}} \right] \beta + O(\beta^2) \tag{A.56}$$

A.3 Charged sphere in a stationary plasma: Lower bound

The lower bound current is given by Eqs (A.37,A.38,A.39) after replacing $\theta(s^2 + t^2 - D^2)$ by $\theta(s - D)$.

We adopt here the same notation as in Section A.2, and split ι^{Low} in the same three terms.

A.3.1 Current drawn from the orbits in the magnetic shadow:

$$\iota_{in}^{Low}$$

ι_{in}^{Low} is quadratic in β because Eq. (A.43) is still valid.

A.3.2 Analysis of ι_L^{Low}

$$\begin{aligned} \iota_L^{Low} &= \frac{\exp(\chi_p)}{4} \pi^2 \beta^4 \int_{s=0}^{\infty} \exp(-\frac{\pi}{4} \beta^2 s^2) s \int_{u=s-1}^{s+1} u \\ &\quad \int_{t=D}^{\frac{\sqrt{1-(s-u)^2}}{\pi}} (t - \frac{\sqrt{1-(s-u)^2}}{\pi}) dt du ds + O(\beta^3) \end{aligned} \quad (\text{A.57})$$

We can now notice that a sufficient condition to have $\int_{t=D}^{\frac{\sqrt{1-(s-u)^2}}{\pi}} (t - \frac{\sqrt{1-(s-u)^2}}{\pi}) dt = 0$ is $D > \frac{1}{\pi}$, or using Eq. (A.41): $\beta < 2\pi\sqrt{\chi_p}$.

Therefore $\iota_L^{Low} = O(\beta^3)$.

A.3.3 Analysis of ι_C^{Low}

$$\begin{aligned} \iota_C^{Low} &= \frac{\exp(\chi_p)}{4} \pi^2 \beta^4 \int_{s=0}^{\infty} \exp(-\frac{\pi}{4} \beta^2 s^2) s \int_{\alpha=0}^{\infty} \theta(\alpha s - D) \\ &\quad \exp(-\frac{\pi}{4} \beta^2 \alpha^2 s^2) s \frac{\sqrt{\alpha^2 + 1}}{2} s d\alpha ds + O(\beta^2) \end{aligned} \quad (\text{A.58})$$

$$\begin{aligned} &= \frac{\exp(\chi_p)}{8} \pi^2 \beta^4 \int_{\alpha=0}^{\infty} \sqrt{\alpha^2 + 1} \int_{s=D/\alpha}^{\infty} \\ &\quad \exp(-\frac{\pi}{4} \beta^2 (1 + \alpha^2) s^2) s^3 ds d\alpha + O(\beta^2) \end{aligned} \quad (\text{A.59})$$

$$= \int_{\alpha=0}^{\infty} \frac{\alpha^2(1 + \chi_p) + \chi_p}{(1 + \alpha^2)^{3/2} \alpha^2 \exp(\chi_p/\alpha^2)} d\alpha + O(\beta^2) \quad (\text{A.60})$$

$$= 1 - \frac{\sqrt{\pi}}{2} \sqrt{\chi_p} \text{erfc}(\sqrt{\chi_p}) \exp(\chi_p) + O(\beta^2) \quad (\text{A.61})$$

A.3.4 Conclusion

Therefore, the total Lower bound current to the probe has no linear term, and is equal to:

$$I_i^{Low} / I_i^0 = 1 - \frac{\sqrt{\pi}}{2} \sqrt{\chi_p} \text{erfc}(\sqrt{\chi_p}) \exp(\chi_p) + O(\beta^2) \quad (\text{A.62})$$

Appendix B

Derivation of the OML currents to a sphere and infinite cylinder

B.1 Sphere

The ion current to an attractive spherical probe under the OML conditions can be calculated by integrating the distribution function at infinity, weighted by the factor $|\mathbf{v}|\pi r_p^2(1 - \frac{ZeV_p}{E_0})$ corresponding to the flux collected by particles whose velocity at infinity is \mathbf{v} (See Eq. (I.32)).

The integration geometry is shown on Fig. (B-1), and the integral expression for the current given by Eq. (I.33).

$$I_i = Z \int_{\theta=0}^{2\pi} \int_{v_z=-\infty}^{\infty} \int_{v_\rho=0}^{\infty} f_i^\infty(v_z, \theta, v_\rho) |\mathbf{v}| \pi r_p^2 \left(1 - \frac{ZeV_p}{E_0}\right) d\theta dv_z v_\rho dv_\rho \quad (\text{B.1})$$

with

$$f_i^\infty = \frac{n_\infty/Z}{(v_{ti}\sqrt{\pi})^3} \exp\left(-\frac{v_z^2 + v_\rho^2 + v_d^2 - 2v_z v_d}{v_{ti}^2}\right) \quad (\text{B.2})$$

and

$$E_0 = \frac{m_i}{2}(v_z^2 + v_\rho^2) \quad (\text{B.3})$$

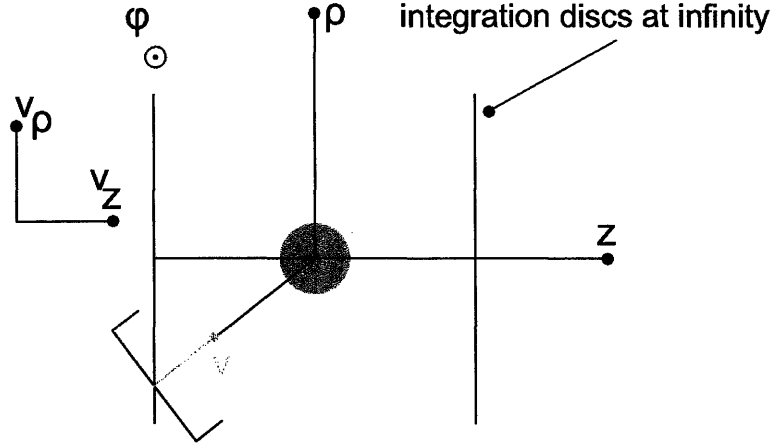


Figure B-1: Geometry for the OML current calculation to a spherical probe. The integration is performed over two disks perpendicular to the drift axis, and placed at infinity.

$$I_i = \frac{2\pi^2 r_p^2 n_\infty}{(v_{ti} \sqrt{\pi})^3} \int_{E_0=0}^{\infty} \left[\int_{v_z=-\sqrt{\frac{2E_0}{m_i}}}^{\sqrt{\frac{2E_0}{m_i}}} \exp\left(-\frac{2v_z v_d}{v_{ti}^2}\right) dv_z \right] \sqrt{\frac{2E_0}{m_i}} \exp\left(-\frac{2E_0}{m_i v_{ti}^2}\right) \left[1 - \frac{ZeV_p}{E_0} \right] \frac{dE_0}{m_i} \quad (\text{B.4})$$

$$= \frac{2\pi^2 r_p^2 n_\infty}{(v_{ti} \sqrt{\pi})^3} \int_{E_0=0}^{\infty} \sqrt{\frac{2E_0}{m_i}} \frac{v_{ti}^2}{2v_d} \left[\exp\left(\frac{2v_d}{v_{ti}^2} \sqrt{\frac{2E_0}{m_i}}\right) - \exp\left(-\frac{2v_d}{v_{ti}^2} \sqrt{\frac{2E_0}{m_i}}\right) \right] \exp\left(-\frac{2E_0}{m_i v_{ti}^2}\right) \left(1 - \frac{ZeV_p}{E_0}\right) \frac{dE_0}{m_i} \quad (\text{B.5})$$

$$= \frac{\sqrt{2}\pi^2 r_p^2 \exp\left(-\frac{v_d^2}{v_{ti}^2}\right) v_{ti}^2 n_\infty}{(v_{ti} \sqrt{\pi})^3 m_i^{3/2} v_d} [A - B - C + D] \quad (\text{B.6})$$

where A, B, C, D are defined as follows:

$$A = \int_{E_0=0}^{\infty} \sqrt{E_0} \exp\left(\frac{2v_d}{v_{ti}^2} \sqrt{\frac{2E_0}{m_i}} - \frac{2E_0}{m_i v_{ti}^2}\right) dE_0 \quad (\text{B.7})$$

$$= \frac{1}{4\left(\frac{2}{m_i v_{ti}^2}\right)^{5/2}} \left\{ \frac{8v_d}{m_i v_{ti}^3} + \exp\left(\frac{v_d^2}{v_{ti}^2}\right) \sqrt{\pi} \left[\frac{8v_d^2}{m_i v_{ti}^4} + \frac{4}{m_i v_{ti}^2} \right] \right. \\ \left. \left(1 + \operatorname{erf}\left(\frac{v_d}{v_{ti}}\right)\right) \right\} \quad (\text{B.8})$$

$$B = \int_{E_0=0}^{\infty} \sqrt{E_0} \exp\left(-\frac{2v_d}{v_{ti}^2} \sqrt{\frac{2E_0}{m_i}} - \frac{2E_0}{m_i v_{ti}^2}\right) dE_0 \quad (\text{B.9})$$

$$= \frac{1}{4\left(\frac{2}{m_i v_{ti}^2}\right)^{5/2}} \left\{ -\frac{8v_d}{m_i v_{ti}^3} + \exp\left(\frac{v_d^2}{v_{ti}^2}\right) \sqrt{\pi} \left[\frac{8v_d^2}{m_i v_{ti}^4} + \frac{4}{m_i v_{ti}^2} \right] \right. \\ \left. \left(1 - \operatorname{erf}\left(\frac{v_d}{v_{ti}}\right)\right) \right\} \quad (\text{B.10})$$

$$C = ZeV_p \int_{E_0=0}^{\infty} \frac{1}{\sqrt{E_0}} \exp\left(\frac{2v_d}{v_{ti}^2} \sqrt{\frac{2E_0}{m_i}} - \frac{2E_0}{m_i v_{ti}^2}\right) dE_0 \quad (\text{B.11})$$

$$= ZeV_p \exp\left(\frac{v_d^2}{v_{ti}^2}\right) \frac{\sqrt{\pi}}{\sqrt{2/m_i}} v_{ti} \left[1 + \operatorname{erf}\left(\frac{v_d}{v_{ti}}\right) \right] \quad (\text{B.12})$$

$$D = ZeV_p \int_{E_0=0}^{\infty} \frac{1}{\sqrt{E_0}} \exp\left(-\frac{2v_d}{v_{ti}^2} \sqrt{\frac{2E_0}{m_i}} - \frac{2E_0}{m_i v_{ti}^2}\right) dE_0 \quad (\text{B.13})$$

$$= ZeV_p \exp\left(\frac{v_d^2}{v_{ti}^2}\right) \frac{\sqrt{\pi}}{\sqrt{2/m_i}} v_{ti} \left[1 - \operatorname{erf}\left(\frac{v_d}{v_{ti}}\right) \right] \quad (\text{B.14})$$

After simplification we recover Eq. (I.34)

$$I_i/I_i^0 = \frac{1}{2} \exp\left(-\frac{v_d^2}{v_{ti}^2}\right) + \frac{\sqrt{\pi}}{2} \left[\frac{v_d}{v_{ti}} + \frac{v_{ti}}{2v_d} + \chi_p \frac{v_{ti}}{v_d} \right] \operatorname{erf}\left(\frac{v_d}{v_{ti}}\right) \quad (\text{B.15})$$

where $I_i^0 = n_{\infty} \frac{v_{ti}}{2\sqrt{\pi}} 4\pi r_p^2$ is the thermal current collected by the sphere.

B.2 Infinite cylinder

Similar calculations can be performed for an infinite cylindrical probe (The cylinder length L is large compared to its radius r_p), provided v_d is considered as the drift velocity component perpendicular to the probe axis. The geometry is shown in Fig. (B-2); the weighting factor is $2r_p L v_{\perp} \sqrt{1 - \frac{ZeV_p}{E_0}}$, where E_0 is the ion kinetic energy in the \perp direction at infinity.

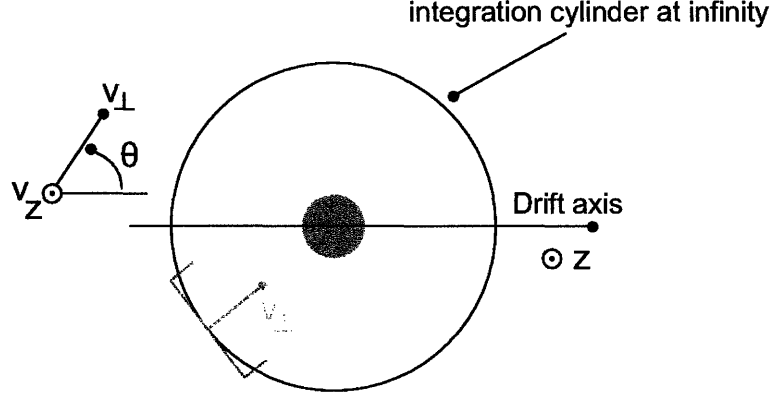


Figure B-2: Geometry for the OML current calculation to an infinite cylindrical probe. The integration is performed over a cylinder coaxial with the probe, and placed at infinity.

$$I_i = ZL \int_{\theta=0}^{2\pi} \int_{v_z=-\infty}^{\infty} \int_{v_{\perp}=0}^{\infty} f_i^{\infty}(v_z, \theta, v_{\perp}) 2r_p v_{\perp} \sqrt{1 - \frac{2ZeV_p}{m_i v_{\perp}^2}} d\theta dv_z v_{\perp} dv_{\perp} \quad (\text{B.16})$$

with:

$$f_i^{\infty} = \frac{n_{\infty}/Z}{(v_{ti}\sqrt{\pi})^3} \exp\left(-\frac{v_z^2 + v_{\perp}^2 + v_d^2 - 2v_{\perp}v_d \cos\theta}{v_{ti}^2}\right) \quad (\text{B.17})$$

The integration over v_z is straightforward and we are left with:

$$I_i = 2r_p L n_{\infty} \exp\left(-\frac{v_d^2}{v_{ti}^2}\right) \frac{1}{(v_{ti}\sqrt{\pi})^2} \int_{v_{\perp}=0}^{\infty} \exp\left(-\frac{v_{\perp}^2}{v_{ti}^2}\right) v_{\perp}^2 \sqrt{1 - \frac{2ZeV_p}{m_i v_{\perp}^2}} \int_{\theta=0}^{2\pi} \exp\left(\frac{2v_{\perp}v_d \cos\theta}{v_{ti}^2}\right) d\theta dv_{\perp} \quad (\text{B.18})$$

By using the following property of second kind Bessel functions:

$$I_n(x) = \frac{1}{\pi} \int_0^{\pi} \exp(x \cos\theta) \cos(n\theta) d\theta \quad (\text{B.19})$$

we can integrate over θ and express the current as:

$$I_i/I_i^0 = \frac{4}{\sqrt{\pi}} \exp\left(-\frac{v_d^2}{v_{ti}^2}\right) \int_{\xi=0}^{\infty} \exp(-\xi^2) \sqrt{\xi^2 + \chi_p} I_0\left(2\xi \frac{v_d}{v_{ti}}\right) \xi d\xi \quad (\text{B.20})$$

where $\xi = \frac{v_\perp}{v_{ti}}$ and I_i^0 is the random thermal current collected by the cylinder (different from the I_i^0 corresponding to the sphere):

$$I_i^0 = n_\infty \frac{v_{ti}}{2\sqrt{\pi}} 2\pi r_p L \quad (\text{B.21})$$

The integral of Eq. (B.20) can not be cast in closed form, unless $v_d = 0$. In this case we are left with:

$$I_i/I_i^0 = \frac{4}{\sqrt{\pi}} \int_{\xi=0}^{\infty} \exp(-\xi^2) \sqrt{\xi^2 + \chi_p} \xi d\xi \quad (\text{B.22})$$

$$= \frac{2}{\sqrt{\pi}} \sqrt{\chi_p} + \exp(\chi_p) \text{erfc}(\sqrt{\chi_p}) \quad (\text{B.23})$$

If $\chi_p \gtrsim 2$ we are left with the well known form [1]:

$$I_i = I_i^0 \frac{2}{\sqrt{\pi}} \sqrt{1 + \chi_p} \quad (\text{B.24})$$

B.3 Comparison of the OML current for the sphere and the cylinder

Fig. (B-3) compares the evolution of the OML current with the normalized probe potential $\chi_p = -\frac{ZeV_p}{T}$ to an infinite sphere and a cylinder.

There is a noticeable difference between the two geometries. While for the cylinder the current is a monotonic rising function of the drift velocity, this is not the case for the sphere if the normalized potential is greater than 1.

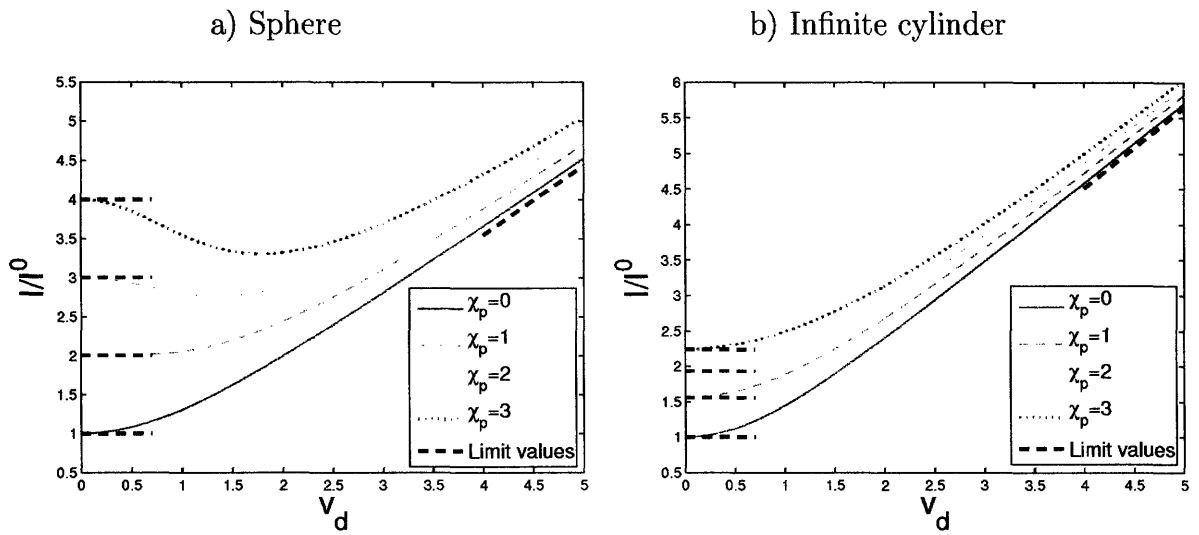


Figure B-3: Attracted current to a sphere and an infinite cylinder as function of the drift velocity and the normalized probe potential in the OML conditions.

Bibliography

- [1] H.M. Mott-Smith and I. Langmuir *The theory of collectors in gaseous discharges* Physical review **28**, 727 (1926).
- [2] I.H. Hutchinson *Ion collection by a sphere in a flowing plasma: 1. Quasineutral* Plasma Phys. Control. Fusion **44**, 1953-1977 (2002).
- [3] I.H. Hutchinson *Ion collection by a sphere in a flowing plasma: 2. Non-zero Debye length* Plasma Phys. Control. Fusion **45**, 1477-1500 (2003).
- [4] I.H. Hutchinson *Principles of Plasma Diagnostics, Second edition* Cambridge University press (2002).
- [5] G.L. Delzanno, A. Bruno, G. Sorasio and al. *Exact orbital motion theory of the shielding potential around a spherical body* Physics of Plasmas **16**, 062102 (2005).
- [6] I.H. Hutchinson *A fluid theory of ion collection by probes in strong magnetic fields with plasma flow* Physics of Fluids **30**, 3777-3781 (1987).
- [7] K.S. Chung and I.H. Hutchinson *Kinetic theory of ion collection by probing objects in flowing strongly magnetized plasmas* Physical review A **38**, 4721-4731 (1988).
- [8] T. Shikama, S. Kado, A. Okamoto and Al *Practical formula for Mach number probe diagnostics in weakly magnetized plasmas* Physics of plasmas **12**, 044504 (2005).
- [9] E.C. Whipple *PhD Thesis* George Washington University (1965).

- [10] L.W. Parker and B.L. Murphy *Potential buildup on an electron-emitting ionospheric satellite* J. Geophys. Res. **72**, 1631-1636 (1967).
- [11] J. Rubinstein. and J.G. Laframboise *Theory of a spherical probe in a collisionless magnetoplasma* Physics of Fluids **25**, 1174-1182 (1982).
- [12] L.J. Sonmor and J.G. Laframboise *Exact current to a spherical electrode in a collisionless, large Debye-length magnetoplasma* Physics of Fluids **3**, 2472-2490 (1991).
- [13] E.C. Whipple *Potential of surfaces in space* Reports on Progress in Physics **44**, 1197-1250 (1981).
- [14] N. Singh, B.I. Vashi and L.C. Leung *Three-dimensional numerical simulation of current collection by a probe in a magnetized plasma* Geophysical Research Letters **2**, 833-836 (1994).
- [15] I.B. Bernstein and I.N. Rabinovitz *Theory of Electrostatic Probes in a Low-Density Plasma* Physics of fluids **2**, 112-121 (1959).
- [16] K.U. Riemann *The Bohm criterion and sheath formation* J. Phys. D: Appl. Phys **24**, 493-518 (1991).
- [17] C. Birdsall and A. Langdon *Plasma Physics via computer simulation* McGraw-Hill, (1985).
- [18] J. Rubinstein and J.G. Laframboise *Theory of a cylindrical probe in a collisionless magnetoplasma* Physics of Fluids **19**, 1900-1908 (1976).
- [19] J.P. Boris *Proceedings of the Fourth Conference on Numerical Simulation of Plasmas* edited by J.P. Boris and R.A. Shanny (Naval Research Laboratory, Washington DC), (1970).
- [20] P.H. Stolz and al. *Efficiency of a Boris-like integration scheme with spatial stepping* Physical Review Special Topics - Accelerators and beams **5**, (2002).

- [21] L. Verlet *Computer 'experiments' on classical fluids. I. Thermodynamical properties of Lennard-Jones molecules* Phys. Rev. **159**, 88-103 (1967).
- [22] G. Lapenta *Simulation of charging and shielding of dust particles in drifting plasmas* Physics of Plasmas **6** 1442-1447 (1999).
- [23] M.H. Lee, M.J. Duncan and H.F. Levison *Variable Timestep Integrators for Long-Term Orbital Integrations* (1997).
- [24] D. Donnelly and E. Rogers *Symplectic integrators: An introduction* Am. J. Phys., **73**, 938-945 (2005).
- [25] H. Goldstein, C. Poole and J. Safko *Classical Mechanics, third edition* Pearson Education (2002).
- [26] I.H. Hutchinson *Ion collection by a sphere in a flowing plasma: 3. Floating potential and drag force* Plasma Phys. Control. Fusion **47**, 71-87 (2005).
- [27] I.H. Hutchinson and L. Patacchini *Computation of the effect of neutral collisions on ion current to a floating sphere in a stationary plasma* Physics of Plasmas **14**, 013505 (2007).